Syntheses of Biocompatible Luminescent Nanocrystals for Visible and Short-wave Infrared Imaging Applications

by

Yue Chen

B.S. Chemistry, 2012
University of Science and Technology of China

Submitted to the Department of Chemistry
in Partial Fulfillment of the Requirements for the Degree of

DOCTOR OF PHILOSOPHY
IN PHYSICAL CHEMISTRY

at the

MASSACHUSETTS INSTITUTE OF TECHNOLOGY

February 2018

© 2018 Massachusetts Institute of Technology.

All rights reserved.
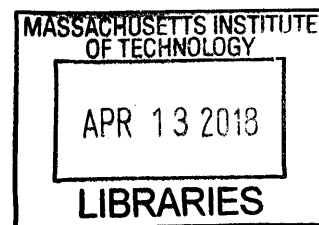
Signature of Author: **Signature redacted**

Department of Chemistry
December 11, 2017

Certified by: **Signature redacted**

Moungi G. Bawendi
Lester Wolfe Professor of Chemistry
Thesis Supervisor

Accepted by: **Signature redacted**

Robert W. Field
Chairman, Departmental Committee on Graduate Students

This doctoral thesis has been examined by a committee of the

Department of Chemistry as follows:

Signature redacted

Professor Troy Van Voohis ....

Thesis Committee Chair

Haslam and Dewey Professor of Chemistry

Signature redacted

Professor Moungi G. Bawendi ....

Thesis Supervisor

Lester Wolfe Professor of Chemistry

Signature redacted

Professor Timothy M. Swager ...

Thesis Committee Member

John D. MacArthur Professor of Chemistry

Syntheses of Biocompatible Luminescent Nanocrystals for Visible and Short-wave Infrared Imaging Applications

by

Yue Chen

Submitted to the Department of Chemistry
on January 15, 2018 in Partial Fulfillment of the
Requirements for the Degree of Doctor of Philosophy in Chemistry

Abstract

The primary focus of this thesis is to synthesize biocompatible luminescent nanocrystals for visible and short-wave infrared (1-2 µm, SWIR) imaging applications. Quantum dots (QDs) have been promising fluorescent probes for biomedical imaging due to their high quantum yield (QY), narrow photoluminescence spectra, and excellent photostability. However, challenges remain to be solved to transfer the as-synthesized hydrophobic QD to aqueous solutions while maintaining the high QY and a compact size. This study involves the design and synthesis of a novel ligand that can be introduced to the established QD synthesis, producing norbornene functionalized QDs that can be readily phase transferred into water *via* norbornene/tetrazine click chemistry, meanwhile allowing flexible functionalization of the QDs by incorporating a functional group on the hydrophilic chain. This ligand system can be applied to a variety of carboxylic-ligand-stabilized QDs, with emission spectra spanning the visible and the SWIR region. The resulting water-soluble QDs exhibit a high QY, a small hydrodynamic diameter (HD), and excellent colloidal stability and pH stability. Further *in vitro* cell labeling experiments using azido-functionalized QDs demonstrates their potential for cell targeting applications.

As *in vivo* imaging in the SWIR range has further reduced background noise from tissue scattering compared to traditional visible and near infrared (0.7-1 µm, NIR) imaging, images of higher contrast and better resolution can be readily obtained. The next challenge is to develop SWIR emitters that have high quantum efficiency and minimal toxicity, which is of critical importance in order to promote this technology for clinical applications. Our study found that the emission of luminescent gold nanoclusters can be tuned from the visible to the SWIR region by proper selection of ligands and post ligand modifications. The SWIR-emitting gold nanoclusters have a good QY, a HD that is small enough that they exhibit a rapid renal clearance, and images taken in the SWIR region show better resolution of the blood vessels than in the NIR region.

Thesis Supervisor: Moungi G. Bawendi

Title: Lester Wolfe Professor of Chemistry

Preface

Chapters of this thesis were reproduced in part from the following references:

Chen, Y.; Montana, D. M.; Wei, H.; Cordero, J. M.; Schneider, M.; Le Guével, X.; Chen, O.; Bruns, O. T.;* Bawendi, M. G.* Shortwave Infrared in Vivo Imaging with Gold Nanoclusters. *Nano Lett.* **2017**, *17*, 6330-6334.

Chen, Y.; Cordero, J. M.; Wang, H.; Franke, D.; Achorn, O. B.; Freyria, F. S.; Coropceanu, I.; Wei, H.; Chen, O.; Mooney, D. J.; Bawendi, M. G. A Ligand System for Flexible Functionalization of Quantum Dots via Click Chemistry. **2017**, *submitted*.

Table of Contents

Chapter 3: Live Cell Labeling with QD Probes   65

Chapter 4: *In Vivo* Fluorescence Imaging in the Short-wave Infrared   89

Chapter 5: SWIR-emitting Gold Nanoclusters   102

Chapter 6: SWIR *In Vivo* Imaging with Gold Nanoclusters   **120**

Acknowledgement   **129**

List of Figures and Schemes

List of Tables

Chapter 1

Introduction of Quantum Dots as Fluorescent Probes for Biomedical Imaging Applications

1.1 Introduction of Quantum Dots

Figure 1-1. Schematic illustration of the quantum confinement effect. Semiconductor band gap increases with decreasing size of the nanocrystal.

Quantum Dots (QDs) are spherical nanoscale semiconductors, the size of which are usually smaller than 10 nm. Because of the quantum confinement effect, the continuous density of states in the bulk reduces to discrete atom-like states, resulting in a different energy gap of the QD from that of the bulk material (Figure 1-1).[1-2] When the radius of a QD is smaller than the exciton Bohr radius (the average distance between the electron in the conduction band and the hole it leaves in the valence band), the energy gap is strongly dependent on the nanocrystal size.

For QDs of the same composition, the smaller the size is, the larger the energy gap will be. This can be explained using the particle in the box model, where the electron and the hole can be seen as hydrogen in the Bohr model. In this case, the energy levels of the exciton can be represented as the ground level of the particle in a box, which is proportional to $1/L^2$ (L is the length of the box).[1-2] Therefore, by tuning the size of QDs, the absorption and emission properties can be finely tuned.

1.2   Syntheses of QDs

1.2.1   Syntheses of Visible-emitting Core/Shell QDs

Syntheses of high-quality QDs with high monodispersity in size and shape had been challenging for a period of time until a breakthrough in the early 1990s was achieved. This method enables syntheses of CdE (E=S, Se, Te) semiconductor nanocrystals with high uniformity by injecting organometallic reagents into a hot coordinating solvent.[7] For example, Figure 1-2a shows the absorption spectra of a size series of monodispersed cadmium selenide (CdSe) QDs prepared using the hot injection method. The first extinction peak shifts from 400 nm to 700 nm with the diameter increasing from 1.7 nm to 15 nm. Since then, more synthetic procedures based on the hot injection method have been developed, such as replacing the acutely toxic and unstable dimethylcadmium precursor with cadmium oxide dissolved by octadecylphosphonic acid, or introducing the use of non-coordinating solvents.[8-9]

Despite the significant improvement of II-VI QD syntheses, the quantum yield (QY) of these QDs are very low due to the existence of surface trap states. For example, the as-synthesized CdSe QDs usually have a QY of less than 10%. Over the past few decades, significant progress has been made by researchers to synthesize QDs with a uniform size, suppressed blinking, and an increased QY.[10-12] Overcoating QDs with a shell structure has been demonstrated as a powerful solution to

increase the photoluminescence QY of QDs.[10, 13-14] First, the growth of a shell can passivate the surface trap states of the core material, where the electrons and holes recombine through non-radiative pathways. In addition, the shell material can provide isolation for the electrons or holes from the moisture and oxygen in the surrounding environment by confining both the electron and hole to the core material (Type I) (Figure 1-2b), or one of the electron or hole to the core material while allowing the other to delocalize into the shell (Type II).
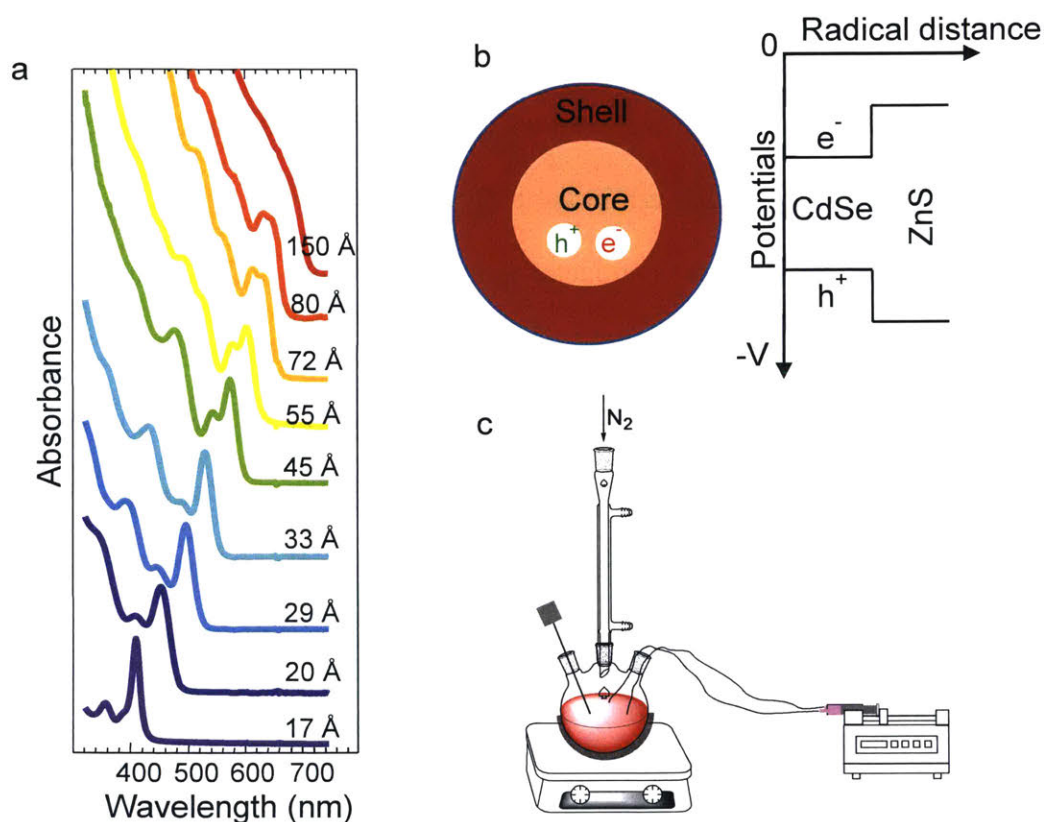
Figure 1-2. (a) Absorption spectra of a CdSe size series. Figure reproduced from C. B. Murray, Ph.D. Thesis, MIT, 1995. (b) Band structure of Type I QDs, in which both the electron and the hole are confined to the core. (c) Synthetic setup for CdSe/CdS core/shell QDs. A syringe pump is employed for continuous infusion of precursors.

In our recently described result, successful synthesis of compact high-quality quasi-Type II CdSe/CdS core/shell nanocrystals with narrow emission linewidths and suppressed blinking has been reported.[4] The CdSe/CdS QDs were synthesized *via* an optimized process that maintains a slow growth rate of the shell by using octanethiol and cadmium (II) oleate as precursors. As shown in Figure 1-2c, the precursors were continuously injected into the reaction solution using a syringe pump over two hours. The slow continuous precursor infusion and the relatively low reactivity of octanethiol lead to a well-maintained size distribution during the shell growth. Since the lattice mismatch between the CdSe core and the CdS shell is very small (3.9%), the final CdSe/CdS core/shell QDs maintain the original crystal structure of CdSe core. The resulting CdSe/CdS QDs have close to unity QYs, narrow and symmetric PL spectra with full-width at half-maximum (FWHM) as narrow as 20 nm, and significantly suppressed blinking (Figure 1-3).

Because of the quasi-Type II band structure of CdSe/CdS core/shell QDs, the electron can be delocalized in the conduction bands of both the core and the shell materials.[15] Thus, as the shell grows, the emission spectrum of the core/shell QDs red shifts. Therefore, it is challenging to synthesize CdSe/CdS core/shell QDs that exhibit green emission. In order to synthesize high-quality QDs with emission spectrum spanning the visible region, we adapted this continuous slow precursor infusion and slow shell growth procedure to synthesize QDs of other II-VI materials, such as CdSe/ZnS, and successfully prepared green- and yellow- emitting CdSe/ZnS QDs with > 90% QY and < 25 nm FWHM. We chose CdS/ZnS core/shell system to produce blue-emitting QDs. As shown in Figure 1-3d, QDs of different compositions are synthesized, and the emission spectra of these QDs are tunable within the visible region (400-700 nm). Moreover, the FWHM of the emission spectra are very narrow, allowing more colors of QDs to be fitted in the visible region with minimal spectral overlap, which can be very useful for multiplexing imaging applications.
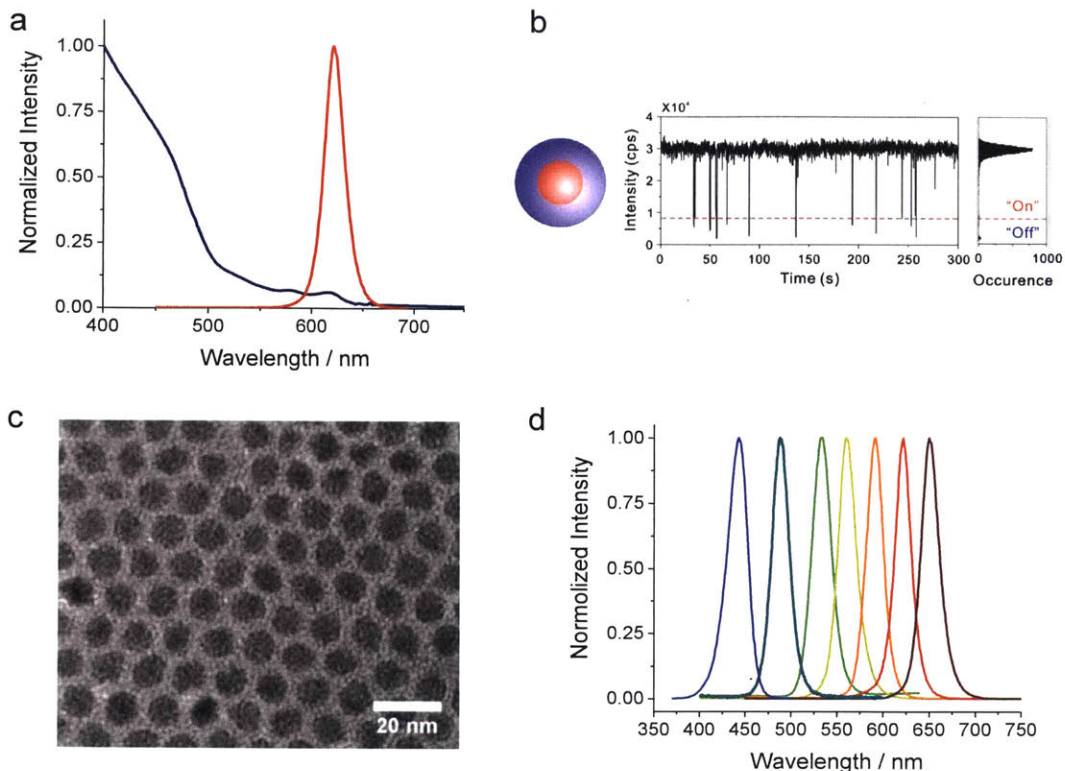
Figure 1-3. (a) Absorption (blue) and photoluminescence (red) spectra of CdSe/CdS core/shell QDs. (b) Representative photoluminescence blinking trace of a single CdSe/CdS core/shell QD. Histogram indicates the distribution of intensities observed in the trace (Figure is adapted from ref.[4]). (c) Representative transmission electron microscopy image of CdSe/CdS QDs. (d) Photoluminescence spectra of a color series of QDs (blue: CdS/ZnS; cyan: CdZnSeS; green, yellow, and orange: CdSe/ZnS; red and wine: CdSe/CdS).

1.2.2 Syntheses of Short-wave Infrared-emitting QDs

Successful synthesis of high-quality indium arsenide (InAs) -based QDs that emit in the short-wave infrared (SWIR) region has also been reported recently.[5, 16] III-V QDs have historically struggled to match the high-quality optical properties of II-VI QDs.[17-19] By investigating the kinetics that govern InAs nanocrystal growth, Franke *et al.* managed to synthesize large InAs QDs with narrow emission linewidths.[5] Further passivation of the InAs QDs with CdSe, CdS or ZnS

24

double shells improves the QY by more than six-fold, and the photostability is significantly enhanced. The emission spectra of these InAs/CdSe/CdS or InAs/CdSe/ZnS core/shell/shell QDs span the entire sensitivity range of modern InGaAs SWIR cameras with QYs ranging from 16 to 82% (Figure 1-4), which are very helpful for new biomedical imaging applications in the SWIR range. The probes can also improve infrared nanocrystal-LEDs and photon-upconversion technology.
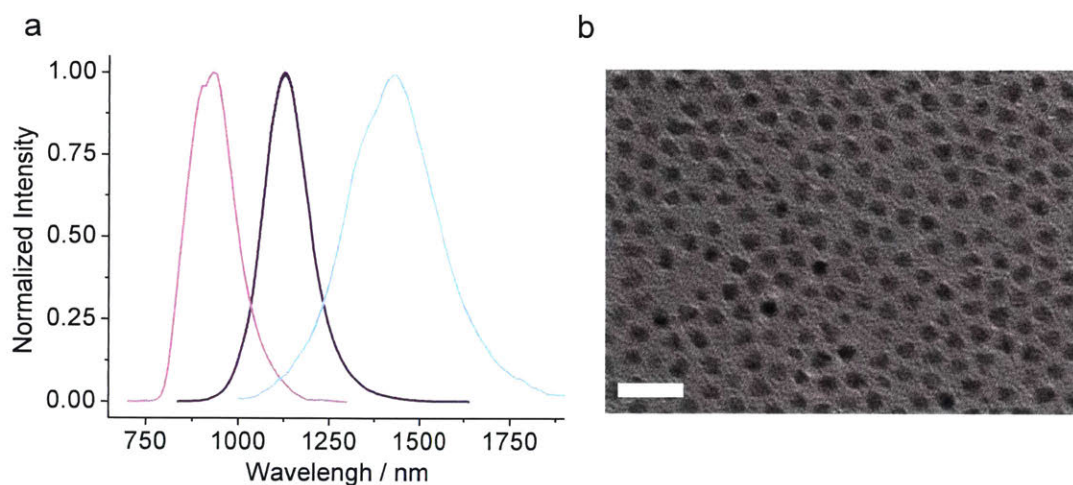
Figure 1-4. (a) InAs/CdSe/CdS and InAs/CdSe/ZnS core/shell/shell QDs spanning the entire sensitivity range of modern InGaAs cameras for wavelength-selective SWIR imaging. (b) Representative TEM image of InAs/CdSe/CdS core/shell/shell QDs with a size distribution of 8%. Scale bar, 20 nm (Figures are reproduced from ref.[5]).

As high-quality QDs emitting from the visible to the SWIR range are becoming more available with improved synthetic methods, these core/shell QDs have found numerous applications in biological imaging,[20-22] photovoltaic devices,[23-25] light emitting diodes,[26-28] photodetector devices,[29-30] and QDs displays.[31-32] QD displays, especially, have gained increasing popularity on the television market as television giants such as Samsung and TCL are pursuing wider color gamut and improved visual experience. In this work, we will focus on the biological applications of the improved visible- and SWIR- emitting QDs.

1.3 QDs for Biomedical Imaging Applications

1.3.1 QD Probes for Live Cell Tracking

QDs have long been explored as alternative fluorophores to organic dyes for *in vitro* imaging applications.[33-34] Due to their excellent photostability, QDs are the preferred fluorescent probes for long-term imaging applications that require constant, high flux density excitation, such as live cell tracking.[35-36] In fact, QDs have been demonstrated to have orders of magnitude higher photostability than organic dyes, or even higher in the case of SWIR-emitting QDs.[37] Wu et al. monitored the fluorescence intensity changes of QDs and the organic dye Alexa Fluor 488 simultaneously in the same cell under the same excitation condition for 3 min. QDs showed higher stability against photobleaching than Alexa 488 regardless of which part of the cell was stained with QDs (Figure 1-5).[6]
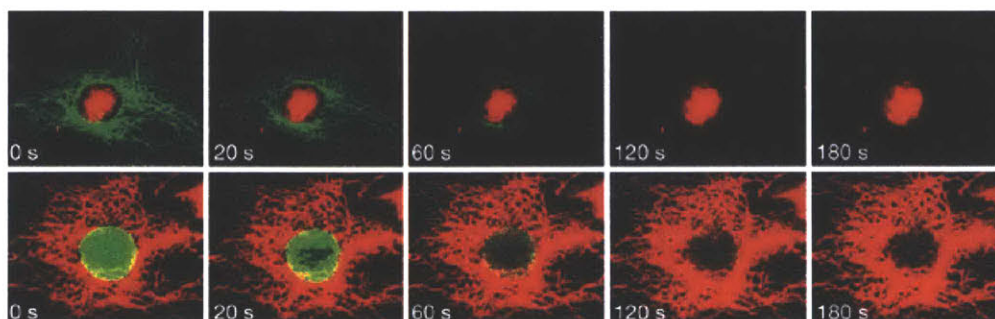
Figure 1-5. Nuclear antigens were labeled with QD 630-streptavidin (red, top row), and Alexa 488 conjugated to anti-human IgG(green, bottom row), respectively, while microtubules were labeled with Alexa 488 conjugated to anti-mouse IgG (green, top row), and QD 630-streptavidin (red, bottom row) simultaneously in a 3T3 cell. The cells were continuously illuminated for 3 min using a 100 W mercury lamp. Continuous exposure times in seconds are indicated. Scale bar, 10 μm (Figures are reprinted from ref.[6] with permission from Nature Publishing Group).

The better photostability of QDs makes them promising candidates for live cell imaging, where the time scale of observation for conventional organic dyes is limited due to photobleaching. For example, Derfus et al. demonstrated live cell labeling and organelle tracking using CdSe/ZnS core/shell QDs;[38] Jaiswal et al. reported long-term imaging of QD-labeled live cells for 14 h, and no decline in the emission intensity of QDs was observed;[33] and Cui et al. reported using QD-labeled nerve growth factor (NGF) to track the movement of NGF in real time in a compartmentalized culture of rat dorsal root ganglion neurons.[39] These results indicate the suitability of QDs as fluorescent probes for long-term, high flux density excitation imaging.

1.3.2 QD Probes for Multiplexing Imaging

A major obstacle of visualizing biological structures in all their complexity is spectral overlap between fluorophores. Traditional fluorescent imaging is limited by the number of available fluorophores that have minimal spectral overlap, and only three to four targets can be examined at the same time.[40] Fluorescence in situ hybridization, for example, is a recently described powerful strategy for highly multiplexed transcriptome imaging. However, multiple rounds of time consuming dehybridization, hybridization, imaging, and washing are required due to lack of available non-overlapping fluorophores. Researchers have reported several strategies to address this issue, including developing new optical setups that allow better resolution to detect overlapping fluorophores, such as spectrally resolved stochastic optical reconstruction microscopy (SR-STORM), and developing new probes that have narrow spectra and are easy to resolve from one another. For the latter option, QDs are ideal candidate probes to solve the "lack of probes" issue.[41-42] The broad absorption spectra of QDs allows for using a single excitation source for all fluorophores, and the narrow emission spectra enable discrimination of an increased number of different fluorophores that can be imaged at the same time. Quantum Dot Corp. demonstrated five-

color staining of fixed human epithelial cells using QDs (Figure 1-6) more than ten years ago.[43] With the improved QY, narrower FWHM of QDs, and the availability of improved SWIR-emitting QDs, multiplexing imaging with seven or more targets at the same time can be readily realized.

a

b
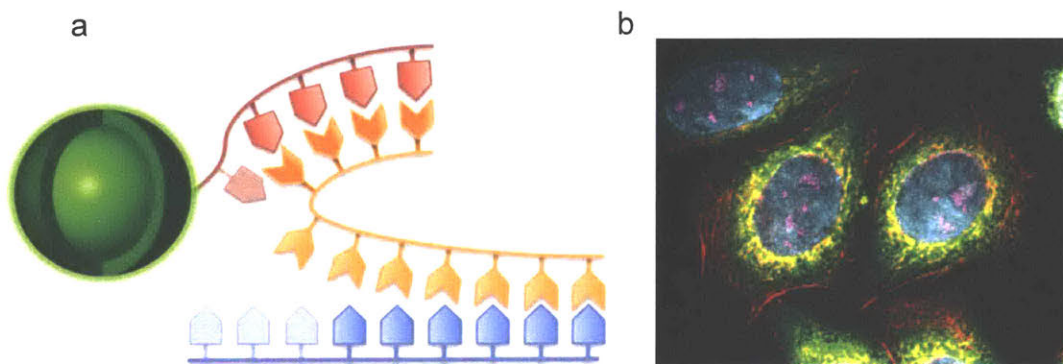
Figure 1-6. (a) Schematic illustration of using oligo conjugated QD probes for fluorescence in situ hybridization. (b) Multiplexing immunolabeling of fixed human epithelial cells with five colors of QD conjugates. Nuclear antigens (Cyan, Qdot 655 anti-human), Ki-67 protein (magenta, Qdots 605 anti-rabbit), mitochondria (orange, Qdot 525 anti-mouse), microtubules (green Qdot 565 anti-rat), and actin filaments (red, Qdot 705 streptavidin). Figure credit to Quantum Dot Corp, adapted from ref.[43].

1.3.3 QD Probes for SWIR *In Vivo* Imaging

Non-invasive *in vivo* fluorescence imaging in the SWIR range has been demonstrated to improve the tissue penetration depth and spatial resolution due to the significantly reduced tissue scattering and autofluorescence.[44-45] However, most organic dyes that emit in the SWIR range are highly hydrophobic and suffer from extremely low QY once being transferred into water, and therefore SWIR emitters with high quantum efficiencies need to be developed. With the improved generation of SWIR emitting QDs being available, especially InAs- based QDs that have high QY and photostability, QDs have gained increasing attention as promising fluorescent contrast agents for SWIR *in vivo* imaging applications. For example, Franke *et al*. demonstrated non-invasive

28

through-skull fluorescence imaging of the brain vasculature of murine models;[5] Bruns *et al.* also reported SWIR *in vivo* imaging of mice using InAs- based QDs, and detailed three-dimensional quantitative flow maps of the mouse brain vasculature were generated (Figure 1-7).[3] In Bruns' work, the glioblastoma multiforme tumor in a mouse brain was pre-labelled by injection of SWIR QD composite particles three days before imaging, and the particles were seen to accumulate in the collapsed and abnormal tumor blood vessels. A second dose of particles was injected and perfusion was imaged across the entire cranial window. A multicolor angiography image of a glioblastoma tumor through a cranial window was generated, and visualization of the overall structure of the vasculature in the tumor margin and healthy tissue was realized. These high-contrast and high-resolution images demonstrate the great potential of using SWIR emitting QDs for non-invasive *in vivo* biomedical imaging applications.
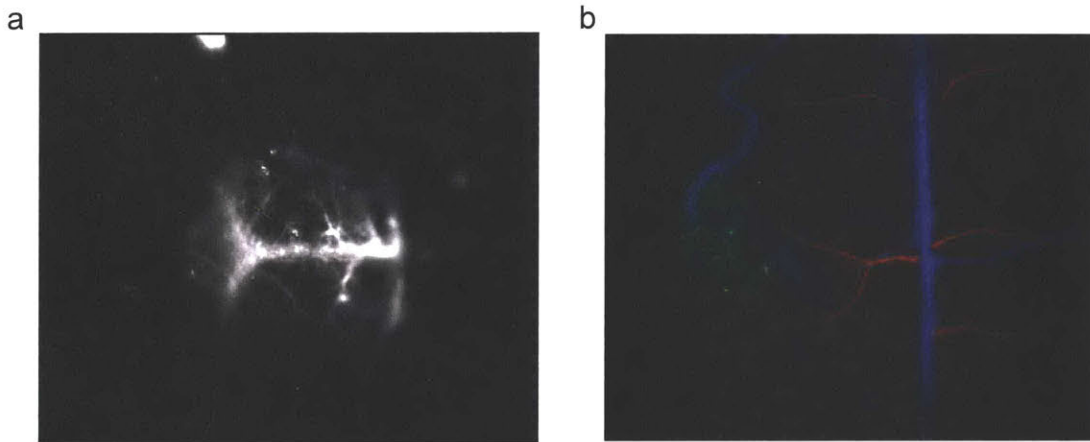
Figure 1-7. (a) Image of the brain vasculature in a mouse. A quantum dot mixture was injected into a living mouse's vascular system, and the image was taken using an InGaAs camera with a 1450 nm bandpass filter applied (image reproduced from M. Allen, Master thesis, MIT, 2016). (b) A multicolor angiography image of a glioblastoma tumor through a cranial window (figure reproduced from ref.[3]).

Overall, owing to their high quantum efficiency, broad absorption and narrow emission spectra, and excellent photostability, QDs are promising fluorescent probes for live cell imaging, multiplexing imaging, and SWIR *in vivo* imaging applications. However, a prerequisite for all the above applications is to transfer the as-synthesized hydrophobic QDs into aqueous solutions while maintaining the optical properties and compact sizes, and rendering physiological stability.

1.4 Phase Transfer of QDs
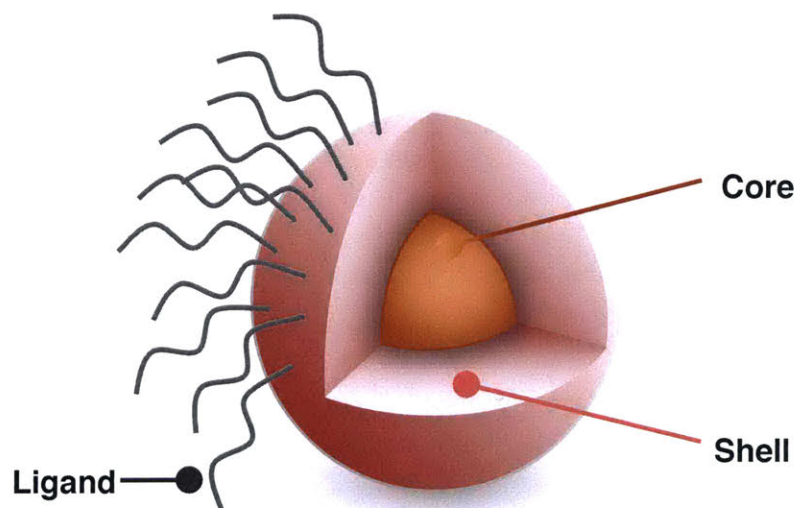
Figure 1-8. Structure of a core-shell nanocrystal.

High-quality QDs with uniform sizes and high QYs are usually prepared using organometallic precursors in hot coordinating solvents, and the as-synthesized QDs are passivated with long-chain hydrophobic ligands, such as carboxylate ligands, alkylamines, trioctylphosphine (TOP) and trioctylphosphineoxide (TOPO) (Figure 1-8). These hydrophobic ligands determine that the as-synthesized QDs are only dispersible in organic solvent (e.g., hexane, chloroform, or toluene). In order to use these QDs for biomedical imaging applications, surface ligand modifications are often performed to transfer the QDs from organic solvents to aqueous solutions. Several strategies reported by researchers so far can be classified into three categories: encapsulating QDs into

30

amphiphilic polymers, coating QDs with a silica shell, and replacing the native hydrophobic ligands with hydrophilic molecules.

1.4.1 Amphiphilic Polymer Encapsulation
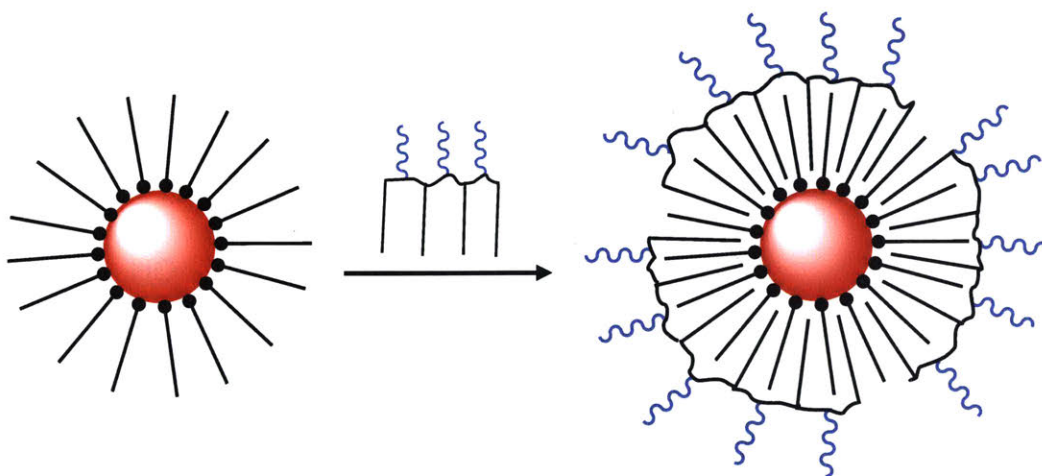
Figure 1-9. Schematic illustration of encapsulating QDs into amphiphilic polymers.

Amphiphilic polymer encapsulation method has been demonstrated to be a universal method to transfer hydrophobic ligand-capped nanocrystals of different compositions into aqueous solutions.[46-48] The hydrophobic chains of the amphiphilic polymer can interact with the native hydrophobic ligands on the nanocrystal surfaces through Van der Waals forces, and the hydrophilic chains of the polymer will extend away from the center to enable water solubility (Figure 1-9). Since the native ligands on the nanocrystal surfaces are left intact, this method maintains the QY very well. However, small aggregates are sometimes inevitable upon water solubilization of QDs, leading to a significant increase in the hydrodynamic diameter. For example, 4-8 nm QDs were shown to have hydrodynamic diameters of 20-40 nm after being coated with amphiphilic polymers.[46, 49] This large increase in hydrodynamic diameter is more than the expected size increase from the polymer, probably due to the dangling chain of the polymer on QD surfaces,

which will also result in non-specific binding to serum proteins or cell membranes. The large hydrodynamic diameter of QDs limits their use in biological applications, because these polymer coated QDs are much larger than the receptors being labeled, which will potentially interfere with the function of labeled proteins. In addition, the large size also prevents QDs from accessing specific tissues such as neuronal synapses.

1.4.2 Silica Coating
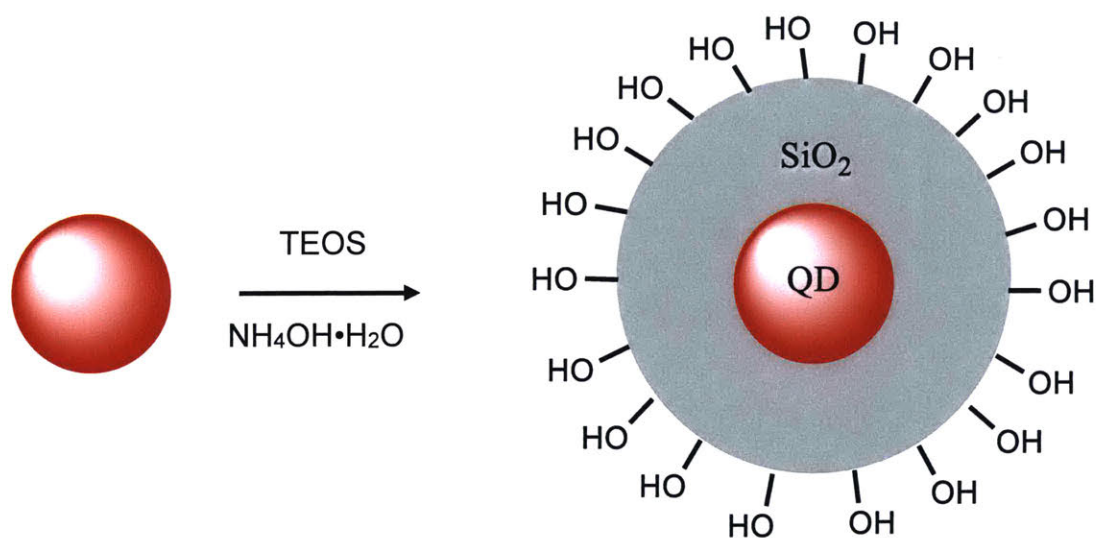
Figure 1-10. Schematic illustration of silica coating of QDs.

Overcoating hydrophobic nanocrystals with a silica shell also provides a universal method to render the nanocrystals water soluble.[50-51] Figure 1-10 shows the shell overcoating procedure. Usually, this process is carried out using a reverse microemulsion method (i.e. water-in-cyclohexane reverse microemulsion). Surfactant molecules form micelles in a hydrophobic solvent, and the addition of tetraethyl orthosilicate followed by ammonium hydroxide solution induces deposition of silica on QDs inside the micelles.[52] Moreover, this method enables straightforward surface functionalization *via* co-condensation between tetraethyl orthosilicate and another silane with the desired functional groups. However, the final size of the QD/silica is usually larger than

20 nm, and later functionalization will further increase the hydrodynamic diameter.[53] In addition, precise control of the final size of QD/silica particles is still challenging. Reaction parameters such as the size of the micelles, the concentration of the surfactant in the reaction solution, and the stirring speed will all influence the final size. Empty silica particles without QDs encapsulated or one silica particle with multiple QDs inside are difficult to avoid. Thus, producing high-quality water soluble QDs using this method is very challenging, and the resulting large hydrodynamic diameter limits the biological applications of QD/silica.

1.4.3 Ligand Replacement
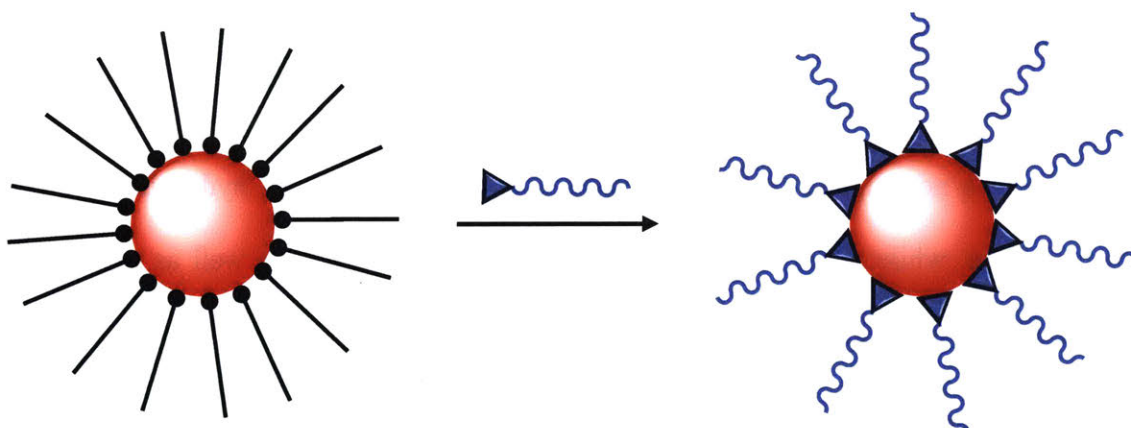
Figure 1-11. Schematic illustration of replacing the hydrophobic ligands on QD surfaces with hydrophilic molecules.

The stringent requirement on the small hydrodynamic diameter of QDs in numerous biological applications has drawn extensive attention to the ligand-substitution method. While substitution of native ligands with water-soluble molecules results in minimal change in size, significant loss of QY can result from the introduction of surface trap states.[54-55] Stability issues also exist. For example, thiolated monodentate ligands or DHLA-based bidentate ligands coated QDs would precipitate out within weeks because of the formation of disulfide bonds.[56] There are also reports about using multidentate polymers to replace the native ligands, which produces QDs with small

HDs, satisfactory QYs and minimal nonspecific binding.[56-59] However, these multidentate ligands are usually optimized for one single nanocrystal system, depending on the composition of the nanocrystal and the binding group of the native ligands.

1.5 Overview

Table 1-1 compares the above mentioned strategies to transfer as-synthesized hydrophobic QDs into aqueous solutions. In addition to the disadvantages listed, syntheses of water soluble QDs using these methods usually can only be carried out at a small scale, either limited by the method itself or the availability of the replacing ligands.[59-61] In order to promote QDs as fluorescent probes for biomedical imaging applications, a universal method to synthesize water-soluble QDs with a high QY, a compact size, good physiological stability, and at a larger scale is required. In this work, we will explore a new ligand system to realize convenient transfer of hydrophobic QDs into aqueous solutions, while maintaining a high QY and a compact size as well as rendering high physiological stability and flexible functionalization.

Table 1-1. Comparison of currently available methods to transfer hydrophobic QDs into aqueous solutions.

	Universal	QY	Stability	HD
Encapsulation	Yes	High	Moderate	Large
Silica coating	Yes	Moderate	Moderate	Large
Ligand replacement	No	Moderate-High	Poor (monodentate) Good (multidentate)	Small

References

1.   Efros, A. L.; Efros, A. L. Interband Absorption of Light in a Semiconductor Sphere *Sov Phys Semicond+* **1982,** *16,* 772-775.

2.   Brus, L. E. Electron Electron and Electron-Hole Interactions in Small Semiconductor Crystallites - the Size Dependence of the Lowest Excited Electronic State *J. Chem. Phys.* **1984,** *80,* 4403-4409.

3.   Bruns, O. T.; Bischof, T. S.; Harris, D. K.; Franke, D. K.; Shi, Y.; Riedemann, L.; Bartelt, A.; Jaworski, F. B.; Carr, J. A.; Rowlands, C. J., *et al.* Next-Generation in Vivo Optical Imaging with Short-Wave Infrared Quantum Dots *Nat. Biomed. Eng.* **2017,** *1,* 0056.

4.   Chen, O.; Zhao, J.; Chauhan, V. P.; Cui, J.; Wong, C.; Harris, D. K.; Wei, H.; Han, H. S.; Fukumura, D.; Jain, R. K., *et al.* Compact High-Quality Cdse-Cds Core-Shell Nanocrystals with Narrow Emission Linewidths and Suppressed Blinking *Nature Materials* **2013,** *12,* 445-451.

5.   Franke, D.; Harris, D. K.; Chen, O.; Bruns, O. T.; Carr, J. A.; Wilson, M. W. B.; Bawendi, M. G. Continuous Injection Synthesis of Indium Arsenide Quantum Dots Emissive in the Short-Wavelength Infrared *Nat. Commun.* **2016,** *7,* 12749.

6.   Wu, X. Y.; Liu, H. J.; Liu, J. Q.; Haley, K. N.; Treadway, J. A.; Larson, J. P.; Ge, N. F.; Peale, F.; Bruchez, M. P. Immunofluorescent Labeling of Cancer Marker Her2 and Other Cellular Targets with Semiconductor Quantum Dots *Nat. Biotechnol.* **2003,** *21,* 41-46.

7.   Murray, C. B.; Norris, D. J.; Bawendi, M. G. Synthesis and Characterization of Nearly Monodisperse Cde (E = S, Se, Te) Semiconductor Nanocrystallites *J. Am. Chem. Soc.* **1993,** *115,* 8706-8715.

8.   Peng, Z. A.; Peng, X. G. Formation of High-Quality Cdte, Cdse, and Cds Nanocrystals Using Cdo as Precursor *J. Am. Chem. Soc.* **2001,** *123,* 183-184.

9.   Yu, W. W.; Peng, X. G. Formation of High-Quality Cds and Other Ii-Vi Semiconductor Nanocrystals in Noncoordinating Solvents: Tunable Reactivity of Monomers *Angew. Chem., Int. Ed.* **2002,** *41,* 2368-2371.

10.   Dabbousi, B. O.; RodriguezViejo, J.; Mikulec, F. V.; Heine, J. R.; Mattoussi, H.; Ober, R.; Jensen, K. F.; Bawendi, M. G. (Cdse)Zns Core-Shell Quantum Dots: Synthesis and Characterization of a Size Series of Highly Luminescent Nanocrystallites *J. Phys. Chem. B* **1997,** *101,* 9463-9475.

11.   Kim, S.; Fisher, B.; Eisler, H. Y.; Bawendi, M. G. Novel Type-Ii Quantum Dots: Cdte/Cdse(Core/Shell) and Cdse/Znte(Core/Shell) Heterostructures. *Abstr Pap Am Chem S* **2002,** *224,* U443-U443.

12.   Peng, X. G.; Schlamp, M. C.; Kadavanich, A. V.; Alivisatos, A. P. Epitaxial Growth of Highly Luminescent Cdse/Cds Core/Shell Nanocrystals with Photostability and Electronic Accessibility *J. Am. Chem. Soc.* **1997,** *119,* 7019-7029.

13.   Reiss, P.; Bleuse, J.; Pron, A. Highly Luminescent Cdse/Znse Core/Shell Nanocrystals of Low Size Dispersion *Nano Lett.* **2002,** *2,* 781-784.

14.   Li, J. J.; Wang, Y. A.; Guo, W. Z.; Keay, J. C.; Mishima, T. D.; Johnson, M. B.; Peng, X. G. Large-Scale Synthesis of Nearly Monodisperse Cdse/Cds Core/Shell Nanocrystals Using Air-Stable Reagents Via Successive Ion Layer Adsorption and Reaction *J. Am. Chem. Soc.* **2003,** *125,* 12567-12575.

15.   Zhu, H. M.; Song, N. H.; Rodriguez-Cordoba, W.; Lian, T. Q. Wave Function Engineering for Efficient Extraction of up to Nineteen Electrons from One Cdse/Cds Quasi-Type Ii Quantum Dot *J. Am. Chem. Soc.* **2012,** *134,* 4250-4257.

16.   Aharoni, A.; Mokari, T.; Popov, I.; Banin, U. Synthesis of Inas/Cdse/Znse Core/Shell1/Shell2 Structures with Bright and Stable near-Infrared Fluorescence *J. Am. Chem. Soc.* **2006,** *128*, 257-264.

17.   Guzelian, A. A.; Banin, U.; Kadavanich, A. V.; Peng, X.; Alivisatos, A. P. Colloidal Chemical Synthesis and Characterization of Inas Nanocrystal Quantum Dots *Appl. Phys. Lett.* **1996,** *69*, 1432-1434.

18.   Uesugi, H.; Kita, M.; Omata, T. Synthesis of Size-Controlled Colloidal Inas Quantum Dots Using Triphenylarsine as a Stable Arsenic Source *J. Cryst. Growth* **2015,** *416*, 134-141.

19.   Xie, R. G.; Peng, X. G. Synthetic Scheme for High-Quality Inas Nanocrystals Based on Self-Focusing and One-Pot Synthesis of Inas-Based Core-Shell Nanocrystals *Angew. Chem., Int. Ed.* **2008,** *47*, 7677-7680.

20.   Kim, S.; Lim, Y. T.; Soltesz, E. G.; De Grand, A. M.; Lee, J.; Nakayama, A.; Parker, J. A.; Mihaljevic, T.; Laurence, R. G.; Dor, D. M., *et al.* Near-Infrared Fluorescent Type Ii Quantum Dots for Sentinel Lymph Node Mapping *Nat. Biotechnol.* **2004,** *22*, 93-97.

21.   Zimmer, J. P.; Kim, S. W.; Ohnishi, S.; Tanaka, E.; Frangioni, J. V.; Bawendi, M. G. Size Series of Small Indium Arsenide-Zinc Selenide Core-Shell Nanocrystals and Their Application to in Vivo Imaging *J. Am. Chem. Soc.* **2006,** *128*, 2526-2527.

22.   Liu, W. H.; Choi, H. S.; Zimmer, J. P.; Tanaka, E.; Frangioni, J. V.; Bawendi, M. Compact Cysteine-Coated Cdse(Zncds) Quantum Dots for in Vivo Applications *J. Am. Chem. Soc.* **2007,** *129*, 14530-14531.

23.   McDonald, S. A.; Konstantatos, G.; Zhang, S. G.; Cyr, P. W.; Klem, E. J. D.; Levina, L.; Sargent, E. H. Solution-Processed Pbs Quantum Dot Infrared Photodetectors and Photovoltaics *Nat. Mater.* **2005,** *4*, 138-142.

24.   Leschkies, K. S.; Divakar, R.; Basu, J.; Enache-Pommer, E.; Boercker, J. E.; Carter, C. B.; Kortshagen, U. R.; Norris, D. J.; Aydil, E. S. Photosensitization of Zno Nanowires with Cdse Quantum Dots for Photovoltaic Devices *Nano Lett*. **2007,** *7*, 1793-1798.

25.   Tang, J.; Kemp, K. W.; Hoogland, S.; Jeong, K. S.; Liu, H.; Levina, L.; Furukawa, M.; Wang, X. H.; Debnath, R.; Cha, D. K., *et al*. Colloidal-Quantum-Dot Photovoltaics Using Atomic-Ligand Passivation *Nat. Mater*. **2011,** *10*, 765-771.

26.   Caruge, J. M.; Halpert, J. E.; Wood, V.; Bulovic, V.; Bawendi, M. G. Colloidal Quantum-Dot Light-Emitting Diodes with Metal-Oxide Charge Transport Layers *Nat Photonics* **2008,** *2*, 247-250.

27.   Sun, L. F.; Choi, J. J.; Stachnik, D.; Bartnik, A. C.; Hyun, B. R.; Malliaras, G. G.; Hanrath, T.; Wise, F. W. Bright Infrared Quantum-Dot Light-Emitting Diodes through Inter-Dot Spacing Control *Nat Nanotechnol* **2012,** *7*, 369-373.

28.   Anikeeva, P. O.; Halpert, J. E.; Bawendi, M. G.; Bulovic, V. Quantum Dot Light-Emitting Devices with Electroluminescence Tunable over the Entire Visible Spectrum *Nano Lett*. **2009,** *9*, 2532-2536.

29.   Konstantatos, G.; Howard, I.; Fischer, A.; Hoogland, S.; Clifford, J.; Klem, E.; Levina, L.; Sargent, E. H. Ultrasensitive Solution-Cast Quantum Dot Photodetectors *Nature* **2006,** *442*, 180-183.

30.   Pan, D.; Towe, E.; Kennerly, S. Normal-Incidence Intersubband (in, Ga)as/Gaas Quantum Dot Infrared Photodetectors *Appl. Phys. Lett*. **1998,** *73*, 1937-1939.

31.   Jang, E.; Jun, S.; Jang, H.; Llim, J.; Kim, B.; Kim, Y. White-Light-Emitting Diodes with Quantum Dot Color Converters for Display Backlights *Adv. Mater*. **2010,** *22*, 3076-3080.

32.   Kim, T. H.; Cho, K. S.; Lee, E. K.; Lee, S. J.; Chae, J.; Kim, J. W.; Kim, D. H.; Kwon, J. Y.; Amaratunga, G.; Lee, S. Y., *et al.* Full-Colour Quantum Dot Displays Fabricated by Transfer Printing *Nat Photonics* **2011,** *5*, 176-182.

33.   Jaiswal, J. K.; Mattoussi, H.; Mauro, J. M.; Simon, S. M. Long-Term Multiple Color Imaging of Live Cells Using Quantum Dot Bioconjugates *Nat. Biotechnol.* **2003,** *21*, 47-51.

34.   Dahan, M.; Levi, S.; Luccardini, C.; Rostaing, P.; Riveau, B.; Triller, A. Diffusion Dynamics of Glycine Receptors Revealed by Single-Quantum Dot Tracking *Science* **2003,** *302*, 442-445.

35.   Voura, E. B.; Jaiswal, J. K.; Mattoussi, H.; Simon, S. M. Tracking Metastatic Tumor Cell Extravasation with Quantum Dot Nanocrystals and Fluorescence Emission-Scanning Microscopy *Nat Med* **2004,** *10*, 993-998.

36.   Courty, S.; Luccardini, C.; Bellaiche, Y.; Cappello, G.; Dahan, M. Tracking Individual Kinesin Motors in Living Cells Using Single Quantum-Dot Imaging *Nano Lett.* **2006,** *6*, 1491-1495.

37.   Resch-Genger, U.; Grabolle, M.; Cavaliere-Jaricot, S.; Nitschke, R.; Nann, T. Quantum Dots Versus Organic Dyes as Fluorescent Labels *Nature Methods* **2008,** *5*, 763-775.

38.   Derfus, A. M.; Chan, W. C. W.; Bhatia, S. N. Intracellular Delivery of Quantum Dots for Live Cell Labeling and Organelle Tracking *Adv. Mater.* **2004,** *16*, 961-966.

39.   Cui, B. X.; Wu, C. B.; Chen, L.; Ramirez, A.; Bearer, E. L.; Li, W. P.; Mobley, W. C.; Chu, S. One at a Time, Live Tracking of Ngf Axonal Transport Using Quantum Dots *Proc. Natl. Acad. Sci. U.S.A.* **2007,** *104*, 13666-13671.

40.   Strack, R. Highly Multiplexed Imaging *Nat. Methods* **2016,** *13*, 35-35.

41.   Han, M. Y.; Gao, X. H.; Su, J. Z.; Nie, S. Quantum-Dot-Tagged Microbeads for Multiplexed Optical Coding of Biomolecules *Nat. Biotechnol.* **2001,** *19*, 631-635.

42.   So, M. K.; Xu, C. J.; Loening, A. M.; Gambhir, S. S.; Rao, J. H. Self-Illuminating Quantum Dot Conjugates for in Vivo Imaging *Nat. Biotechnol.* **2006,** *24*, 339-343.

43.   Medintz, I. L.; Uyeda, H. T.; Goldman, E. R.; Mattoussi, H. Quantum Dot Bioconjugates for Imaging, Labelling and Sensing *Nature Materials* **2005,** *4*, 435-446.

44.   Hong, G. S.; Diao, S.; Chang, J. L.; Antaris, A. L.; Chen, C. X.; Zhang, B.; Zhao, S.; Atochin, D. N.; Huang, P. L.; Andreasson, K. I., *et al*. Through-Skull Fluorescence Imaging of the Brain in a New near-Infrared Window *Nature Photonics* **2014,** *8*, 723-730.

45.   Bardhan, N. M.; Ghosh, D.; Belcher, A. M. Carbon Nanotubes as in Vivo Bacterial Probes *Nat. Commun.* **2014,** *5*, 4918.

46.   Pellegrino, T.; Manna, L.; Kudera, S.; Liedl, T.; Koktysh, D.; Rogach, A. L.; Keller, S.; Radler, J.; Natile, G.; Parak, W. J. Hydrophobic Nanocrystals Coated with an Amphiphilic Polymer Shell: A General Route to Water Soluble Nanocrystals *Nano Lett.* **2004,** *4*, 703-707.

47.   Petruska, M. A.; Bartko, A. P.; Klimov, V. I. An Amphiphilic Approach to Nanocrystal Quantum Dot-Titania Nanocomposites *J. Am. Chem. Soc.* **2004,** *126*, 714-715.

48.   Anderson, R. E.; Chan, W. C. W. Systematic Investigation of Preparing Biocompatible, Single, and Small Zns-Capped Cdse Quantum Dots with Amphiphilic Polymers *ACS Nano* **2008,** *2*, 1341-1352.

49.   Smith, A. M.; Duan, H. W.; Rhyner, M. N.; Ruan, G.; Nie, S. M. A Systematic Examination of Surface Coatings on the Optical and Chemical Properties of Semiconductor Quantum Dots *Phys. Chem. Chem. Phys.* **2006,** *8*, 3895-3903.

50.   Gerion, D.; Pinaud, F.; Williams, S. C.; Parak, W. J.; Zanchet, D.; Weiss, S.; Alivisatos, A. P. Synthesis and Properties of Biocompatible Water-Soluble Silica-Coated Cdse/Zns Semiconductor Quantum Dots *J. Phys. Chem. B* **2001,** *105,* 8861-8871.

51.   Guerrero-Martinez, A.; Perez-Juste, J.; Liz-Marzan, L. M. Recent Progress on Silica Coating of Nanoparticles and Related Nanomaterials *Adv. Mater.* **2010,** *22,* 1182-1195.

52.   Selvan, S. T.; Tan, T. T.; Ying, J. Y. Robust, Non-Cytotoxic, Silica-Coated Cdse Quantum Dots with Efficient Photoluminescence *Adv. Mater.* **2005,** *17,* 1620-1625.

53.   Koole, R.; van Schooneveld, M. M.; Hilhorst, J.; Donega, C. D.; 't Hart, D. C.; van Blaaderen, A.; Vanmaekelbergh, D.; Meijerink, A. On the Incorporation Mechanism of Hydrophobic Quantum Dots in Silica Spheres by a Reverse Microemulsion Method *Chem. Mater.* **2008,** *20,* 2503-2512.

54.   Zhang, Y. J.; Clapp, A. Overview of Stabilizing Ligands for Biocompatible Quantum Dot Nanocrystals *Sensors* **2011,** *11,* 11036-11055.

55.   Jeong, S.; Achermann, M.; Nanda, J.; Lvanov, S.; Klimov, V. I.; Hollingsworth, J. A. Effect of the Thiol-Thiolate Equilibrium on the Photophysical Properties of Aqueous Cdse/Zns Nanocrystal Quantum Dots *J. Am. Chem. Soc.* **2005,** *127,* 10126-10127.

56.   Liu, W. H.; Greytak, A. B.; Lee, J.; Wong, C. R.; Park, J.; Marshall, L. F.; Jiang, W.; Curtin, P. N.; Ting, A. Y.; Nocera, D. G., *et al.* Compact Biocompatible Quantum Dots Via Raft-Mediated Synthesis of Imidazole-Based Random Copolymer Ligand *J. Am. Chem. Soc.* **2010,** *132,* 472-483.

57.   Zhang, P. F.; Liu, S. H.; Gao, D. Y.; Hu, D. H.; Gong, P.; Sheng, Z. H.; Deng, J. H.; Ma, Y. E.; Cai, L. T. Click-Functionalized Compact Quantum Dots Protected by Multidentate-Imidazole Ligands: Conjugation-Ready Nanotags for Living-Virus Labeling and Imaging *J. Am. Chem. Soc.* **2012,** *134,* 8388-8391.

58.   Zhan, N. Q.; Palui, G.; Mattoussi, H. Preparation of Compact Biocompatible Quantum Dots Using Multicoordinating Molecular-Scale Ligands Based on a Zwitterionic Hydrophilic Motif and Lipoic Acid Anchors *Nat. Protoc.* **2015,** *10,* 859-874.

59.   Wang, W. T.; Ji, X.; Kapur, A.; Zhang, C. Q.; Mattoussi, H. A Multifunctional Polymer Combining the Imidazole and Zwitterion Motifs as a Biocompatible Compact Coating for Quantum Dots *J. Am. Chem. Soc.* **2015,** *137,* 14158-14172.

60.   Park, J.; Lee, J.; Kwag, J.; Baek, Y.; Kim, B.; Yoon, C. J.; Bok, S.; Cho, S. H.; Kim, K. H.; Ahn, G. O.*, et al.* Quantum Dots in an Amphiphilic Polyethyleneimine Derivative Platform for Cellular Labeling, Targeting, Gene Delivery, and Ratiometric Oxygen Sensing *ACS Nano* **2015,** *9,* 6511-6521.

61.   Popovic, Z.; Liu, W. H.; Chauhan, V. P.; Lee, J.; Wong, C.; Greytak, A. B.; Insin, N.; Nocera, D. G.; Fukumura, D.; Jain, R. K.*, et al.* A Nanoparticle Size Series for in Vivo Fluorescence Imaging *Angew. Chem., Int. Ed.* **2010,** *49,* 8649-8652.

Chapter 2

A New Ligand System for Convenient Phase Transfer of QDs

2.1 Design of a Norbornene-bearing Ligand

As mentioned in Chapter 1, synthesizing water-soluble QDs at a large scale while maintaining a high QY and a compact size remains challenging. Our goal in this study is to develop an efficient system for water solubilization and flexible functionalization of carboxylate ligand-passivated QDs. In order to obtain water-soluble QDs for biomedical imaging applications at a larger scale, we evaluated whether incorporation of a clickable moiety at the end of native ligands and further conjugation of a hydrophilic agent would allow phase transfer of QDs while maintaining a high QY and a small hydrodynamic diameter.

Importantly, we placed emphasis on a ligand system that would not alter the native ligands on the nanocrystal surface post-synthesis in order to maintain high QYs. To minimize the size of the resulting QDs in water, we decided to link hydrophilic moieties to the native hydrophobic ligands *via* covalent bonds rather than Van der Waals forces between the native hydrophobic ligands and an amphiphilic polymer.[1] Norbornene has been demonstrated to undergo highly efficient and bio-orthogonal click reactions with tetrazine.[2-3] Thus, we chose this group as the clickable moiety to link the native ligand to a tetrazine-bearing hydrophilic molecule *via* a covalent bond. The main ligand species for a broad range of QDs are carboxylate based ligands,[4-6] as the carboxyl group exhibits a strong binding affinity to cadmium, zinc, lead, and other common QD metals, so the
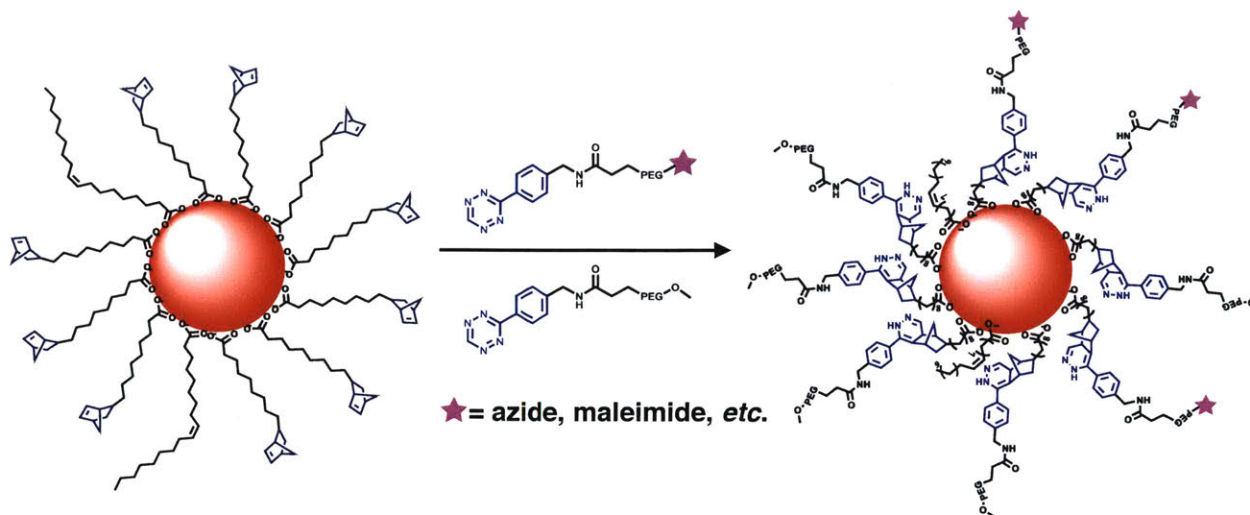
Scheme 2-1. Schematic illustration of water solubilization and flexible functionalization of 5-norbornene-2-nonanoic acid capped QDs *via* norbornene-tetrazine click chemistry.

carboxyl group was chosen as the binding group to QD surfaces. Considering the cost and availability of reagents, we designed the ligand 5-norbornene-2-nonanoic acid, later referred to as NB-nonanoic acid (Scheme 2-1), as the native ligand to be introduced during QD syntheses.

As shown in Scheme 2-1, the as-synthesized QDs are capped with NB-nonanoic acid. Upon clicking with tetrazine-bearing polyethylene glycol (PEG), the QDs are readily soluble in aqueous solutions. Further functionalization and conjugation of QDs can be achieved through the incorporation of functional groups (azide, maleimide, biotin, thiol, acrylate, *etc.*) at the other terminus of the PEG chains, and the number and ratio of functional groups on the QD surface can be readily controlled. In summary, by incorporating a "clickable" moiety (the norbornene group) to a ligand that can be added during QD syntheses and bind to QD surfaces, we can realize convenient phase transfer of hydrophobic QDs into aqueous solutions as well as versatile functionalization by clicking with a hydrophilic molecule *via* norbornene/tetrazine click chemistry.

2.2 Synthesis of NB-nonanoic Acid[7]
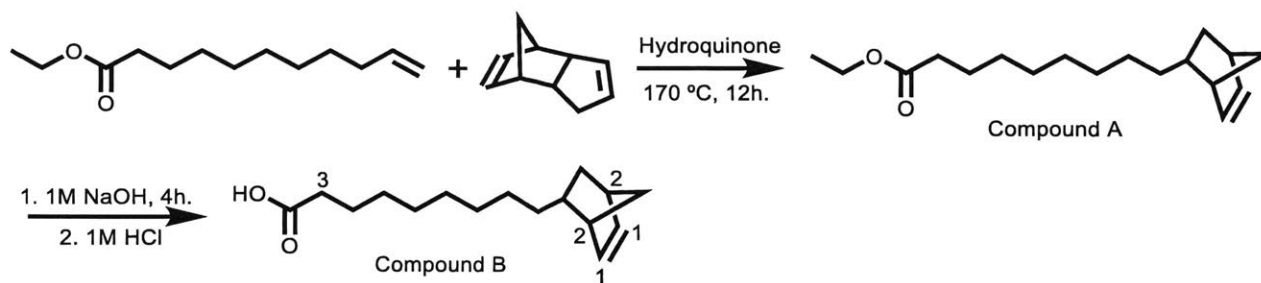
Figure 11. Synthetic route to NB-nonanoic acid.

Figure 2-1 shows the synthetic route to NB-nonanoic acid. The details are provided as follows.

2.2.1 Synthesis of Compound A (ethyl 10-(norborn-2-en-5-yl)decanoate)

A pressure vessel is used in this reaction, and a blast shield is recommended. To a 65 mL pressure vessel, dicyclopentadiene (15.73 g, 0.119 mol), ethyl undecylenate (30.30 g, 0.143 mol) and hydroquinone (39.3 mg, 0.36 mmol) were added. After sealing the vessel with a Teflon valve, the mixture was brought up to 170 °C in an oil bath and left stirring for 20 h. The reaction solution was then allowed to cool down and distilled under vacuum (200 mTorr). The fraction (vapor temperature: 120-130 °C) containing Compound A was collected and set aside for 4 h. A solid side-product precipitated out of the solution and was removed using a fritted glass filter funnel. The filtrate was stored at 4 °C overnight to induce a secondary precipitation, and another filtration step yielded a colorless clear oil (7.69 g, 0.028 mol, 19% yield). The ^{1}H Nuclear Magnetic Resonance (NMR) spectrum shows the ratio of exo and endo products as 2:8 (Figure 2-2). NMR peaks of the major isomer (endo): ^{1}H NMR (400MHz, CDCl$_3$) δ (ppm) 6.09 (m, 1H), 5.89 (m, 1H), 4.11 (q, J=7.6 Hz, 2H), 2.73 (m, 2H), 2.27 (t, J=7.4 Hz, 2H), 1.94 (m, 1H), 1.81 (m, 1H), 1.60 (m,

2H), 1.38-1.22 (br, 11H), 1.24 (t, J=7.1 Hz, 3H), 1.19 (d, J=8.0 Hz, 1H), 1.03 (m, 2H), 0.47 (m, 1H); ^{13}C NMR (100MHz, CDCl₃) δ (ppm) 174.0, 137.0, 132.6, 60.3, 49.7, 45.5, 42.6, 38.9, 34.9, 34.5, 32.6, 30.0, 29.6, 29.4, 29.3, 28.7, 25.1, 14.4.
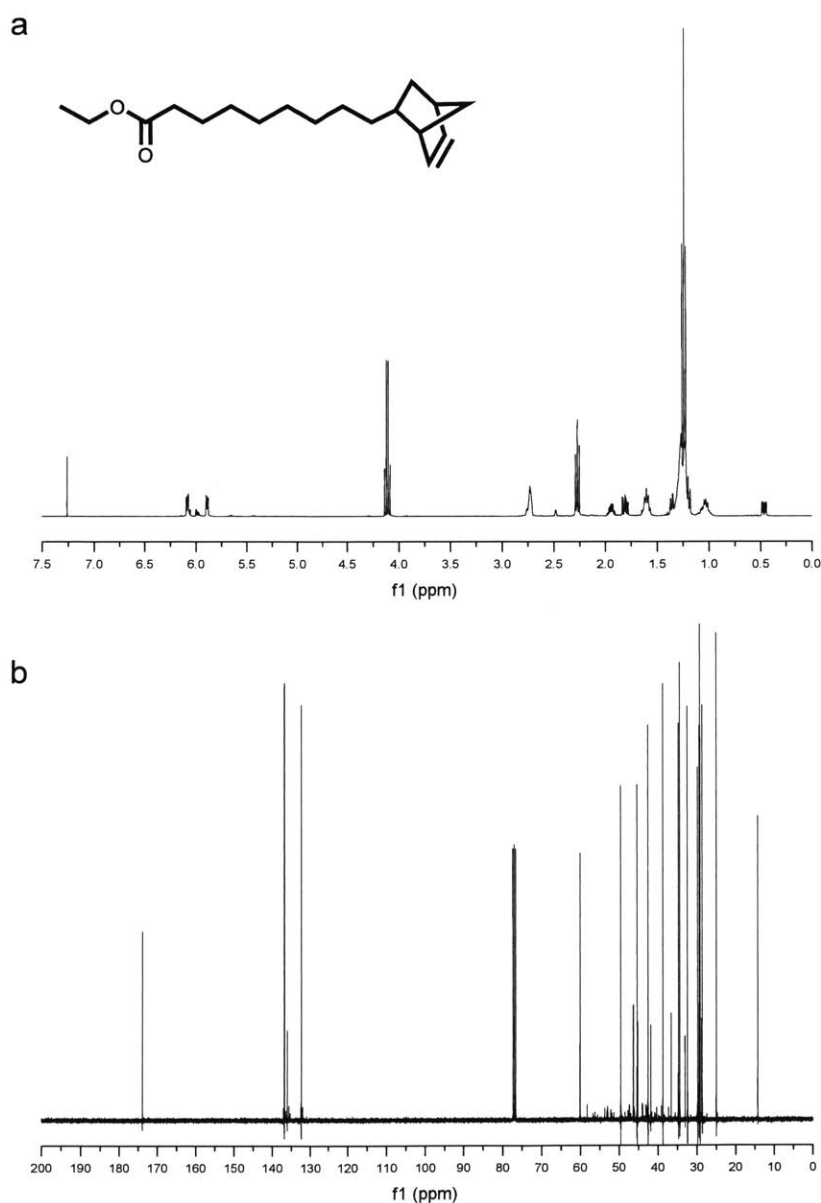
Figure 2-2. (a) ^{1}H NMR spectrum and (b) ^{13}C NMR spectrum of the intermediate Compound A (ethyl 10-(norborn-2-en-5-yl)decanoate).

2.2.2 Synthesis of Compound B (NB-nonanoic acid)
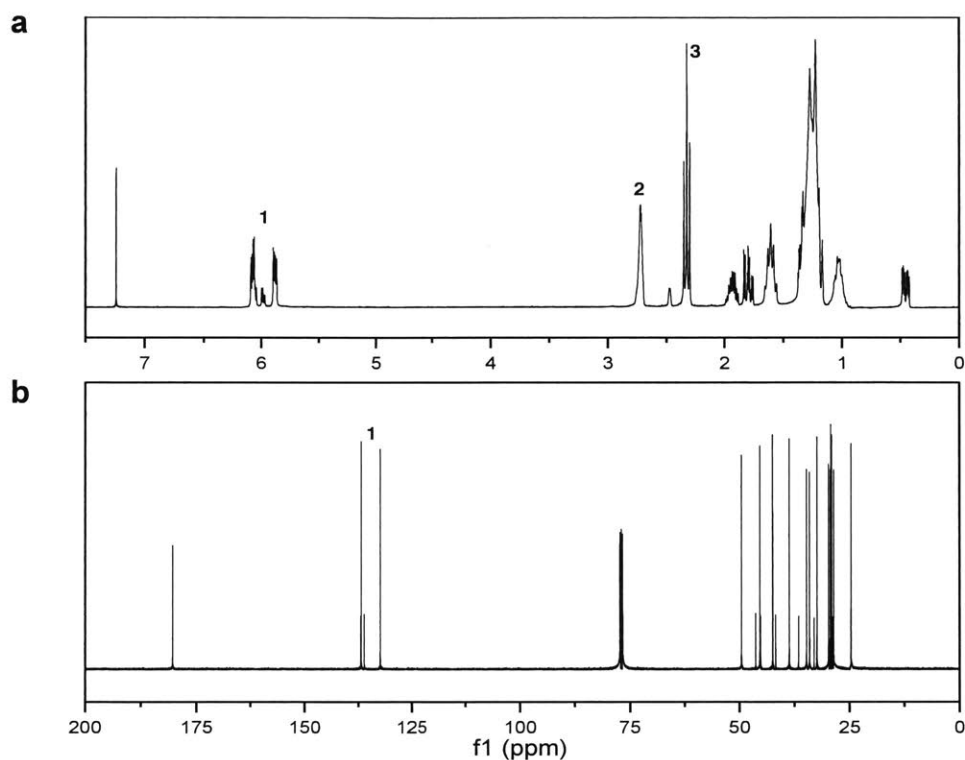
Figure 2-3. (a) ^{1}H NMR spectrum of NB-nonanoic acid. The peaks marked 1, 2, and 3 are corresponding to the protons marked on the structure of the molecule in Figure 2-1. (b) ^{13}C NMR spectrum of NB-nonanoic acid.

While stirring, 6.81g (0.024 mol) of Compound A was added dropwise to 1M solution of NaOH in methanol (105 mL). After 4 h, the solution was transferred into a separatory funnel and washed three times with 150 mL of hexanes to remove any unreacted material and side-products. The pH of the methanol phase was then adjusted to 3 using 1M HCl aqueous solution, and the product was extracted into hexanes (3×150 mL). The combined 450 mL of hexanes containing Compound B was dried over Na_2SO_4, and the solvent was evaporated under reduced pressure to obtain NB-nonanoic acid as a white solid (2.82g, 0.011mol, 47% yield). The ^{1}H NMR spectrum shows the ratio of exo and endo products as 2:8 (Figure 2-3). NMR peaks of the major isomer (endo): ^{1}H NMR (400MHz, CDCl$_3$) δ (ppm) 11.53 (br, 1H), 6.10 (m, 1H), 5.90 (m, 1H), 2.74 (m, 2H), 2.34

47

(t, J=7.4 Hz, 2H), 1.96 (m, 1H), 1.82 (m, 1H), 1.63 (m, 2H), 1.39-1.23 (br, 11H), 1.20 (d, J=8.0 Hz, 1H), 1.04 (m, 2H), 0.48 (m, 1H); ^{13}C NMR (100MHz, CDCl$_3$) δ (ppm) 180.5, 137.0, 132.6, 49.7, 45.5, 42.7, 38.9, 34.9, 34.2, 32.6, 30.0, 29.6, 29.4, 29.2, 28.8, 24.8.

We have successfully performed this synthesis at six times the scale described above and have obtained similar reaction yields.

2.3 Thermo-stability of NB-nonanoic Acid
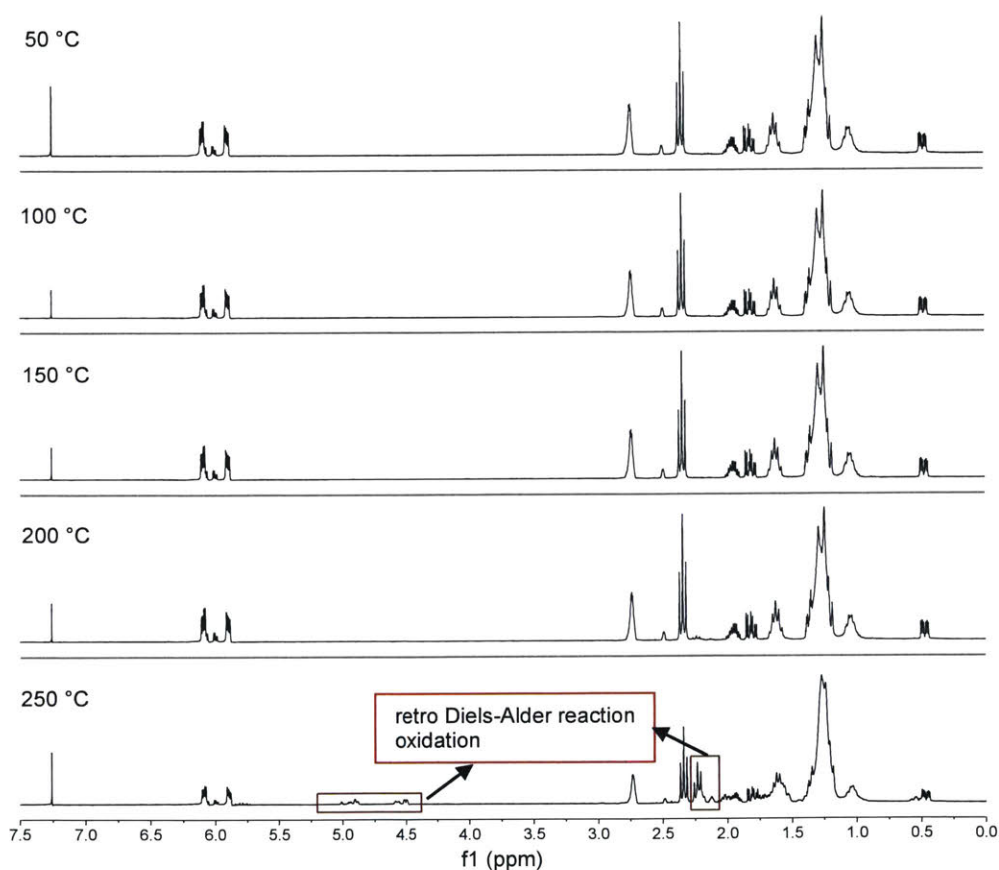
Figure 2-4. ^{1}H NMR spectra of NB-nonanoic acid. Each spectrum corresponds to an aliquot that was incubated up to a particular temperature (50 °C, 100 °C, 150 °C, and 200 °C) and kept at that temperature for 40 min. Signs of the retro Diels-Alder reaction and oxidation start to become evident at temperatures above 200 °C (indicated in the red rectangular box).

Because QD syntheses are usually conducted at a high temperature of over 200 °C, we studied the thermo-stability of NB-nonanoic acid by heating the molecule up stepwise and tracking structural changes using ^{1}H NMR spectroscopy. As shown in Figure 2-4, the ligand is stable up to 200 °C, and the norbornene moiety undergoes a retro-Diels-Alder decomposition beyond that point. Thus, for QD syntheses that are performed higher than 200 °C (CdSe/CdS QDs, CdSe/ZnS QDs, etc.), the ligand is added as the final step when the reaction solution cools down to below 200 °C; for syntheses that are performed lower than 200 °C (PbS QDs), NB-nonanoic acid is added in the form of metal carboxylate.

2.4 Syntheses of NB-nonanoic Acid-capped QDs

We applied the NB-nonanoic ligand to our recently described CdSe/CdS QDs, which are synthesized at 310 °C, by modifying the published method.[8] Briefly, 100 nmol of CdSe QDs were added to a mixture of 1-octadecene (ODE, 3 mL) and oleylamine (3 mL). The reaction solution was degassed under vacuum at room temperature for 1 h and at 120 °C for 20 min. The solution was then heated to 310 °C under nitrogen flow, and a desired amount of cadmium (II) oleate (1.5 mL of 0.2M Cd-oleate, diluted in 3 mL ODE) and octanethiol (1.2 equivalents with respect to Cd-oleate, diluted in 3 mL ODE) were injected dropwise into the reaction solution at 1.5 mL/h using a syringe pump when the temperature reached 240 °C. The QDs were annealed at 310 °C for 30 min after precursor infusion before cooling to 150 °C. 2 grams of NB-nonanoic acid dissolved in 2 mL of ODE was injected, and QDs were annealed at 150 °C for 1 h. The resulting CdSe/CdS QDs were precipitated by adding acetone and then redispersed in hexanes twice. For ligand addition to existing QDs, QD-norbornene were synthesized by adding NB-nonanoic acid to QDs dispersed in toluene, and the mixture was stirred in a 70 °C oil bath for 2 h. The resulting CdSe/CdS QDs were precipitated out by adding methanol and redispersed in chloroform.

We performed ^{1}H NMR to confirm that the NB-nonanoic acid ligands are bound to QD surfaces. For a more precise analysis, we did a secondary purification using a home-built dialysis setup (Figure 2-5) that can efficiently remove free unbound ligands prior to ^{1}H NMR analysis. The ^{1}H NMR spectrum of the QDs shows broadening and loss of resolved splitting of all the resonance peaks of NB-nonanoic acid (Figure 2-6 insets as an example) as well as loss of the α-proton Peak 3, indicating that the NB-nonanoic acid ligands are bound to the surface of QDs.[9-11]
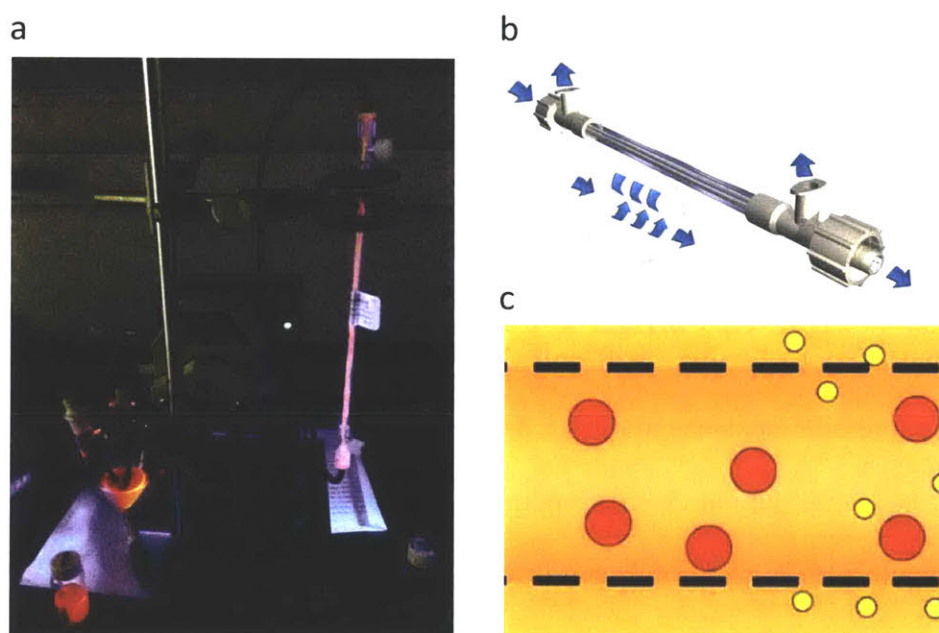
Figure 2-5. (a) A home-built setup to purify QDs by allowing small molecules to diffuse out of the porous fiber filters. This setup includes a Masterflex L/S series peristaltic pump from Cole Palmer and a MicroKros® hollow fiber filter from Spectrum Labs. (b,c) Schematic illustration of the purification process. The filter consists of several porous fiber tubes inside a larger plastic tube. The QD solution flows inside the fiber tubes, while solvent containing small molecules diffuses out, and is collected. After evaporating the collected solvent, the mass of the residue (small molecules that diffused out of the fiber tubes) can be weighed. Our QD solution was purified on this system until no small molecules were detected. This setup provides a mild way to purify QDs, and the process can be easily scaled up.
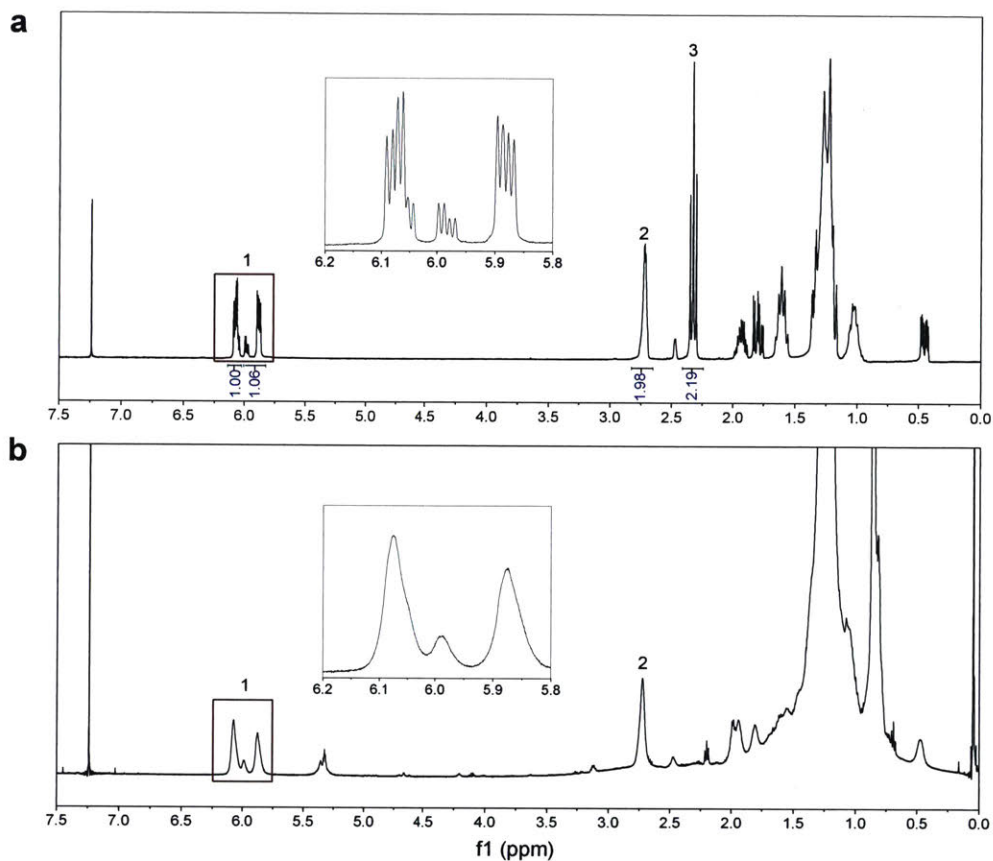
Figure 2-6. ^{1}H NMR spectrum of (a) NB-nonanoic acid and (b) NB-nonanoic acid capped CdSe/CdS QDs (insets are zoomed-in areas indicated in the red box).

Syntheses of NB-nonanoic acid capped CdSe/CdS nanorods, InAs/CdSe/ZnS QDs, and PbS QDs are provided in the experimental details.

2.5 NB-nonanoic Acid to Oleic Acid Ratio on QD Surfaces

The final ratio of NB-nonanoic acid to the competing oleic acid ligands on the QD surfaces was also investigated. After careful analysis, we note that a very small amount of oleylamine exists in the QD solution, as shown in Figure 2-7. The α-proton peaks of oleylamine are visible on the ^{1}H NMR spectrum of QD-norbornene. However, the splitting of the peaks is still well resolved, and the coupling constant remains the same. Thus we conclude that the little amount of oleylamine in
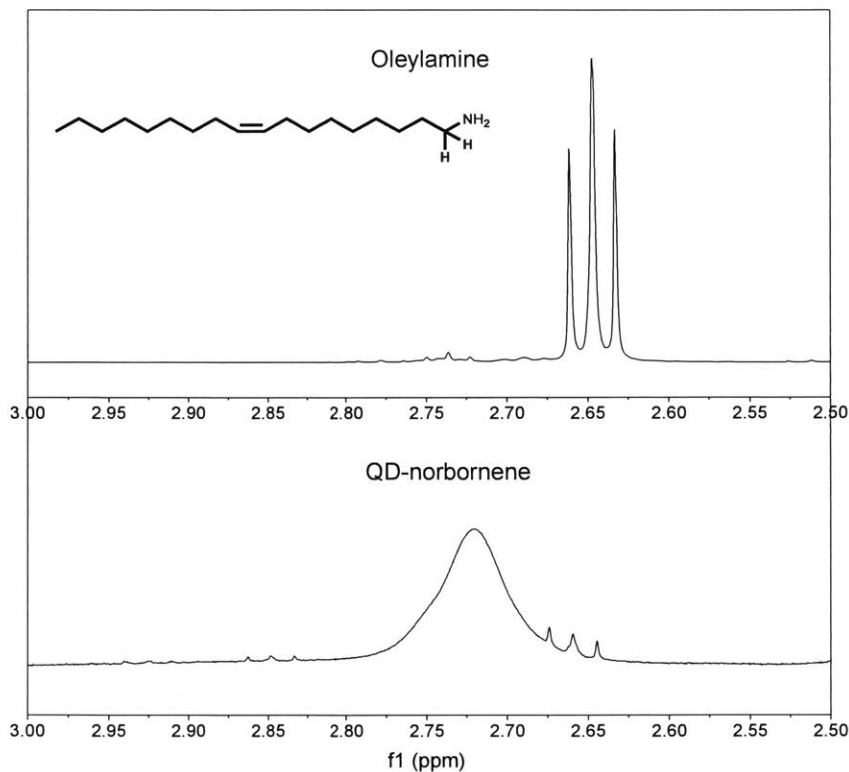
Figure 2-7. Zoomed-in ¹H NMR spectra of oleylamine and QD-norbornene.

the QD-norbornene solution is not bound to QD surfaces. By integrating the peaks of double bond

protons (NB-nonanoic acid: 5.8-6.2 ppm, oleic acid: 5.3 ppm) on Figure 2-6b, we obtained a

quantitative NB-nonanoic acid to oleic acid ratio of 4:1. Thus, we conclude that NB-nonanoic acid

accounts for about 80% of the capping ligands on QD surfaces. We used ¹H NMR spectroscopy to

study the effect of the annealing temperature on final ligand ratios between 50 °C and 200 °C

(Figure 2-8). As shown in Figure 2-9, when the annealing temperature is higher than 100 °C, the

NB-nonanoic acid to oleic acid ratio on QD surfaces remains constant as 4:1, which is similar to

the ratio of the ligands that were added to the reaction solution (4.2:1) (see Figure 2-8 description).

This finding is consistent with a Langmuir-like binding behavior, assuming a similar binding

equilibrium constant for the two carboxylate ligands. In contrast, our data indicates that annealing

at 50 °C for one hour does not provide the needed activation energy to overcome a Cd-oleate bond. We chose an annealing temperature of 150 °C for all following syntheses.
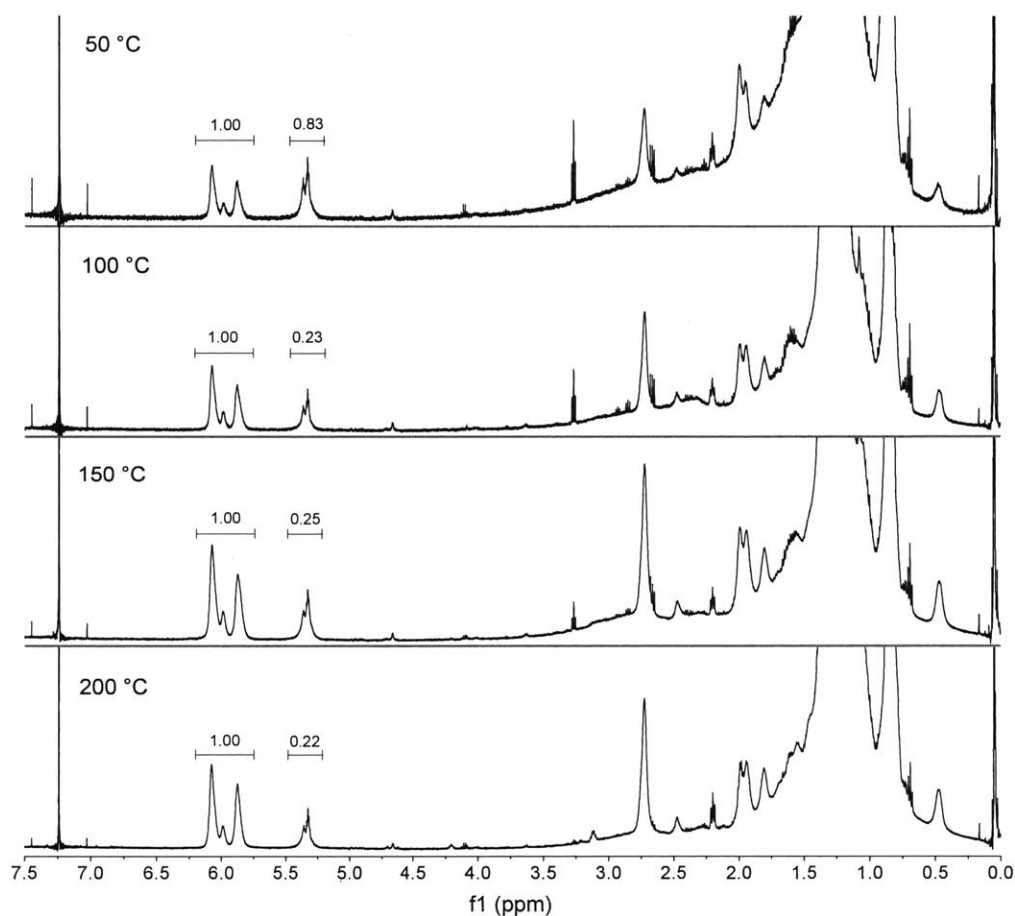
Figure 2-8. ^{1}H NMR of QD-norbornene at different annealing temperatures. The peaks at 5.8-6.2 ppm correspond to the carbon-carbon double bond protons of the norbornene group, and the peaks at 5.35 ppm correspond to the double bond protons of oleic acid.

*Calculation of the ratio of NB-nonanoic acid to oleate species added to the reaction solution: 0.2 M Cd-oleate was synthesized by dissolving CdO (2.5746 g, 0.02 mol) in 40 mL oleic acid, followed by adding ODE to make the total volume 100 mL. 1.5 mL of 0.2 M Cd-oleate was used as the cadmium precursor, which corresponds to 1.5*40/100=0.6 mL oleic acid (0.0019 mol oleate

species, including Cd-oleate and free oleic acid). 2.0 g of NB-nonanoic acid (0.008 mol) was added

to the reaction solution. So the NB-nonanoic acid to oleate ratio in the reaction solution is 4.2:1.
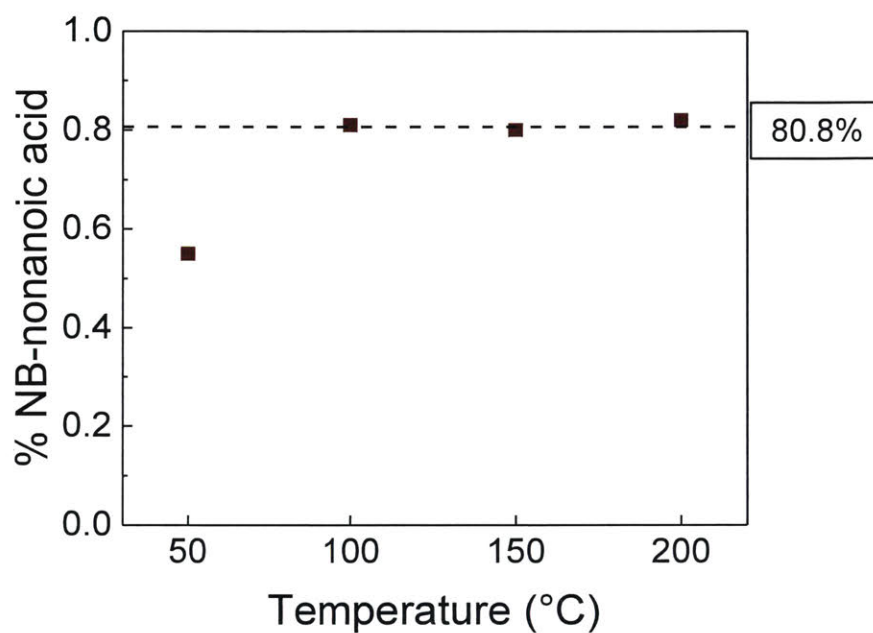
Figure 2-9. NB-nonanoic acid percentage on CdSe/CdS QD surface at different annealing temperatures when a 4.2:1 NB-nonanoic acid to oleate species molar ratio is added in the reaction solution.

2.6 Phase Transfer of QD-norbornene
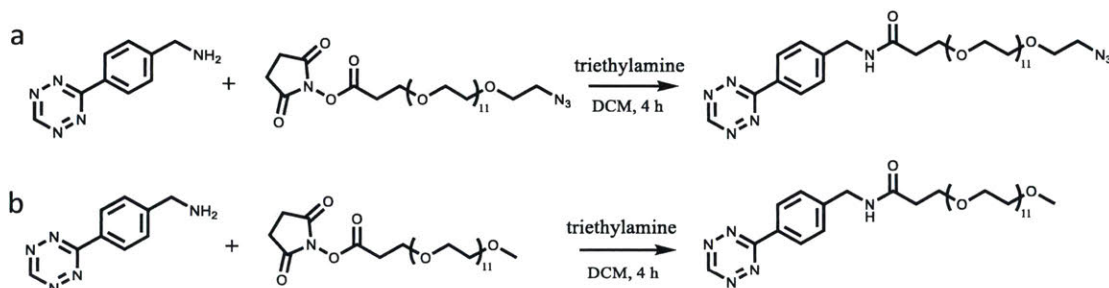
Figure 2-10. Synthetic routes to Tetrazine-PEG-N$_3$ and Tetrazine-PEG-OMe.
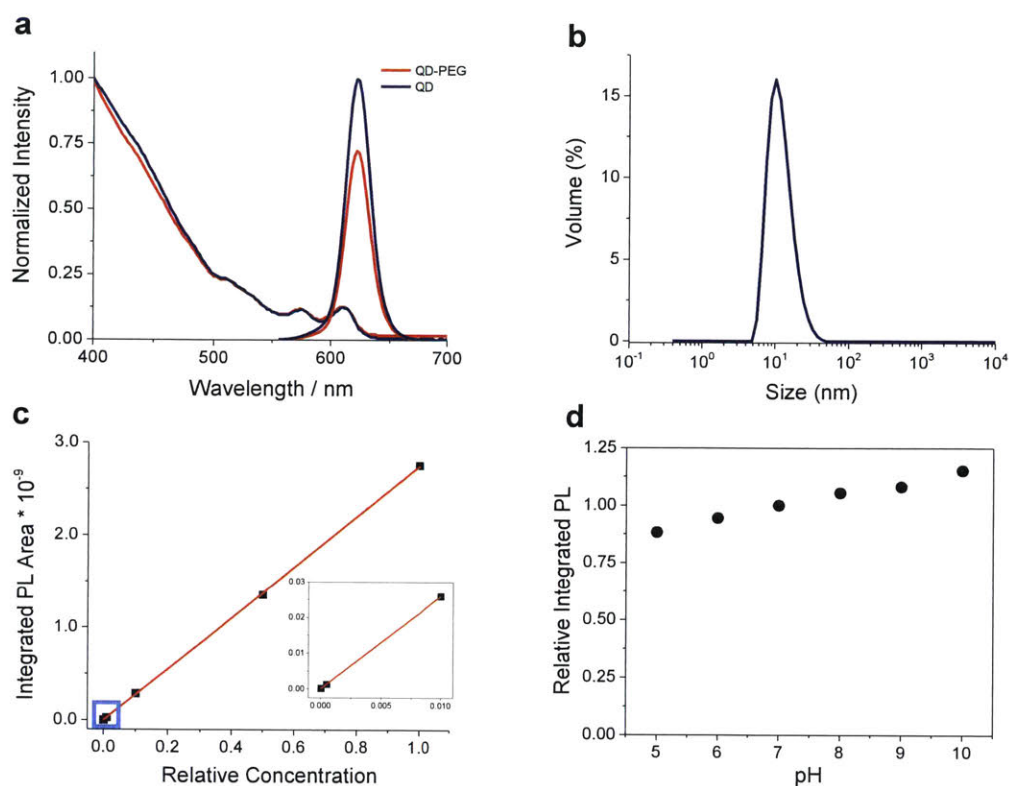
Figure 2-11. (a) Absorption and photoluminescence (PL) spectra of CdSe/CdS QDs before (blue) and after (red) water solubilization. PL intensities were adjusted according to QYs. (b) DLS measurement of water soluble CdSe/CdS QDs. (c) Linear relationship between integrated PL and relative concentrations of water-soluble CdSe/CdS QDs; inset is a zoomed-in area indicated by the blue rectangle. (d) Colloidal stability test of water soluble CdSe/CdS QDs at different pH values (5-10).

After demonstrating the synthesis of NB-nonanoic acid capped "clickable" CdSe/CdS QDs (QD-norbornene), we investigated the subsequent reaction with tetrazine-PEG to make the QDs water soluble. Tetrazine-PEG-OMe and tetrazine-PEG-N$_3$ were synthesized according to Figure 2-10, followed by purification using a silica column. QD-norbornene in chloroform was added to a mixture of tetrazine-PEG-OMe and tetrazine-PEG-N$_3$. Upon phase transfer to aqueous solution, we detected a negligible change in the QD absorption and PL spectra but a drop in the PL QY from close to 100% to about 70% (Figure 2-11a). Our approach preserves ~70% of the original QY,

which is comparable to other methods but yields a higher absolute QY value.[12-14] Dynamic light scattering (DLS) measurements show a hydrodynamic diameter (HD) of 12 nm (Figure 2-11b), which is about 3 nm larger than the inorganic core (Figure 2-12), a reasonable diameter increase caused by the NB-nonanoic acid and PEG_{12} chains. The resulting water soluble QDs are stable against serial dilution with phosphate buffered saline (PBS), with the integrated emission remaining linear over 3 decades of dilution (Figure 2-11c). This indicates a strong binding constant between the ligands and inorganic core,[15] resulting in high colloidal stability that is essential for biological applications where very dilute samples are used. We also investigated the stability of our QD dispersions with respect to the physiological pH range. The integrated PL intensity of the solutions decreases slightly with decreasing pH, presumably due to the protonation of NB-nonanoic acid and loss of ligand at lower pH (Figure 2-11d). Our characterization shows that our novel ligand system generates water soluble CdSe/CdS QDs with a small HD, a high QY, and good colloidal stability.
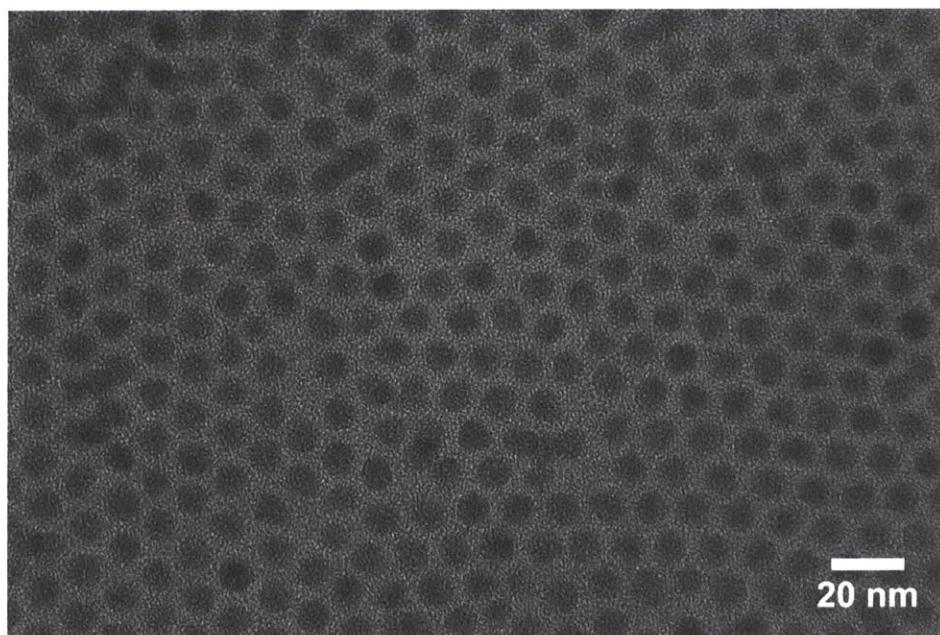
Figure 2-12. Transmission electron microscopy (TEM) image of CdSe/CdS QDs.

2.7 A Universal Ligand

We highlight that our new ligand system not only achieves promising results for our recently described CdSe/CdS QDs,[8] but that it can also be readily applied to other carboxylate ligand-stabilized nanocrystal systems, including CdSe/CdS nanorods, CdSe/ZnS QDs, InAs/CdSe/CdS QDs, and PbS QDs. After clicking with hydrophilic agents, the emission spectra of those water-soluble nanostructures cover a broad wavelength range from the visible to the infrared (Figure 2-13), and their QYs are well maintained (Table S1). These water-soluble QDs are promising candidate probes for multiplexed imaging applications, and InAs- and PbS-based QDs, especially, have received recent attention as emissive materials for *in vivo* imaging in the short-wave infrared.[16-17]
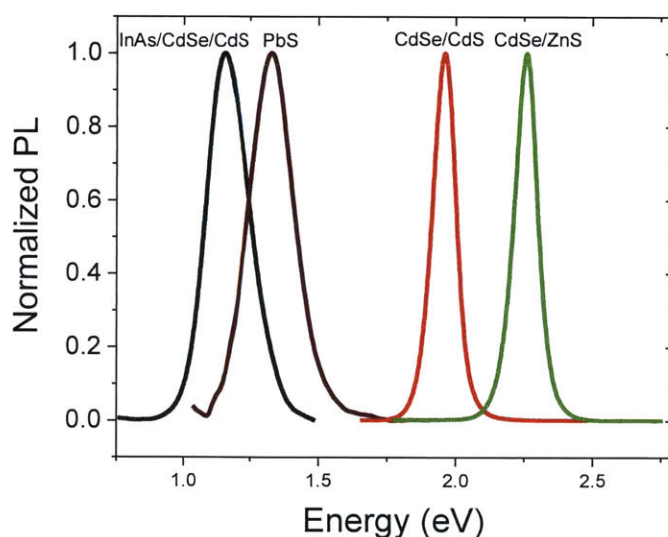
Figure 2-13. Emission spectra of CdSe/ZnS QDs, CdSe/CdS nanorods, PbS QDs, and InAs/CdSe/CdS QDs in aqueous solutions.

Table 2-1. QYs of several NB-nonanoic acid capped nanocrystals before and after water solublization.

QY(%)	CdSe/ZnS QDs (Em: 545 nm)	InAs/CdSe/CdS QDs (Em: 1080 nm)	CdSe/CdS Nanorods (Em: 630 nm)	PbS QDs (Em: 980 nm)
As synthesized	>95	28	92	73
In water	57	22	50	40

2.8 Experimental Details

Materials

Dicyclopentadiene, ethyl undecylenate (97%), hydroquinone (99%), 1-octadecene (ODE, 90%), trioctylphosphine oxide (TOPO 99%), trioctylphosphine (TOP, 97%), oleylamine (70%), oleic acid (90%), 1-octanethiol (> 98.5%), lead acetate trihydrate (99.99 %), hexamethyldisilathiane, and triethylamine were obtained from Sigma Aldrich. Cadmium oxide (CdO, 99.998%), selenium powder (99.999%) and octadecylphosphonic acid (ODPA, 97%) were purchased from Alfa Aesar. Azido-dPEG®12-NHS ester and m-dPEG®12-NHS ester were purchased from Quanta BioDesign. Amicon®Ultra diafiltration filters (50K cutoff) were purchased from EMD Millipore.

Instrumentation

^{1}H NMR and ^{13}C NMR spectra were obtained on a Bruker DRX 400 NMR spectrometer. Absorption spectra of QDs were measured on an Agilent UV-Visible spectrophotometer. PL spectra of CdSe/CdS QDs, CdSe/CdS nanorods, and CdSe/ZnS QDs were taken on a FluoroMax3 spectrofluorometer (HORIBA), and PL spectra of PbS QDs, InAs/CdSe/ZnS were collected using a thinned InGaAs point detector (Thorlabs, DET10N) with a 532 nm laser excitation. Transmission electron microscopy (TEM) images of CdSe/CdS QDs were taken on a JEOL 2010 advanced high

performance TEM. Quantum yields were measured using an integrating sphere (Labsphere RTC-060-SF) under a diode laser excitation. A longpass filter was used to block the excitation, and signal from the sample was collected using a calibrated detector through a lock-in amplifying system.

Synthesis of CdSe QDs

CdSe cores were synthesized according to a literature method,[18] except that the reaction was scaled up with twice the amount of chemicals used. Briefly, CdO (120 mg), octadecylphosphonic acid (ODPA, 560 mg) and trioctylphosphine oxide (TOPO, 6 g) were added to a 100 mL flask. The mixture was heated to 150 °C and degassed under vacuum for 1 hour. Under nitrogen flow, the reaction mixture was heated to 330 °C to form a clear solution. After adding 3.0 mL of trioctylphosphine (TOP) to the solution, the temperature was brought up to 380 °C, at which point a Se/TOP (120 mg of Se in 1.0 mL of TOP) solution was swiftly injected into the flask. When the CdSe core nanocrystals reached the desired size, the reaction was terminated by removing the heating mantle. 10 mL of hexane was added to the resulting reaction solution to form a stock solution.

Synthesis of Cd-oleate

To a 250 mL three-neck round bottom flask, cadmium oxide (2.57 g, 0.02 mol) and oleic acid (40 mL) were added. Under stirring, the mixture was degassed under vacuum for 10 min at room temperature, 1 h at 80 °C, and 1 h at 120 °C. The temperature was then brought up to 160 °C under nitrogen atmosphere, and held at this temperature until the solution became clear. The reaction solution was allowed to cool down to 120 °C, and ODE was added to make the total volume 100

mL. The solution was degassed at 80 °C for one hour before being transferred into three 40 ml vials. The resulting 0.2 M Cd-oleate was stored at room temperature as a slightly yellow soft solid.

Syntheses of QD-norbornene

Syntheses of NB-nonanoic acid capped CdSe/CdS nanorods and InAs/CdSe/ZnS QDs are similar to that of CdSe/CdS QDs. NB-nonanoic acid was added after precursor infusion when the reaction solution cooled down to below 200 °C, followed by annealing at that temperature for 1 h.

PbS QDs were synthesized based on the method of Hines et al.[19] Briefly, 0.306 g of lead acetate was dissolved in 8 mL of 1-octadecene with oleic acid to have a final concentration of 0.1 M. Then the solution was degassed at 80 °C for at least two hours. In a glovebox, 105.5 µL of hexamethyldisilathiane was diluted in 5 mL of ODE and then quickly injected into the flask with the lead precursor at 60 °C. In our synthesis, oleic acid was partially (25%-75% in molar ratio) substituted by NB-nonanoic acid. The reation was quenched immediately using an ice bath. The resulting PbS QDs were precipitated out by adding acetone to the growth solution. The supernatant was discarded and the precipitate was rewashed with hexane and acetone. Finally, the NB-nonanoic acid capped PbS QDs were dispersed in chloroform and stored in an inert atmosphere.

Syntheses of Tetrazine-PEG-OMe and Tetrazine-PEG-N$_3$

5 mg of (4-(1,2,4,5-tetrazin-3-yl)phenyl) methanamine hydrochloride were dissolved in 500 µL of dichloromethane (DCM) with dropwise addition of about 50 µL of triethylamine. While stirring, azido-dPEG®12-NHS ester or m-dPEG®12-NHS ester solution (15 mg in 100 µL DCM) was added and the mixture was allowed to react at room temperature for 4 h. The resulting solution was purified using a silica column with a solution of 7% methanol in DCM as the flushing solvent. The eluted pink product was collected and stored at 4 °C.

Synthesis of QD-PEG-N₃

5 mg of QD-norbornene was dispersed in 100 μL of chloroform and added to a mixture of tetrazine-PEG-OMe and tetrazine-PEG-N$_3$ solution (4mg, dissolved in 200 μL of chloroform). The molar ratios of these two tetrazine ligands added to the reaction were 0:1, 0.25:0.75, 0.5:0.5 and 1:0 to make QD-N$_3$(100%), QD-N$_3$(75%), QD-N$_3$(50%), and QD-OMe, respectively. The reaction solution was stirred for 2 h at room temperature, followed by dropwise addition of hexanes until the solution became turbid. After centrifugation, the upper pink solution was discarded, and the precipitate was redispersed in 1× PBS. The resulting water-soluble QDs were washed five times using a 50kDa cutoff dialysis filter to remove excess free ligands. The QDs in PBS solution were purified using a 0.2 μm syringe filter and stored at 4 °C for further use.

2.9   Chapter Acknowledgement

References

1.   Pellegrino, T.; Manna, L.; Kudera, S.; Liedl, T.; Koktysh, D.; Rogach, A. L.; Keller, S.; Radler, J.; Natile, G.; Parak, W. J. Hydrophobic Nanocrystals Coated with an Amphiphilic Polymer Shell: A General Route to Water Soluble Nanocrystals *Nano Lett.* **2004,** *4,* 703-707.

2.   Han, H. S.; Devaraj, N. K.; Lee, J.; Hilderbrand, S. A.; Weissleder, R.; Bawendi, M. G. Development of a Bioorthogonal and Highly Efficient Conjugation Method for Quantum Dots Using Tetrazine-Norbornene Cycloaddition *J. Am. Chem. Soc.* **2010,** *132,* 7838-7839.

3.   Devaraj, N. K.; Weissleder, R.; Hilderbrand, S. A. Tetrazine-Based Cycloadditions: Application to Pretargeted Live Cell Imaging *Bioconjugate Chem.* **2008,** *19,* 2297-2299.

4.   Yu, W. W.; Peng, X. G. Formation of High-Quality Cds and Other Ii-Vi Semiconductor Nanocrystals in Noncoordinating Solvents: Tunable Reactivity of Monomers *Angew. Chem., Int. Ed.* **2002,** *41,* 2368-2371.

5.   Zarghami, M. H.; Liu, Y.; Gibbs, M.; Gebremichael, E.; Webster, C.; Law, M. P-Type Pbse and Pbs Quantum Dot Solids Prepared with Short-Chain Acids and Diacids *ACS Nano* **2010,** *4,* 2475-2485.

6.   Virieux, H.; Le Troedec, M.; Cros-Gagneux, A.; Ojo, W. S.; Delpech, F.; Nayral, C.; Martinez, H.; Chaudret, B. Inp/Zns Nanocrystals: Coupling Nmr and Xps for Fine Surface and Interface Description *J. Am. Chem. Soc.* **2012,** *134,* 19701-19708.

7.   Cordero, J. Synthesis of Derivatizable Semiconductor Nanocrystals through Rational Ligand Design, and Applications Thereof. Ph.D. Thesis, Massachusetts Institute of Technology, 2016.

8.   Chen, O.; Zhao, J.; Chauhan, V. P.; Cui, J.; Wong, C.; Harris, D. K.; Wei, H.; Han, H. S.; Fukumura, D.; Jain, R. K., *et al*. Compact High-Quality Cdse-Cds Core-Shell Nanocrystals with Narrow Emission Linewidths and Suppressed Blinking *Nat. Mater*. **2013,** *12*, 445-451.

9.   Hens, Z.; Martins, J. C. A Solution Nmr Toolbox for Characterizing the Surface Chemistry of Colloidal Nanocrystals *Chem. Mater*. **2013,** *25*, 1211-1221.

10.   De Roo, J.; Van den Broeck, F.; De Keukeleere, K.; Martins, J. C.; Van Driessche, I.; Hens, Z. Unravelling the Surface Chemistry of Metal Oxide Nanocrystals, the Role of Acids and Bases *J. Am. Chem. Soc*. **2014,** *136*, 9650-9657.

11.   Fritzinger, B.; Capek, R. K.; Lambert, K.; Martins, J. C.; Hens, Z. Utilizing Self-Exchange to Address the Binding of Carboxylic Acid Ligands to Cdse Quantum Dots *J. Am. Chem. Soc*. **2010,** *132*, 10195-10201.

12.   Zhan, N. Q.; Palui, G.; Mattoussi, H. Preparation of Compact Biocompatible Quantum Dots Using Multicoordinating Molecular-Scale Ligands Based on a Zwitterionic Hydrophilic Motif and Lipoic Acid Anchors *Nat. Protoc*. **2015,** *10*, 859-874.

13.   Smith, A. M.; Nie, S. Minimizing the Hydrodynamic Size of Quantum Dots with Multifunctional Multidentate Polymer Ligands *J. Am. Chem. Soc*. **2008,** *130*, 11278-11279.

14.   Gerion, D.; Pinaud, F.; Williams, S. C.; Parak, W. J.; Zanchet, D.; Weiss, S.; Alivisatos, A. P. Synthesis and Properties of Biocompatible Water-Soluble Silica-Coated Cdse/Zns Semiconductor Quantum Dots *J. Phys. Chem. B* **2001,** *105*, 8861-8871.

15.   Zhang, X.; Shamirian, A.; Jawaid, A. M.; Tyrakowski, C. M.; Page, L. E.; Das, A.; Chen, O.; Isovic, A.; Hassan, A.; Snee, P. T. Monolayer Silane-Coated, Water-Soluble Quantum Dots *Small* **2015,** *11*, 6091-6096.

16.   Bruns, O. T.; Bischof, T. S.; Harris, D. K.; Franke, D. K.; Shi, Y.; Riedemann, L.; Bartelt, A.; Jaworski, F. B.; Carr, J. A.; Rowlands, C. J., *et al*. Next-Generation in Vivo Optical Imaging with Short-Wave Infrared Quantum Dots *Nat. Biomed. Eng.* **2017,** *1*, 0056.

17.   Franke, D.; Harris, D. K.; Chen, O.; Bruns, O. T.; Carr, J. A.; Wilson, M. W. B.; Bawendi, M. G. Continuous Injection Synthesis of Indium Arsenide Quantum Dots Emissive in the Short-Wavelength Infrared *Nat. Commun.* **2016,** *7*, 12749.

18.   Carbone, L.; Nobile, C.; De Giorgi, M.; Sala, F. D.; Morello, G.; Pompa, P.; Hytch, M.; Snoeck, E.; Fiore, A.; Franchini, I. R., *et al*. Synthesis and Micrometer-Scale Assembly of Colloidal Cdse/Cds Nanorods Prepared by a Seeded Growth Approach *Nano Lett.* **2007,** *7*, 2942-2950.

19.   Hines, M. A.; Scholes, G. D. Colloidal Pbs Nanocrystals with Size-Tunable near-Infrared Emission: Observation of Post-Synthesis Self-Narrowing of the Particle Size Distribution *Adv. Mater.* **2003,** *15*, 1844-1849.

Chapter 3

Live Cell Labeling with QD Probes

3.1 Chapter Overview
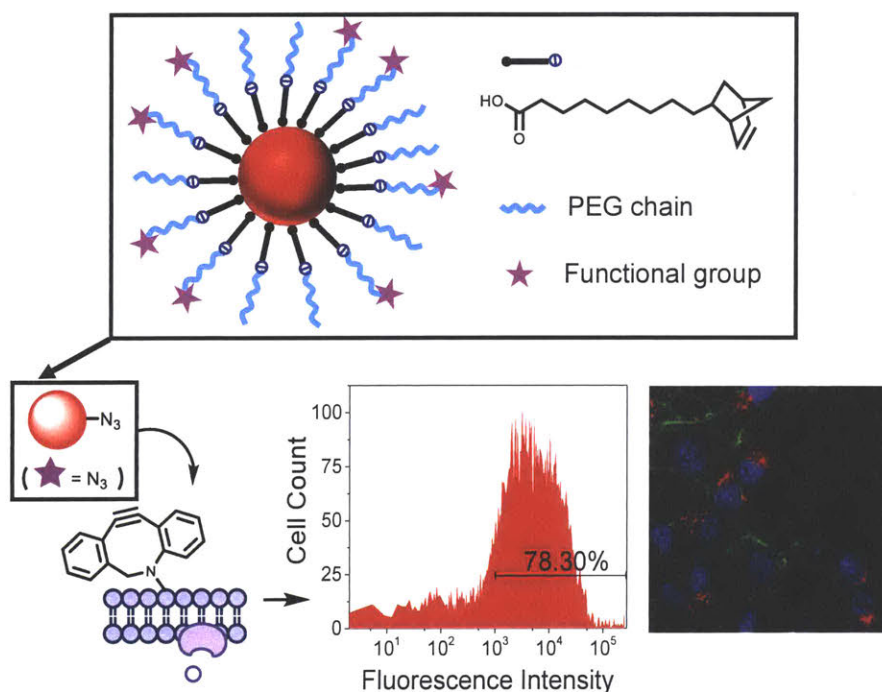
Figure 3-1. Water-soluble QDs prepared using our newly developed ligand system are used to target metabolically labeled cancer cells, and high specific targeting efficiency was achieved.

As mentioned in the previous chapter, we successfully transferred the as-synthesized hydrophobic QDs into water using our new NB-nonanoic ligand system *via* a norbornene/tetrazine click reaction, and versatile functionalization of the water-soluble QDs can be readily realized by incorporating functional groups (azide, maleimide, biotin, etc.) at the terminus of the PEG chain (Figure 3-1). The resulting water-soluble QDs have a high QY, a compact hydrodynamic diameter (HD) of ~12 nm, and excellent colloidal stability, enabling their use as fluorescent probes for

biological applications. In this chapter, we investigated whether these water-soluble QDs prepared using our new ligand system are suitable for cellular imaging. More specifically, we studied the non-specific cellular binding and active cellular targeting using our water-soluble QDs.

In this work, we demonstrated the simplicity and effectiveness of our approach by incubating azido-functionalized CdSe/CdS QDs (QD-N$_3$) with mouse 4T1 breast cancer cells that were metabolically labeled with a dibenzocyclooctyne (DBCO) bearing unnatural sugar (Figure 3-1). Both flow cytometry analysis and confocal imaging showed improved cellular uptake of QD-N$_3$ mediated by the highly efficient DBCO/N$_3$ click chemistry. While for the control cells without pre-treatment with the DBCO-bearing sugar, little QD fluorescence was observed, indicating minimal non-specific cellular binding.

3.2 Cell Labeling Using CdSe/CdS QDs
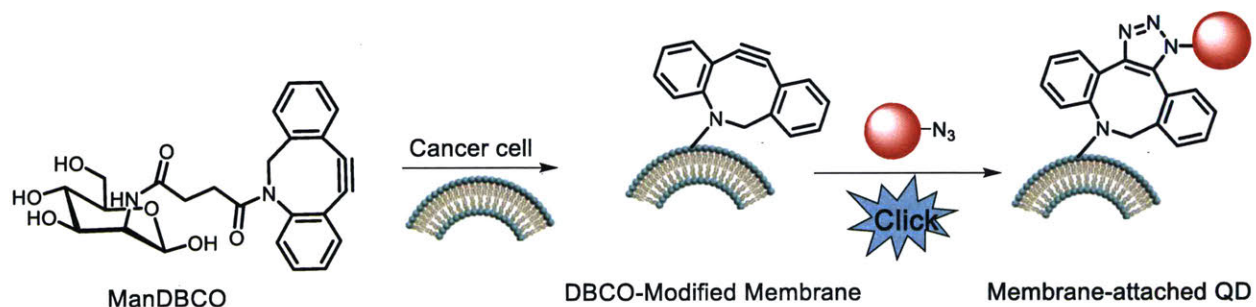
Scheme 3-1. Schematic illustration of using the azido-functionalized QDs to label cells. The cells are pretreated with ManDBCO, which ends up being expressed on cell membranes through cellular metabolic glycosylation pathways.

In addition to studying endocytosis-mediated cellular uptake, we also studied the targeted uptake of QD-N$_3$ into chemically labeled cells *via* efficient click chemistry. Metabolic labeling of cells using unnatural sugars has proven to be an effecitve methodology to introduce artificial chemical receptors to cell surface, as an alternative to endogenous protein receptors that have shown

66

limitations for cell targeting.[1-3] Here we explored targeting cancer cells with DBCO groups on the cell surface using QD-N$_3$ probes. Wang *et al.* recently reported a DBCO-bearing unnatural sugar, Ac$_4$ManDBCO, that metabolically labels LS174T colon cancer cells with DBCO groups for subsequent targeting of azido-modified nanomedicines.[4-5] To label cells with QD-N$_3$, we adapted this procedure by using a new unnatural sugar, ManDBCO, a water-soluble de-acetylated analog of Ac$_4$ManDBCO, for metabolic labeling of 4T1 breast cancer cells. We hypothesized that ManDBCO would participate in the cellular glycosylation pathways and end up being expressed on the cell surface in the form of glycoproteins, functioning as artificial receptors, and that these receptors would improve cellular uptake of QD-N$_3$ *via* a catalyst-free and bio-orthogonal DBCO/N$_3$ click reaction (Scheme 3-1).[6-7]

3.2.1 Synthesis of ManDBCO

D-Mannosamine hydrochloride (0.1 mmol) and triethylamine (0.1 mmol) were dissolved in methanol, followed by the addition of DBCO-NHS (0.12 mmol). The reaction mixture was stirred at room temperature for 48 h. The solvent was removed, and the crude product was purified *via* preparative HPLC using acetonitrile and water as the mobile phases. ^{1}H NMR spectrum and mass spectrum of the final product was obtained to confirm the structure of ManDBCO (Figure 3-2).

^{1}H NMR (500 MHz, DMSO-d_6) δ (ppm): 7.71-7.22 (m, 8H, Ph), 7.06 (t, J = 10.3 Hz, 0.5H, N*H*C(O)), 6.38 (ddd, J = 14.8, 4.4, 1.5 Hz, 1H,CHOC*H*), 6.31 (td, J = 7.3, 1.5 Hz, 0.5H, N*H*C(O)), 5.04 (d, J = 14.0 Hz, 2H, C(O)NC*H$_2$*), 4.71 (td, J = 5.8, 1.5 Hz, 1H, NHCHC*H*CH), 4.68&4.60&4.06 (m, 1H, OH), 4.56&4.52 (dd, J = 5.4, 1.5 Hz, 1H, NHCHCHC*H*), 4.33-4.23 (m, 1H, NHC*H*CHCH), 3.88&3.68 (m, 1H, CH$_2$C*H*OCH), 3.63 (m, 1H, OH), 3.60 (m, 1H, OH),

3.51&3.46 (m, 2H, CH_2CHOCH), 3.16&3.02 (m, 1H, OH), 2.57&2.34 (m, 2H, C(O)CH$_2$CH_2C(O)N), 2.07&1.77 (m, 2H, C(O)CH_2CH$_2$C(O)N).

MS: 467.2 m/z corresponds to [M+H]$^+$, and 955.4 m/z corresponds to [2M+Na]$^+$.
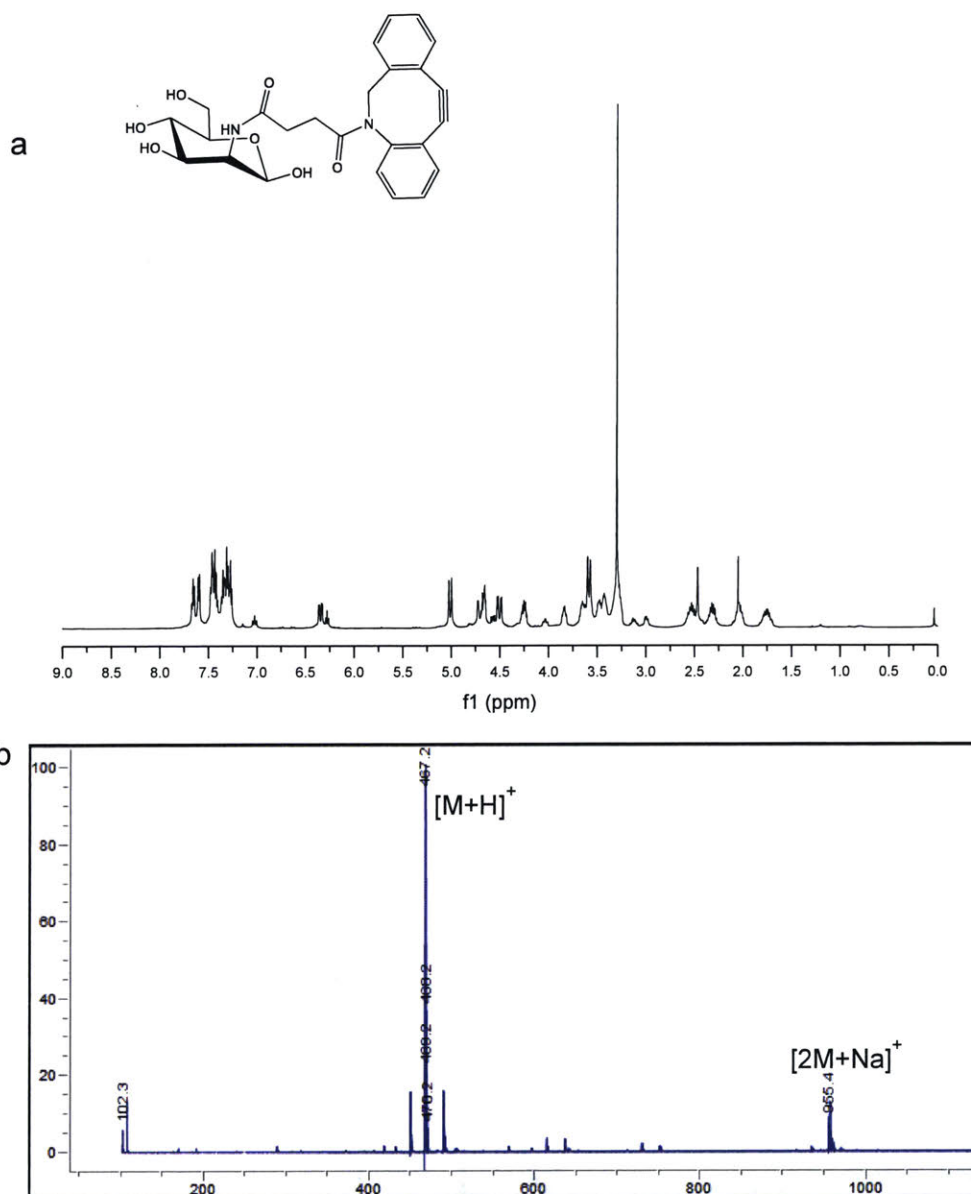
Figure 3-2. (a) Chemical structure and ^{1}H NMR spectrum of ManDBCO. (b) Mass spectrum of ManDBCO.

3.2.2 4T1 Cell Labeling Using QD-N$_3$

We investigated whether 4T1 cells treated with ManDBCO express DBCO groups on the cell membranes and can mediate the specific binding of QD-N$_3$ *via* a click reaction. 4T1 cells were treated with ManDBCO for three days, followed by incubation with QD-N$_3$ (50% N$_3$, Emission: 625 nm) for 2 h. After incubation, the cells were washed multiple times to remove free QD-N$_3$ prior to confocal microscopy and flow cytometry analyses. As shown in Figure 3-3a, QD-N$_3$ shows significantly enhanced cellular uptake in 4T1 cells pretreated with ManDBCO compared to control cells without ManDBCO treatment. We note that the passive cellular uptake of QDs is very low even after 4 h of incubation (Figure 3-3b), perhaps due to the slightly net negative charge of the QD probe (Figure 3-4).[8] The covalently conjugated QD-N$_3$ eventually enters endosomes/lysosomes, as evidenced by confocal images (Figure 3-3 a-b). Increasing the incubation time from 2 h to 4 h increases the cellular uptake of QD-N$_3$ from 29% to 46% (Figure 3-3c), indicating a continuous click reaction-mediated cellular uptake over time. After 4 h of incubation, negligible change of fluorescence intensity in control cells without ManDBCO treatment was observed (Figure 3-3 d-e), further highlighting the minimal nonspecific cellular uptake of QD-N$_3$. In contrast, cells pretreated with ManDBCO exhibit an obvious increase in fluorescence intensity overall (Figure 3-3f). To exclude the impact of cell-surface DBCO on the permeability of cells, we incubated ManDBCO-pretreated 4T1 cells with QD-OMe under the same conditions, which shows minimal cellular internalization (Figure 3-3g). More confocal images and representative flow cytometry profiles are available in Appendix. These experiments demonstrate that ManDBCO can metabolically label 4T1 cells with DBCO groups, and this leads to cellular internalization of QD-N$_3$ *via* a click reaction.
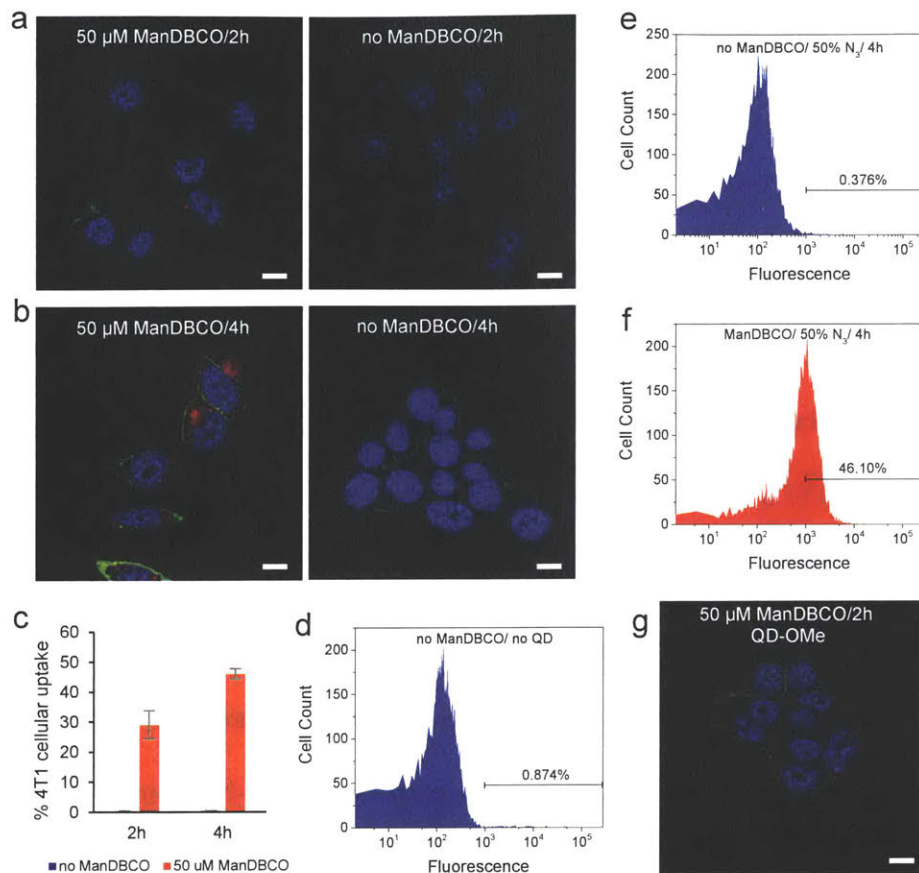
Figure 3-3. Confocal images of 4T1 cells treated and not treated with 50 μM ManDBCO sugar after incubation with QD-N$_3$(50%) for (a) 2 h and (b) 4 h. (c) Percent cellular uptake of QD-N$_3$(50%) by 4T1 cells with (orange) or without (blue) pre-treatment of 50 μM ManDBCO. (d-f) Representative flow cytometry profiles of 4T1 cells after incubation with QD-N$_3$(50%). The PE-Texas Red channel was used. Cell treatment condition and incubation time information is provided at the top of each figure. (g) Confocal images of 4T1 cells pretreated with 50 μM ManDBCO and incubated with QD-OMe for 2 h. (Color code for all confocal images: blue: DAPI, green: Alexa Fluoro 488 membrane stain, red: QD, scale bar: 10 μm.)
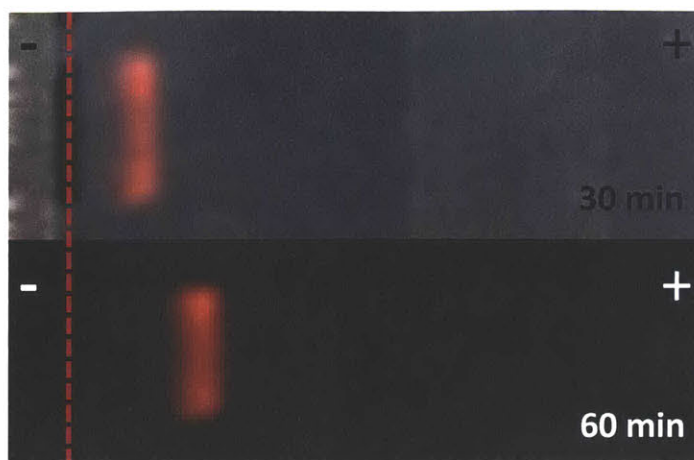
Figure 3-4. Gel electrophoresis images of water soluble CdSe/CdS QDs. Upper image was taken at 30 min, and lower image was taken at 60 min under UV light (0.8% agarose gel, 60 V electric field). The red gradient line indicates gel well line.

3.2.3 Cell Labeling with Higher N₃ Density on QD Surfaces

Given that the click reaction between N_3 and cell-surface DBCO groups mediates the cellular uptake of QD-N_3, we further studied whether a higher density of N_3 on the surfaces of QDs would provide better cell targeting efficiency. QD-N_3 with different molar percentages of tetrazine-PEG-N_3 (50%, 75%, and 100%) were prepared, and all of them showed excellent water solubility. 4T1 cells were treated with ManDBCO for three days, followed by incubation with QD-N_3(50%), QD-N_3(75%), and QD-N_3(100%), respectively, for 2 h. Cells without ManDBCO treatment were used as control. Confocal images show significantly improved cellular internalization of QD-N_3(100%) compared with QD-N_3(50%), while the control cells exhibit similar minimal QD fluorescence (Figure 3-5). All formulations show little passive uptake by 4T1 cells (Figure 3-5d, Appendix

Figures), further highlighting the minimal nonspecific binding of these QD-N₃. More confocal images and representative flow cytometry profiles are available in Appendix.
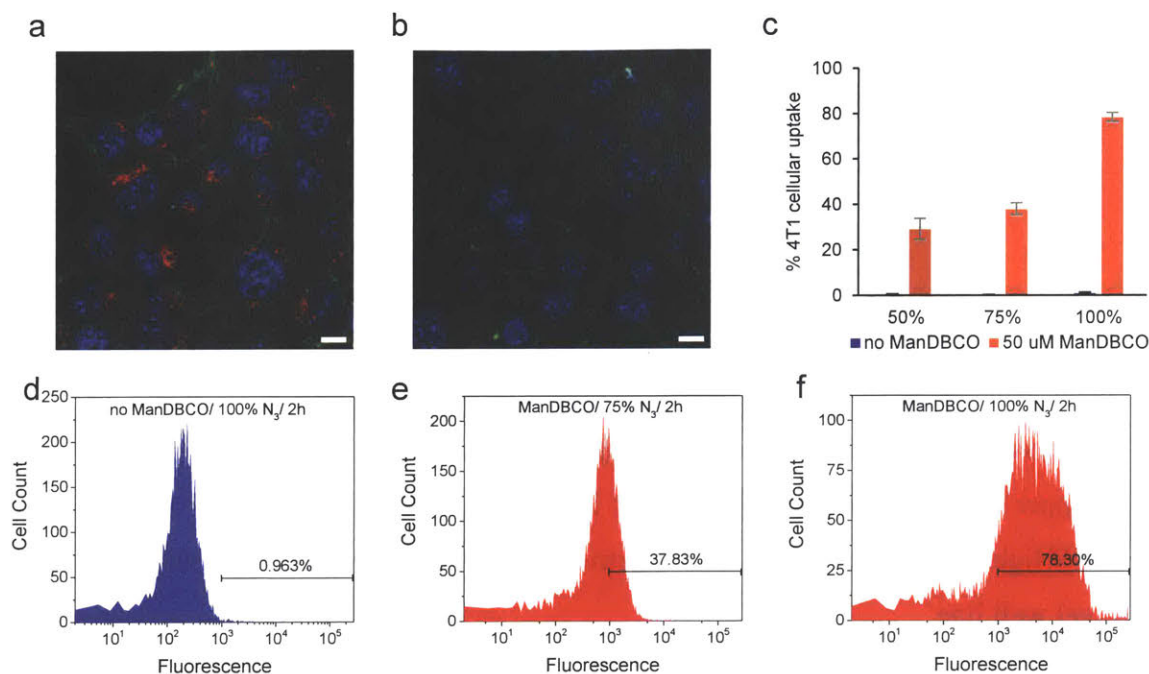
Figure 3-5. Confocal images of 4T1 cells (a) treated with 50 μM ManDBCO, and (b) not treated with ManDBCO and incubated with QD-N$_3$(100%) for 2 h (blue: DAPI, green: Alexa Fluoro 488 membrane stain, red: QD, scale bar: 10 μm). (c) Percent cellular uptake of QD-N$_3$(50%), QD-N$_3$(75%), and QD-N$_3$(100%) after 2 h incubation with 4T1 cells that were pretreated with 50 uM ManDBCO (orange) or PBS (blue). (d-f) Representative flow cytometry profiles of 4T1 cells after incubation with QD-N$_3$. The PE-Texas Red channel was used. Cell treatment condition and incubation time information is provided at the top of each figure.

3.3 QD-oligo Probes

We further demonstrated that azido or maleimide functionalized QDs (QD-N$_3$, QD-Mal) can be conjugated with DNA oligos or antibodies for more specific targeting applications. Single-strand DNA or RNA oligos conjugated with fluorophores are usually designed as probes for targeting
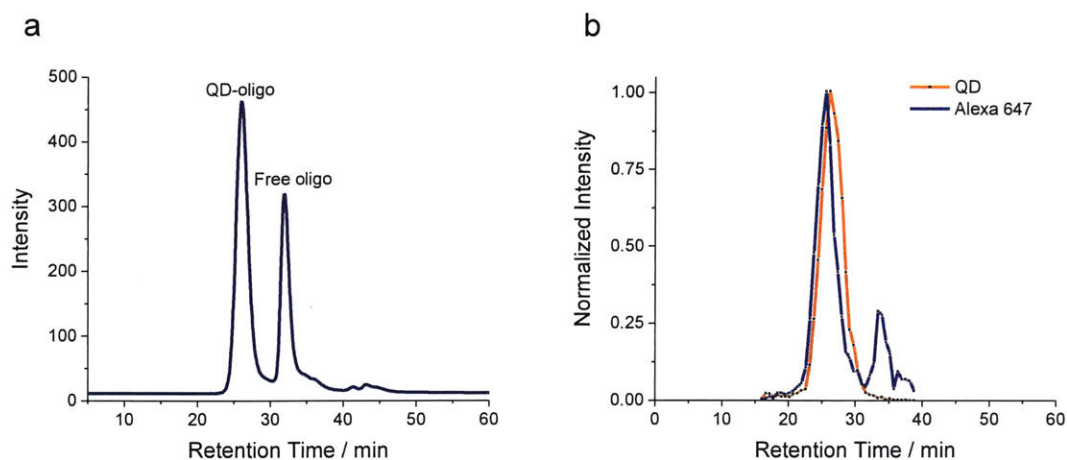
Figure 3-6. (a) GFC trace of QD-N$_3$ and DBCO-oligo conjugation reaction solution. (b) PL intensities of QD (orange) and Alexa 647 (blue) of GFC fractions of QD-oligo and Alexa647-oligo hybridization mixture.

chromosomes and RNAs by hybridizing with complimentary sequences.[9-11] As we discussed in Chapter 1, QD probes are promising alternative fluorophores to organic dyes for highly multiplexed transcriptome imaging.[12-15] Thus, we conjugated a single strand 32-mer DNA oligo to QD-N$_3$ (Emission: 610 nm) to make a QD-oligo fluorescent probe for gene sequence targeting. QD-N$_3$ was reacted with DBCO-oligo and purified using gel filtration chromatography (GFC). As shown in Figure 3-6a, the retention time of the first peak (assigned to QD-oligo) is 26 min, which corresponds to a HD of 15 nm according to our column calibration curve (Figure 3-7), indicating successful conjugation of oligos to QDs. We then tested the hybridization efficiency of QD-oligo probes to a complimentary oligo sequence that is terminated with an Alexa 647 dye molecule. The reaction mixture was analyzed using GFC, and fractions were collected and the PL intensity of QDs and Alexa 647 of each fraction was read on a plate reader. Figure 3-6b shows a strong overlap of the QD signal (Exitation: 450 nm, Detection: 600 nm) and Alexa 647 signal (Exitation:630 nm, Detection: 670 nm), indicating that the Alexa 647-oligo successfully hybridized with the complimentary QD-oligo. The smaller peak at about 33 min corresponds to free Alexa 647-oligo,

73

which from the peak area was calculated to be 19% of all Alexa 647-oligo added (Figure 3-6b). We have thus successfully demonstrated secondary functionalization of these water soluble QDs with DNA oligos for further targeting with high efficiency.
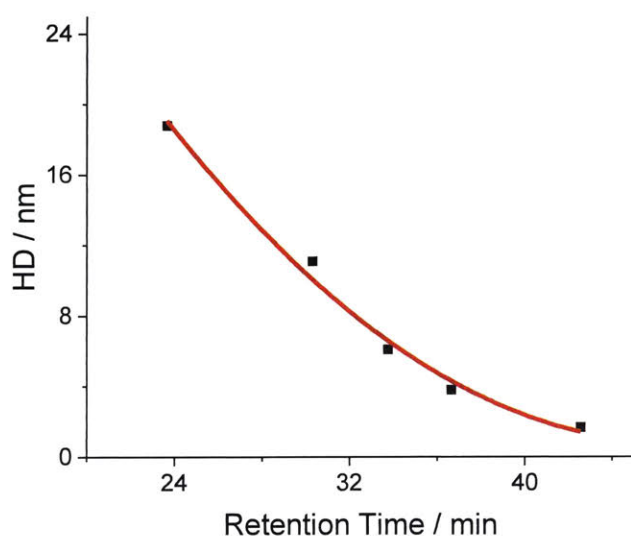
Figure 3-7. A superose 6 size-exclusion column was calibrated with protein standards containing thyroglobulin, bovine γ-globulin, chicken ovalbumin, equine myoglobin, and vitamin B12 from Bio-Rad (black squares). The red curve is a calibration curve of hydrodynamic diameter versus retention time based on the protein standards.

3.4 Summary

We report a new, versatile ligand system that yields "clickable" QDs of various formulations at the hundred nmol scale. The ligand is characterized with a carboxylic acid group at one end for binding to metal sites on QD surfaces and a norbornene group at the other for flexible functionalization. Upon attaching a tetrazine-PEG molecule using click chemistry, we were able to produce water soluble QDs with a high QY, a compact HD, and high colloidal stability. Furthermore, we demonstrated the efficacy and versatility of this ligand system by using azido functionalized CdSe/CdS QDs to label ManDBCO-treated 4T1 cancer cells, and to conjugate QDs

with single strand DNA oligos for further targeting. Our results demonstrate that this ligand system can generate high-quality water-soluble and clickable QDs in quantity for biological applications.

3.5 Experimental details

Materials

(4-(1,2,4,5-tetrazin-3-yl)phenyl) methanamine hydrochloride (95%), trimethylamine (>99%), D-Mannosamine hydrochloride, dibenzocycloocyne-NHS ester (DBCO-NHS), and dibenzocyclooctyne-PEG$_4$-NHS ester (95%) were obtained from Sigma Aldrich. Illustra NAP-5 columns were obtained from GE Healthcare Life Sciences. DNA oligos were ordered from IDT.

Instrumentation

^{1}H NMR was obtained on a Bruker DRX 400 NMR spectrometer. Liquid chromatography-mass spectrometry (LC-MS) analyses were conducted on the Agilent 1290 Infinity LC System equipped with an Agilent 6140 Quadruple mass spectrometer, using acetonitrile and water containing 0.1% formic acid as the mobile phases at a rate of 0.6 mL/min. Confocal images were taken using a ZEISS LSM 710 NLO system. Cell flow cytometry analysis was carried out on a BD LSR II system. PE Texas Red channel (610 ± 10 nm) was chosen to detect the QD signal. The gel filtration chromatography (GFC) setup was an AKTAprime Plus system equipped with a Superose 6 10/300 GL column. The mobile phase was 1x PBS, and measurements were carried out at a flow rate of 0.5 mL/min. 250 μL of each sample was injected, and absorbance at 280 nm was recorded. GFC fractions of QD-oligo hybridization mixture were read on a BioTek Synergy 4 Microplate Reader.

Synthesis of QD-PEG-N₃

5 mg of QD-norbornene was dispersed in 100 µL of chloroform and added to a mixture of tetrazine-PEG-OMe and tetrazine-PEG-N₃ solution (4 mg, dissolved in 200 µL of chloroform). The molar ratios of these two tetrazine ligands added to the reaction were 0:1, 0.25:0.75, 0.5:0.5 and 1:0 to make QD-N₃(100%), QD-N₃(75%), QD-N₃(50%), and QD-OMe, respectively. The reaction solution was stirred for 2 h at room temperature, followed by dropwise addition of hexanes until the solution became turbid. After centrifugation, the upper pink solution was discarded, and the precipitate was redispersed in 1× PBS. The resulting water-soluble QDs were washed five times using a 50kDa cutoff dialysis filter to remove excess free ligands. The QDs in PBS solution were purified using a 0.2 µm syringe filter and stored at 4 °C for further use.

Conjugation with DNA Oligo and Hybridization with Alexa647-oligo

DBCO-oligo was synthesized by reacting DBCO-PEG₄-NHS ester with a single strand DNA oligo (5'-/5AmMC6/ACA CCC TTG CAC GTC GTG GAC CTC CTG CGC TA-3'), followed by purification using a NAP-5 column. About 0.1 nmol of QD-N₃ and 5 nmol of DBCO-oligo were mixed in 1 mL of PBS and stirred at room temperature for 4 h. The reaction solution was purified by GFC, and the QD-oligo solution was collected.

The above QD-oligo solution was mixed with 0.1 nmol Alexa647-oligo (5'-/5Alex647N/TAG CGC AGG AGG TCC ACG ACG TGC AAG GGT GT-3') in 300 µL of PBS. The resulting solution was stirred at room temperature overnight, followed by analysis using GFC. The fractions collected by GFC were read on a plate reader for PL signals of QD (Exitation: 450 nm, Detection: 600 nm) and Alexa 647 (Exitation: 630 nm, Detection: 670 nm), respectively.

In vitro cell labeling for flow cytometry assay

4T1 breast cancer cells were seeded into a 24-well plate at a cell density of 1×10^4 per well and allowed to attach for 12 h. ManDBCO (50 μM) was added and the cells were incubated at 37 °C for 72 h. After washing with PBS, cells were incubated with QD-N$_3$ (1 mg/mL, 10 μL) or QD-OMe (1 mg/mL, 10 μL) for 2 h and 4 h, respectively. Cells were collected with a cell scraper and analyzed by flow cytometry.

In vitro cell labeling for confocal imaging

4T1 Cells were seeded onto coverslips in a 6-well plate at a density of 4×10^4 cells per well and allowed to attach for 12 h. ManDBCO (50 μM) was added and the cells were incubated at 37 °C for 72 h. After washing with PBS, cells were incubated with QD-N$_3$ (1 mg/mL, 10 μL) or QD-OMe (1 mg/mL, 10 μL) for 2 h and 4 h. Cells were fixed with 4% paraformaldehyde (PFA) solution, followed by staining of cell nuclei and membrane with DAPI (2 μg/mL) and CellMask membrane stain (1 μg/mL), respectively. The coverslips were mounted onto microscope slides and imaged under a confocal laser scanning microscope.

DAPI	Alexa 488 membrane stain	QD	Merged
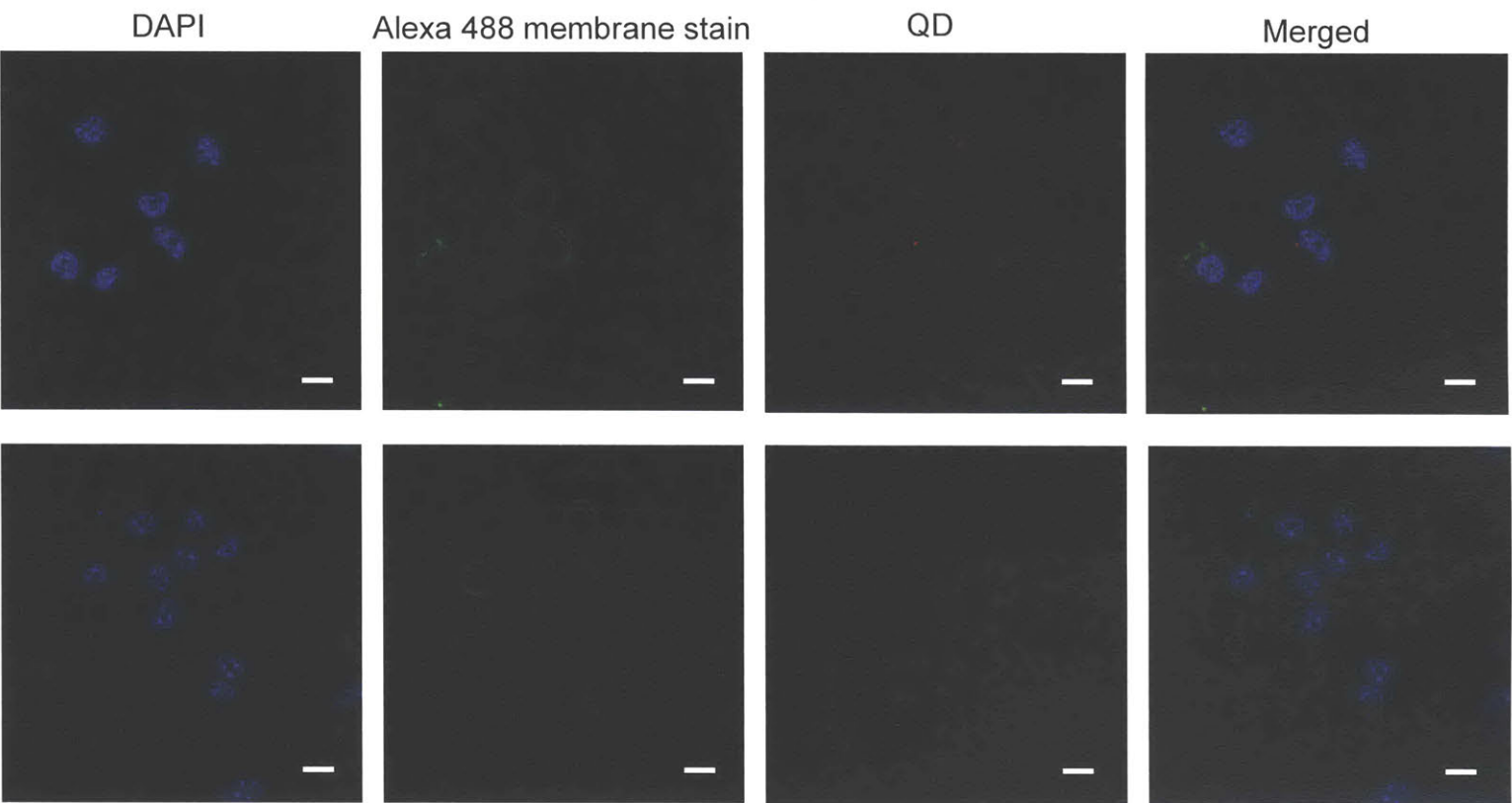
Figure 3-8. Confocal images of 4T1 cells treated (upper row) and not treated (lower row) with 50 μM ManDBCO after incubation with QD-N$_3$ (50%) for 2h (blue: DAPI; green: Alexa Fluoro 488 membrane stain; red: QD, scale bar: 10 μm).

DAPI	Alexa 488 membrane stain	QD	Merged
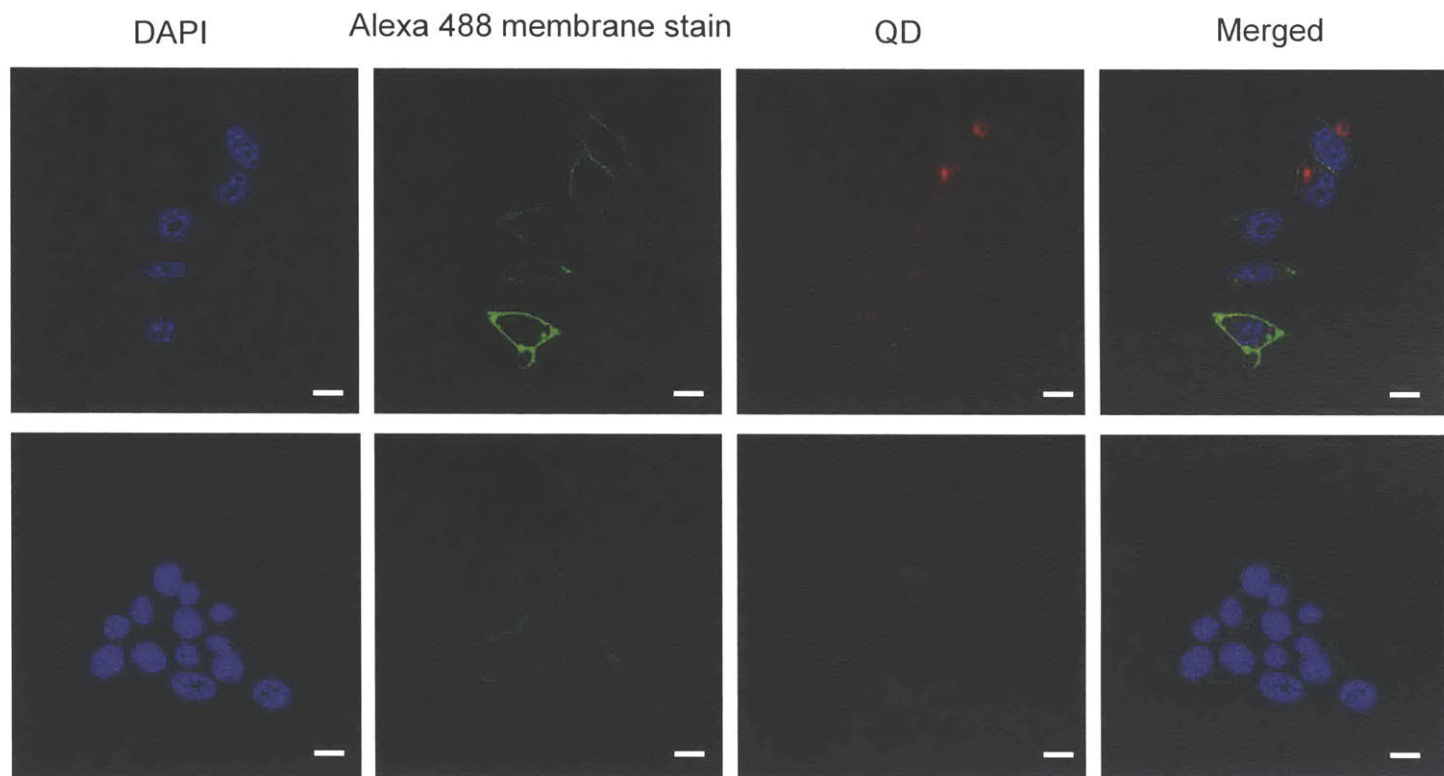
Figure 3-9. Confocal images of 4T1 cells treated (upper row) and not treated (lower row) with 50 μM ManDBCO after incubation with QD-N$_3$ (50%) for 4h (blue: DAPI; green: Alexa Fluoro 488 membrane stain; red: QD, scale bar: 10 μm).

| DAPI | Alexa 488 membrane stain | QD | Merged |
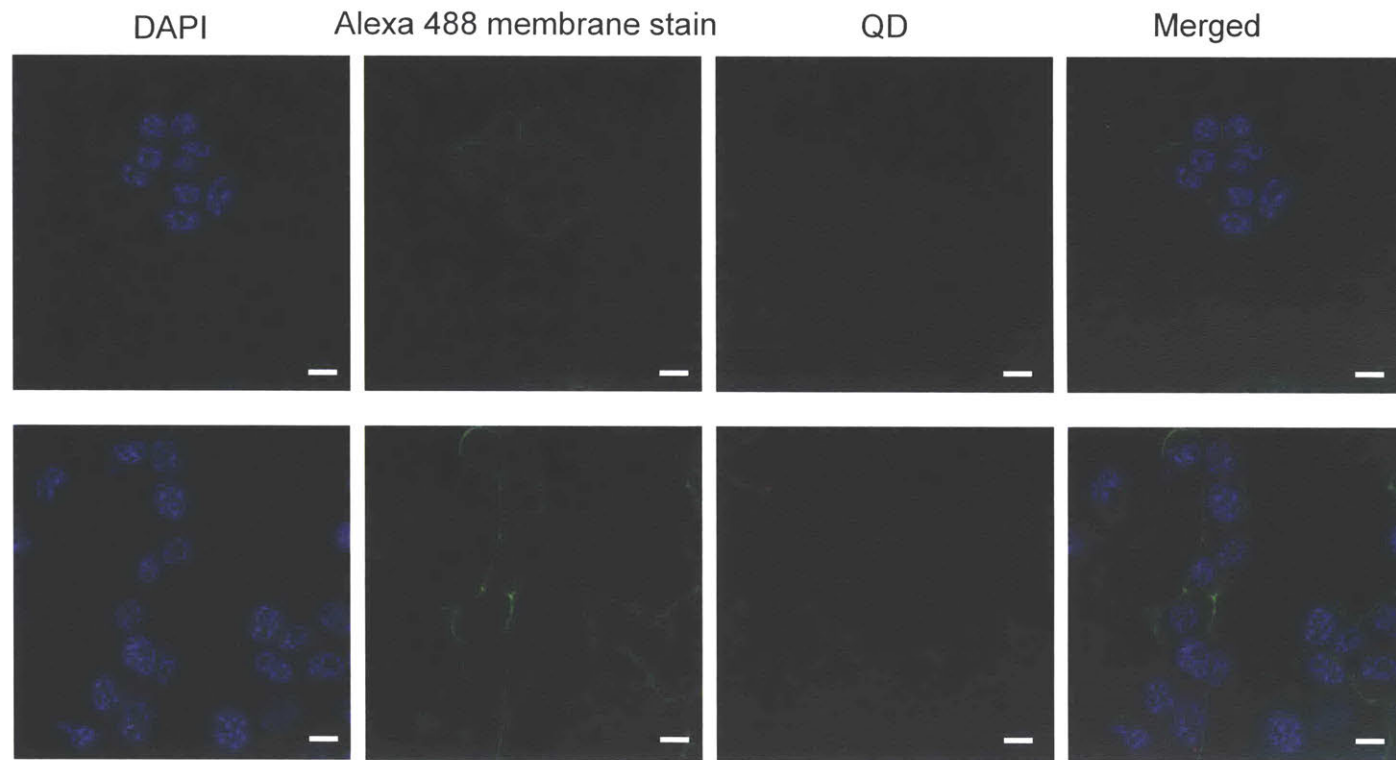
Figure 3-10. Confocal images of 4T1 cells treated with 50 µM ManDBCO after incubation with QD-OMe for 2h (blue: DAPI; green: Alexa Fluoro 488 membrane stain; red: QD, scale bar: 10 µm).

DAPI	Alexa 488 membrane stain	QD	Merged
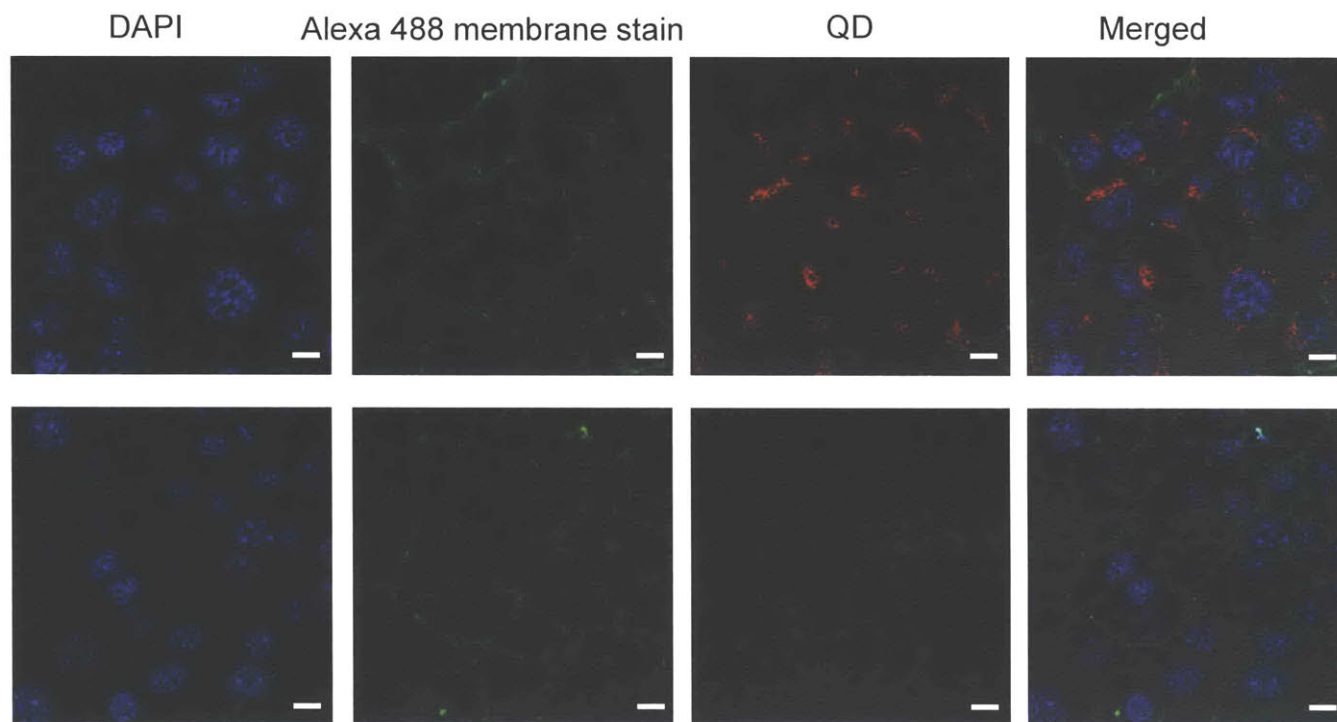
Figure 3-11. Confocal images of 4T1 cells treated (upper row) and not treated (lower row) with 50 μM ManDBCO after incubation with QD-N$_3$ (100%) for 2h (blue: DAPI; green: Alexa Fluoro 488 membrane stain; red: QD, scale bar: 10 μm).
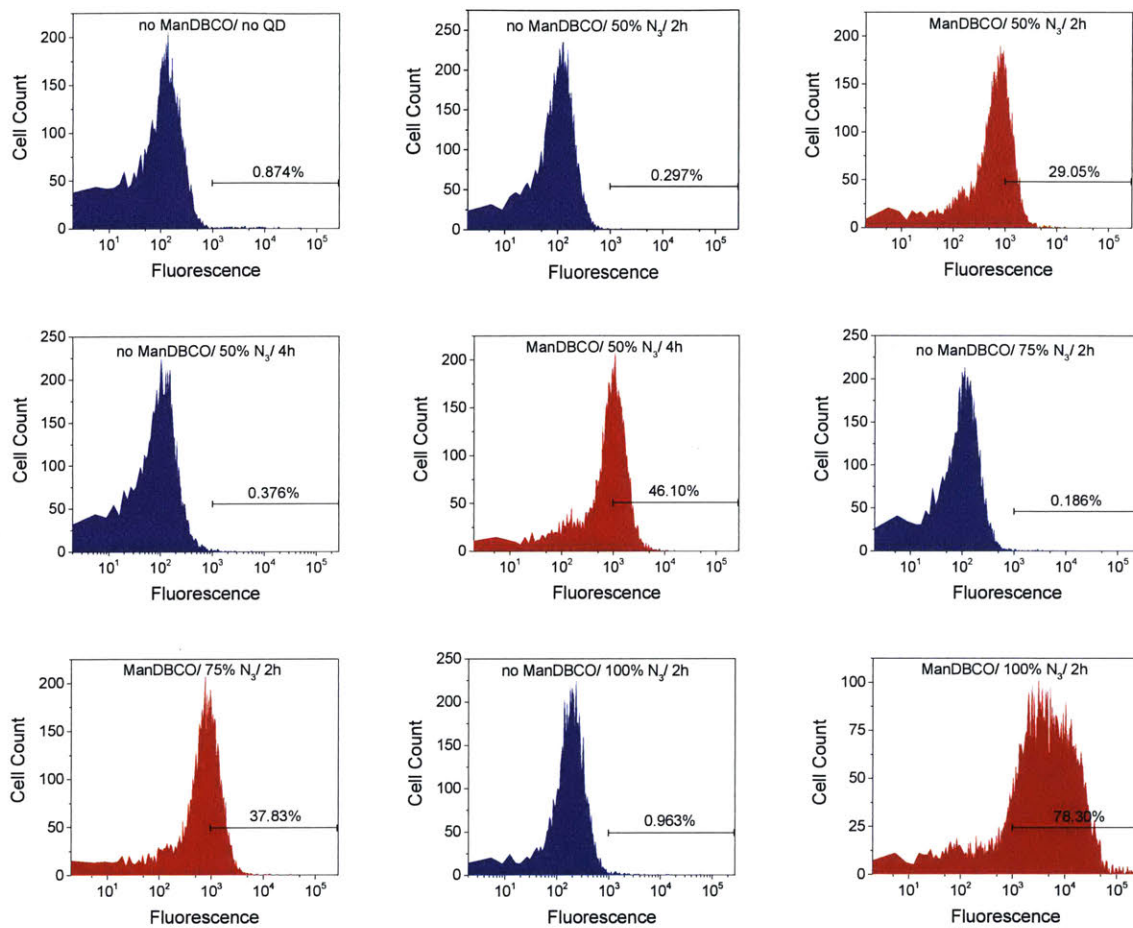
Figure 3-12. Representative flow cytometry profiles of 4T1 cells after incubation with QD-N₃ or QD-OMe. The PE-Texas Red channel was used. Cell treatment condition and incubation time information is provided at the top of each figure.

3.7 Chapter-specific Acknowledgement

References

1.   Prescher, J. A.; Dube, D. H.; Bertozzi, C. R. Chemical Remodelling of Cell Surfaces in Living Animals *Nature* **2004**, *430*, 873-877.

2.   Laughlin, S. T.; Bertozzi, C. R. Metabolic Labeling of Glycans with Azido Sugars and Subsequent Glycan-Profiling and Visualization Via Staudinger Ligation *Nat. Protoc.* **2007**, *2*, 2930-2944.

3.   Breidenbach, M. A.; Gallagher, J. E. G.; King, D. S.; Smart, B. P.; Wu, P.; Bertozzi, C. R. Targeted Metabolic Labeling of Yeast N-Glycans with Unnatural Sugars *Proc. Natl. Acad. Sci. U.S.A.* **2010**, *107*, 3988-3993.

4.   Wang, H.; Tang, L.; Liu, Y.; Dobrucka, I. T.; Dobrucki, L. W.; Yin, L. C.; Cheng, J. J. In Vivo Targeting of Metabolically Labeled Cancers with Ultra-Small Silica Nanoconjugates *Theranostics* **2016**, *6*, 1467-1476.

5.   Wang, H.; Wang, R. B.; Cai, K. M.; He, H.; Liu, Y.; Yen, J.; Wang, Z. Y.; Xu, M.; Sun, Y. W.; Zhou, X., *et al.* Selective in Vivo Metabolic Cell-Labeling-Mediated Cancer Targeting *Nat. Chem. Biol.* **2017**, *13*, 415-424.

6.   Jewett, J. C.; Sletten, E. M.; Bertozzi, C. R. Rapid Cu-Free Click Chemistry with Readily Synthesized Biarylazacyclooctynones *J. Am. Chem. Soc.* **2010**, *132*, 3688-+.

7.   Jeon, J.; Kang, J. A.; Shim, H. E.; Nam, Y. R.; Yoon, S.; Kim, H. R.; Lee, D. E.; Park, S. H. Efficient Method for Iodine Radioisotope Labeling of Cyclooctyne-Containing Molecules Using Strain-Promoted Copper-Free Click Reaction *Biorg. Med. Chem.* **2015,** *23,* 3303-3308.

8.   Arvizo, R. R.; Miranda, O. R.; Thompson, M. A.; Pabelick, C. M.; Bhattacharya, R.; Robertson, J. D.; Rotello, V. M.; Prakash, Y. S.; Mukherjee, P. Effect of Nanoparticle Surface Charge at the Plasma Membrane and Beyond *Nano Lett.* **2010,** *10,* 2543-2548.

9.   Beliveau, B. J.; Joyce, E. F.; Apostolopoulos, N.; Yilmaz, F.; Fonseka, C. Y.; McCole, R. B.; Chang, Y. M.; Li, J. B.; Senaratne, T. N.; Williams, B. R.*, et al.* Versatile Design and Synthesis Platform for Visualizing Genomes with Oligopaint Fish Probes *Proc. Natl. Acad. Sci. U.S.A.* **2012,** *109,* 21301-21306.

10.   Mali, P.; Aach, J.; Lee, J. H.; Levner, D.; Nip, L.; Church, G. M. Barcoding Cells Using Cell-Surface Programmable DNA-Binding Domains *Nat. Methods* **2013,** *10,* 403-406.

11.   Liang, R. Q.; Li, W.; Li, Y.; Tan, C. Y.; Li, J. X.; Jin, Y. X.; Ruan, K. C. An Oligonucleotide Microarray for Microrna Expression Analysis Based on Labeling Rna with Quantum Dot and Nanogold Probe *Nucleic Acids Res.* **2005,** *33,* e17.

12.   Bentolila, L. A.; Weiss, S. Single-Step Multicolor Fluorescence in Situ Hybridization Using Semiconductor Quantum Dot-DNA Conjugates *Cell Biochem Biophys* **2006,** *45,* 59-70.

13.   Ioannou, D.; Tempest, H. G.; Skinner, B. M.; Thornhill, A. R.; Ellis, M.; Griffin, D. K. Quantum Dots as New-Generation Fluorochromes for Fish: An Appraisal *Chromosome Res* **2009,** *17,* 519-530.

14.   Zhang, W. J.; Hubbard, A.; Brunhoeber, P.; Wang, Y. X.; Tang, L. Automated Multiplexing Quantum Dots in Situ Hybridization Assay for Simultaneous Detection of Erg and Pten Gene Status in Prostate Cancer *J Mol Diagn* **2013,** *15,* 754-764.

15. Wu, S. M.; Zha, X.; Zhang, Z. L.; Xie, H. Y.; Tian, Z. Q.; Peng, J.; Lu, Z. X.; Pang, D. W.; Xie, Z. X. Quantum-Dot-Labeled DNA Probes for Fluorescence in Situ Hybridization (Fish) in the Microorganism Escherichia Coli *Chemphyschem* **2006,** *7*, 1062-1067.

Chapter 4

In Vivo Fluorescence Imaging in the Short-wave Infrared

4.1 Overview of the Following Sections
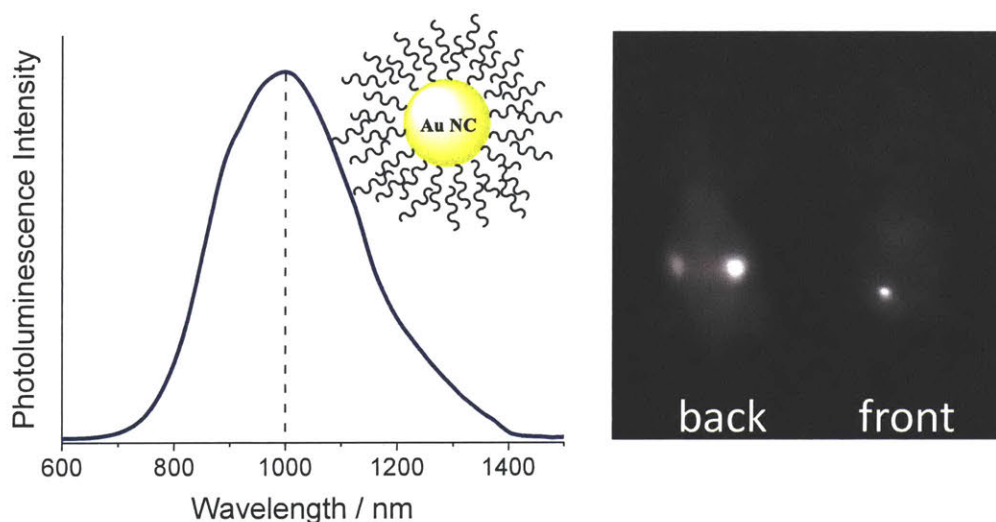
Figure 4-1. Gold Nanoclusters that emit beyond 1000 nm are used for shortwave infrared *in vivo* imaging.

In the previous three chapters, we described using water-soluble QDs for visible *in vitro* imaging, and in the next three chapters we will talk about short-wave infrared (SWIR, 1.0-2.0 μm) *in vivo* imaging. *In vivo* fluorescence imaging in the SWIR region has drawn increasing attention recently as the unique optical properties of the tissue in this region enable improved contrast and spatial resolution over visible and NIR imaging for deep tissue imaging.[1-5] This technology has been shown to be a useful tool for non-invasive *in vivo* imaging as InGaAs-based SWIR detectors are

becoming more inexpensive, more portable, and more widely available.[6-7] However, wide-spread use and clinical applications of this technique continuous to be limited by the poor availability of SWIR emitters with high quantum efficiency, low toxicity, and sufficient physiological stability.[9-10]

Metal nanoclusters, especially gold nanoclusters (Au NCs), have been shown to have tunable emission similar to that of semiconductor QDs.[12-14] The use of visible and near infrared (NIR, 0.7-1.0 μm) -emitting gold nanoclusters (Au NCs), previously proposed for *in vivo* imaging, has been limited to some extent by low quantum yields (QYs) and the limited penetration of visible light in tissues.[15-17] Since Au has been demonstrated to be biocompatible and potentially nontoxic, we aim to tune the emission of Au NCs to the SWIR region and use them as fluorescent probes for *in vivo* imaging. Here we report SWIR-emitting Au NCs with a relatively high photoluminescence QY for this wavelength range (0.6% to 3.8% for λ_{em} = 1000 to 900 nm) and excellent stability under physiological conditions. We show that surface ligand chemistry is critical to achieving these properties. We demonstrate the potential of these SWIR-emitting Au NCs for *in vivo* imaging in mice. The Au NCs have a hydrodynamic diameter that is small (~5 nm) enough that they exhibit a rapid renal clearance, and images taken in the SWIR region show better resolution of the blood vessels than in the NIR region (Figure 4-1).

4.2 Imaging in the SWIR

Deep tissue imaging has been realized using ionizing radiation, such as X-ray and gamma ray imaging. However, these procedures pose a potential risk to biological tissues, and thus fluorescence imaging with lower energy photons is highly preferred. The quality of *in vivo* fluorescence imaging has been largely limited by contrast, which is a function of tissue scattering

and absorption. For Rayleigh scattering, where the scattering particles are much smaller than the wavelength of incoming light, the scattering intensity is inversely proportional to the fourth power of the wavelength, thus tissue scattering can be largely reduced at longer wavelengths. In most tissues, absorbance is dominated by water, melanin, and hemoglobin (Hb), each of which has local minima and maxima of transmission.[8] Therefore, a careful selection of an appropriate imaging wavelength region that takes both parameters into consideration is of critical importance in order to realize deep tissue imaging.
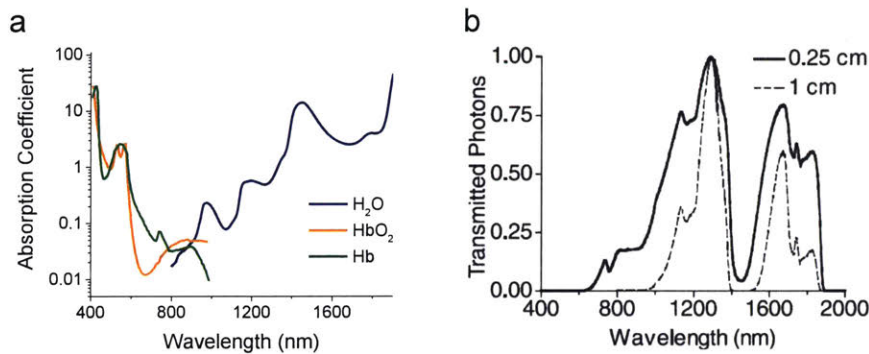
Figure 4-2. (a) Light absorption spectra of hemoglobin and water (part of the Figure is adapted from ref.[18]). (b) The relative number of transmitted photons as a function of wavelength at tissue thicknesses of 0.25 cm (solid line) or 1 cm (dashed line). Figure is adapted from ref.[8].

According to previous studies of photon transmittance of tissue samples, 0.7-1.7 μm is the optical wavelength band for *in vivo* imaging as photons in this range has the highest penetration rate through the tissues, mainly due to the strong Hb absorbance at <700 nm and lipid/water absorbance beyond 1.7 μm (Figure 4-2a).[18-20] Since the absorption spectra of both Hb and water show a minimum in the traditional NIR region, this window has been explored the most for *in vivo* imaging.[21-22] Despite the big progress of NIR technology, deep tissue imaging remains challenging as a result of tissue scattering in the NIR region. Current applications are still limited to primarily small preclinical models (mice, small rates) or to optically accessible tissues (i.e. esophagus, colon)

in humans.[23-24] Since tissue scattering is further reduced in the SWIR, researchers are investigating this region for applications that require greater penetration depths.

Although SWIR light is not visible to the eye, the light interacts with objects in a similar manner to visible light. That is, SWIR light is reflective and can create shadows and contrast in its imagery.[25] SWIR technology has found applications in astronomy and military defense, where sensitive SWIR sensors made of mercury cadmium telluride (HgCdTe) or indium antimonide (InSb) are utilized. However, these sensors have to work at extremely low temperatures to reach a high signal-to-noise ratio, requiring a large cooling system installed, which is not suitable for clinical applications. The development of highly sensitive indium gallium arsenide (InGaAs) sensors has promoted the use of this technology in fluorescent biomedical imaging research. With the price decreasing from above \$120K to less than \$35K and the exempt of some SWIR cameras from the International Traffic in Arms Regulations, this setup is becoming more available to most research institutes.

Several recent studies have shown that better contrast and resolution images with better contrast and resolution of *in vivo* images can be obtained using SWIR technology compared to traditional NIR imaging. For example, the Dai group reported using single-walled carbon nanotube (SWNT)-IRDye-800 conjugates for *in vivo* imaging in both the NIR region with a silicon camera and the SWIR region with an InGaAs camera;[2] the Bawendi group has likewise used indocyanine green as the contrast agent to image a mouse brain vasculature.[11] As shown in Figure 4-3, the image obtained by the SWIR camera has significantly increased contrast and better resolved details of the blood vessels of the mouse vasculature. We anticipate that *in vivo* imaging in the SWIR will be the trend of *in vivo* fluorescence imaging research, and that this technology is promising for future clinical applications.
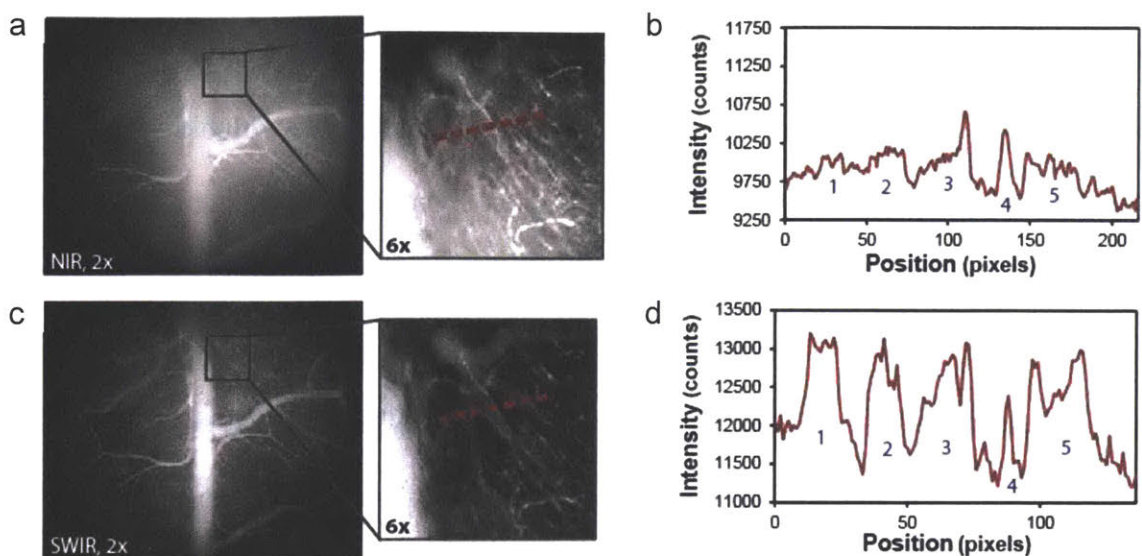
Figure 4-3. (a) Microscopy of brain vasculature of a mouse through a cranial window with NIR detection has poor contrast. (b) The intensity across a line of interest shows insufficient contrast to resolve overlapping vessels from background signal. (c) Using 1300 nm long-pass SWIR detection greatly improves image contrast and (d) resolution of vessels. Figures are adapted from ref.[11].

4.3   Contrast Agents for SWIR *In Vivo* Imaging
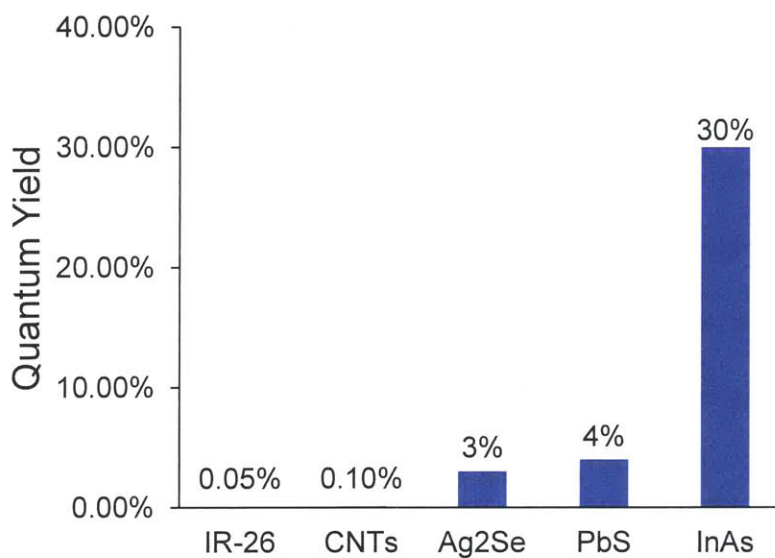
Figure 4-4. Quantum yields of several commonly used SWIR emitters. Figure is reproduced from ref.[3].

While the InGaAs camera is becoming available, further steps toward the development of SWIR *in vivo* imaging will require more efficient contrast agents. There have been few reports about SWIR emitters that can satisfy high quantum efficiency, excellent water solubility, non-toxicity, and good physiological stability at the same time. Commonly used SWIR emitters include organic dyes, single-walled carbon nanotubes (SWNTs), Ag_2Se QDs, PbS QDs, InAs QDs, and rare earth doped nanoparticles (Figure 4-4). Most of the SWIR-emitting organic dyes like IR-26 are highly hydrophobic and suffer from extremely low quantum yield (QY) once being transferred into aqueous solvents.[9-10] SWNTs, similarly, exhibit low quantum efficiency and poor stability.[26] While QDs have higher QY and better photostability, the potential toxicity excludes them as candidates for clinical SWIR *in vivo* imaging. Hence, developing a potentially nontoxic SWIR contrast agent with good QY and excellent physiological stability remains challenging.

4.4 Luminescent Gold Nanoclusters

Luminescent noble metal nanoclusters, especially Au NCs with potentially low toxicity, ultrasmall size, excellent photostability, and facile surface functionalization, are being actively pursued as novel species of fluorescent materials.[13, 27] Composed of several to up to a few hundred Au atoms, these Au NCs exhibit quantum confinement effects and molecule-like properties.[13, 28-30] Au NCs with tunable emission from the ultraviolet to the NIR region have been reported in the last several decades, and utilization of those Au NCs for *in vitro* cell labeling and *in vivo* fluorescence imaging applications is an active research area.[14-15, 31-32] In earlier reports, Au NCs with emission in the NIR region are being particularly investigated for *in vivo* imaging applications owing to the enhanced tissue penetration enabled by NIR light.[15-17] As *in vivo* imaging in the SWIR range has further reduced background noise from tissue scattering than traditional visible and NIR imaging, we focus our effort on obtaining Au NCs for SWIR *in vivo* imaging in this work.

Recently, substantial progress has been made to improve the photoluminescence (PL) QY of Au NCs,[33] to characterize and establish their atomically precise structures,[34-36] and to understand the mechanism of their luminescence.[37] However, most of the luminescent Au NCs reported so far have emission <950 nm[15, 38] and relatively low PL QYs,[39] limiting their *in vivo* applications. Although the luminescence mechanism of Au NCs is still debated and has not yet been well understood, it is clear that the type and stacking structure of surface ligands play a critical role in the PL properties of Au NCs.[37, 40] Emission of Au NCs in the 800-950 nm range has been achieved by using a variety of ligands.[41-45] Zwitterionic and bidentate thiol molecules in particular, have been explored as surface ligands and were shown to result in a higher QY and longer wavelength emission.[46-47] We hypothesized that these zwitterionic and bidentate thiol ligands may enable expansion of the emission spectrum of Au NCs to the SWIR range, thus our work would focus on tuning the emission spectrum of Au NCs to beyond 1000 nm using a lipoic acid based zwitterionic ligand.

References

1.   Hong, G. S.; Diao, S.; Chang, J. L.; Antaris, A. L.; Chen, C. X.; Zhang, B.; Zhao, S.; Atochin, D. N.; Huang, P. L.; Andreasson, K. I., *et al*. Through-Skull Fluorescence Imaging of the Brain in a New near-Infrared Window *Nature Photonics* **2014**, *8*, 723-730.

2.   Hong, G. S.; Lee, J. C.; Robinson, J. T.; Raaz, U.; Xie, L. M.; Huang, N. F.; Cooke, J. P.; Dai, H. J. Multifunctional in Vivo Vascular Imaging Using near-Infrared Ii Fluorescence *Nature Medicine* **2012**, *18*, 1841-1846.

3.   Bruns, O. T.; Bischof, T. S.; Harris, D. K.; Franke, D.; Shi, Y.; Riedemann, L.; Bartelt, A.; Jaworski, F. B.; Carr, J. A.; Rowlands, C. J., *et al*. Next-Generation in Vivo Optical Imaging with Short-Wave Infrared Quantum Dots *Nature Biomedical Engineering* **2017**, *1*, 0056.

4.   Smith, A. M.; Mancini, M. C.; Nie, S. M. Bioimaging Second Window for in Vivo Imaging *Nature Nanotechnology* **2009**, *4*, 710-711.

5.   Zhang, H. R.; Salo, D.; Kim, D. M.; Komarov, S.; Tai, Y. C.; Berezin, M. Y. Penetration Depth of Photons in Biological Tissues from Hyperspectral Imaging in Shortwave Infrared in Transmission and Reflection Geometries *Journal of Biomedical Optics* **2016**, *21*, 126006.

6.   Sordillo, L. A.; Lindwasser, L.; Budansky, Y.; Leproux, P.; Alfano, R. R. Near-Infrared Supercontinuum Laser Beam Source in the Second and Third near-Infrared Optical Windows Used to Image More Deeply through Thick Tissue as Compared with Images from a Lamp Source *Journal of Biomedical Optics* **2015**, *20*, 030501.

7.   Welsher, K.; Sherlock, S. P.; Dai, H. J. Deep-Tissue Anatomical Imaging of Mice Using Carbon Nanotube Fluorophores in the Second near-Infrared Window *Proceedings of the National Academy of Sciences of the United States of America* **2011**, *108*, 8943-8948.

8.   T., L. Y.; Kim, S.; Nakayama, A.; Stott, N. E.; Bawendi, M.; V., F. J. Selection of Quantum Dot Wavelengths for Biomedical Assays and Imaging *Mol Imaging* **2003**, *2*, 50-64.

9.   Semonin, O. E.; Johnson, J. C.; Luther, J. M.; Midgett, A. G.; Nozik, A. J.; Beard, M. C. Absolute Photoluminescence Quantum Yields of Ir-26 Dye, Pbs, and Pbse Quantum Dots *Journal of Physical Chemistry Letters* **2010**, *1*, 2445-2450.

10.   Hatami, S.; Wurth, C.; Kaiser, M.; Leubner, S.; Gabriel, S.; Bahrig, L.; Lesnyak, V.; Pauli, J.; Gaponik, N.; Eychmuller, A., *et al.* Absolute Photoluminescence Quantum Yields of Ir26 and Ir-Emissive Cd1-Xhgxte and Pbs Quantum Dots - Method- and Material-Inherent Challenges *Nanoscale* **2015**, *7*, 133-143.

11.   Carr, J. A.; Franke, D.; Caram, J. R.; Perkinson, C. F.; Askoxylakis, V.; Datta, M.; Fukumura, D.; Jain, R. K.; Bawendi, M.; Bruns, O. T. Shortwave Infrared Fluorescence Imaging with the Clinically Approved near-Infrared Dye Indocyanine Green *bioRxiv* **2017**.

12.   Zhang, Z. Y.; Xu, L. J.; Li, H. X.; Kong, J. L. Wavelength-Tunable Luminescent Gold Nanoparticles Generated by Cooperation Ligand Exchange and Their Potential Application in Cellular Imaging *RSC Adv.* **2013**, *3*, 59-63.

13.   Zheng, J.; Nicovich, P. R.; Dickson, R. M. Highly Fluorescent Noble-Metal Quantum Dots *Annu. Rev. Phys. Chem.* **2007**, *58*, 409-431.

14.   Zheng, J.; Zhou, C.; Yu, M. X.; Liu, J. B. Different Sized Luminescent Gold Nanoparticles *Nanoscale* **2012**, *4*, 4073-4083.

15.   Wu, X.; He, X. X.; Wang, K. M.; Xie, C.; Zhou, B.; Qing, Z. H. Ultrasmall near-Infrared Gold Nanoclusters for Tumor Fluorescence Imaging in Vivo *Nanoscale* **2010**, *2*, 2244-2249.

16.   Sun, C. J.; Yang, H.; Yuan, Y.; Tian, X.; Wang, L. M.; Guo, Y.; Xu, L.; Lei, J. L.; Gao, N.; Anderson, G. J., *et al.* Controlling Assembly of Paired Gold Clusters within Apoferritin

Nanoreactor for in Vivo Kidney Targeting and Biomedical Imaging *J. Am. Chem. Soc.* **2011,** *133,* 8617-8624.

17.   Zhou, C.; Long, M.; Qin, Y. P.; Sun, X. K.; Zheng, J. Luminescent Gold Nanoparticles with Efficient Renal Clearance *Angew. Chem. Int. Ed.* **2011,** *50,* 3168-3172.

18.   Weissleder, R. A Clearer Vision for in Vivo Imaging *Nat. Biotechnol.* **2001,** *19,* 316-317.

19.   Frangioni, J. V. In Vivo near-Infrared Fluorescence Imaging *Curr. Opin. Chem. Biol.* **2003,** *7,* 626-634.

20.   Ntziachristos, V.; Bremer, C.; Weissleder, R. Fluorescence Imaging with near-Infrared Light: New Technological Advances That Enable in Vivo Molecular Imaging *European Radiology* **2003,** *13,* 195-208.

21.   Sevick-Muraca, E. M.; Houston, J. P.; Gurfinkel, M. Fluorescence-Enhanced, near Infrared Diagnostic Imaging with Contrast Agents *Curr. Opin. Chem. Biol.* **2002,** *6,* 642-650.

22.   Achilefu, S.; Dorshow, R. B.; Bugaj, J. E.; Rajagopalan, R. Novel Receptor-Targeted Fluorescent Contrast Agents for in Vivo Tumor Imaging *Investigative Radiology* **2000,** *35,* 479-485.

23.   Zhou, H. Y.; Yan, Y.; Ee, X. P.; Hunter, D. A.; Akers, W. J.; Wood, M. D.; Berezin, M. Y. Imaging of Radicals Following Injury or Acute Stress in Peripheral Nerves with Activatable Fluorescent Probes *Free Radical Biol. Med.* **2016,** *101,* 85-92.

24.   Iftimia, N.; Iyer, A. K.; Hammer, D. X.; Lue, N.; Mujat, M.; Pitman, M.; Ferguson, R. D.; Amiji, M. Fluorescence-Guided Optical Coherence Tomography Imaging for Colon Cancer Screening: A Preliminary Mouse Study *Biomedical Optics Express* **2012,** *3,* 178-191.

25.   Carr, J. A.; Valdez, T. A.; Bruns, O. T.; Bawendi, M. G. Using the Shortwave Infrared to Image Middle Ear Pathologies *Proceedings of the National Academy of Sciences of the United States of America* **2016**, *113*, 9989-9994.

26.   Welsher, K.; Liu, Z.; Sherlock, S. P.; Robinson, J. T.; Chen, Z.; Daranciang, D.; Dai, H. J. A Route to Brightly Fluorescent Carbon Nanotubes for near-Infrared Imaging in Mice *Nature Nanotechnology* **2009**, *4*, 773-780.

27.   Yuan, X.; Luo, Z. T.; Yu, Y.; Yao, Q. F.; Xie, J. P. Luminescent Noble Metal Nanoclusters as an Emerging Optical Probe for Sensor Development *Chem. Asian J.* **2013**, *8*, 858-871.

28.   Chen, S. W.; Ingram, R. S.; Hostetler, M. J.; Pietron, J. J.; Murray, R. W.; Schaaff, T. G.; Khoury, J. T.; Alvarez, M. M.; Whetten, R. L. Gold Nanoelectrodes of Varied Size: Transition to Molecule-Like Charging *Science* **1998**, *280*, 2098-2101.

29.   Zhou, M.; Zeng, C. J.; Chen, Y. X.; Zhao, S.; Sfeir, M. Y.; Zhu, M. Z.; Jin, R. C. Evolution from the Plasmon to Exciton State in Ligand-Protected Atomically Precise Gold Nanoparticles *Nat. Commun.* **2016**, *7*, 13240.

30.   Qian, H. Z., M.; Wu, Z.; Jin, R. Quantum Sized Gold Nanoclusters with Atomic Precision *Acc. Chem. Res.* **2012**, *45*, 1470-1479.

31.   Shang, L.; Nienhaus, G. U. Gold Nanoclusters as Novel Optical Probes for in Vitro and in Vivo Fluorescence Imaging *Biophys. Rev.* **2012**, *4*, 313-322.

32.   Fernandez, T. D.; Pearson, J. R.; Leal, M. P.; Torres, M. J.; Blanca, M.; Mayorga, C.; Le Guevel, X. Intracellular Accumulation and Immunological Properties of Fluorescent Gold Nanoclusters in Human Dendritic Cells *Biomaterials* **2015**, *43*, 1-12.

33.   Pyo, K.; Thanthirige, V. D.; Kwak, K.; Pandurangan, P.; Ramakrishna, G.; Lee, D. Ultrabright Luminescence from Gold Nanoclusters: Rigidifying the Au(I)-Thiolate Shell *J. Am. Chem. Soc.* **2015,** *137*, 8244-8250.

34.   Jin, R. C. Atomically Precise Metal Nanoclusters: Stable Sizes and Optical Properties *Nanoscale* **2015,** *7*, 1549-1565.

35.   Zhu, M.; Aikens, C. M.; Hollander, F. J.; Schatz, G. C.; Jin, R. Correlating the Crystal Structure of a Thiol-Protected Au-25 Cluster and Optical Properties *J. Am. Chem. Soc.* **2008,** *130*, 5883-5885.

36.   Salorinne, K.; Malola, S.; Wong, O. A.; Rithner, C. D.; Chen, X.; Ackerson, C. J.; Hakkinen, H. Conformation and Dynamics of the Ligand Shell of a Water-Soluble Au-102 Nanoparticle *Nat. Commun.* **2016,** *7*, 10401.

37.   Wu, Z. K.; Jin, R. C. On the Ligand's Role in the Fluorescence of Gold Nanoclusters *Nano Lett.* **2010,** *10*, 2568-2573.

38.   Liu, J. B.; Yu, M. X.; Ning, X. H.; Zhou, C.; Yang, S. Y.; Zheng, J. Pegylation and Zwitterionization: Pros and Cons in the Renal Clearance and Tumor Targeting of near-Ir-Emitting Gold Nanoparticles *Angew. Chem. Int. Ed.* **2013,** *52*, 12572-12576.

39.   Yu, Y.; Luo, Z. T.; Chevrier, D. M.; Leong, D. T.; Zhang, P.; Jiang, D. E.; Xie, J. P. Identification of a Highly Luminescent Au-22(Sg)(18) Nanocluster *J. Am. Chem. Soc.* **2014,** *136*, 1246-1249.

40.   Luo, Z. T.; Yuan, X.; Yu, Y.; Zhang, Q. B.; Leong, D. T.; Lee, J. Y.; Xie, J. P. From Aggregation-Induced Emission of Au(I)-Thiolate Complexes to Ultrabright Au(0)@Au(I)-Thiolate Core-Shell Nanoclusters *J. Am. Chem. Soc.* **2012,** *134*, 16662-16670.

41.   Wang, G. L.; Huang, T.; Murray, R. W.; Menard, L.; Nuzzo, R. G. Near-Ir Luminescence of Monolayer-Protected Metal Clusters *J. Am. Chem. Soc.* **2005,** *127,* 812-813.

42.   Wan, X. K.; Xu, W. W.; Yuan, S. F.; Gao, Y.; Zeng, X. C.; Wang, Q. M. A near-Infrared-Emissive Alkynyl-Protected Au-24 Nanocluster *Angew. Chem. Int. Ed.* **2015,** *54,* 9683-9686.

43.   Crawford, S. E.; Andolina, C. M.; Smith, A. M.; Marbella, L. E.; Johnston, K. A.; Straney, P. J.; Hartmann, M. J.; Millstone, J. E. Ligand-Mediated "Turn on," High Quantum Yield near-Infrared Emission in Small Gold Nanoparticles *J. Am. Chem. Soc.* **2015,** *137,* 14423-14429.

44.   Lee, D.; Donkers, R. L.; Wang, G. L.; Harper, A. S.; Murray, R. W. Electrochemistry and Optical Absorbance and Luminescence of Molecule-Like Au-38 Nanoparticles *J. Am. Chem. Soc.* **2004,** *126,* 6193-6199.

45.   Wang, G. L.; Guo, R.; Kalyuzhny, G.; Choi, J. P.; Murray, R. W. Nir Luminescence Intensities Increase Linearly with Proportion of Polar Thiolate Ligands in Protecting Monolayers of Au-38 and Au-140 Quantum Dots *J. Phys. Chem. B* **2006,** *110,* 20282-20289.

46.   Le Guevel, X.; Tagit, O.; Rodriguez, C. E.; Trouillet, V.; Leal, M. P.; Hildebrandt, N. Ligand Effect on the Size, Valence State and Red/near Infrared Photoluminescence of Bidentate Thiol Gold Nanoclusters *Nanoscale* **2014,** *6,* 8091-8099.

47.   Aldeek, F.; Muhammed, M. A. H.; Palui, G.; Zhan, N. Q.; Mattoussi, H. Growth of Highly Fluorescent Polyethylene Glycol- and Zwitterion-Functionalized Gold Nanoclusters *Acs Nano* **2013,** *7,* 2509-2521.

Chapter 5

SWIR-emitting Gold Nanoclusters

5.1 Synthesis of SWIR-emitting Au NCs

Au NCs are generally synthesized by reducing chloroauric acid with a reducing agent or by heating in the presence of thiol ligands such as glutathione, dihydrolipoic acid, or proteins like bovine serum albumin.[1-3] In this study, we first synthesized lipoic acid-based sulfobetaine (LA-sulfobetaine) -capped SWIR-emitting Au NCs in water by modifying a literature method that reduces chloroauric acid in the presence of LA-sulfobetaine.[4] These LA-sulfobetaine capped Au
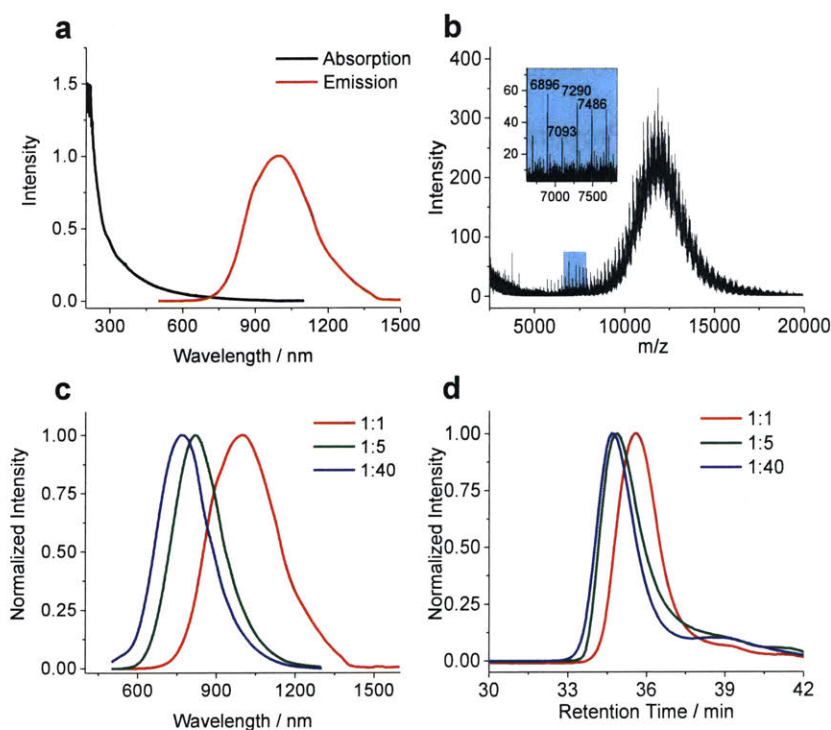
Figure 5-1. (a) Absorption and photoluminescence spectra and (b) MALDI spectrum of LA-sulfobetaine capped Au NCs (LA-sulfobetaine:Au=1:1, QY=0.6%), inset is a zoomed-in area indicated in the blue region on the spectrum. (c) Photoluminescence spectra and (d) Gel filtration chromatography (GFC) traces of Au NCs (1:1, 1:5, and 1:40, QY=0.6%, 6.2%, and 14.9%, respectively). PL spectra were acquired using 532 nm excitation.

NCs have an average inorganic core size of 1.6 nm. Their emission peak is centered at ~1,000 nm (Figure 5-1a), with an initial QY of 0.6%. Matrix-assisted laser desorption/ionization (MALDI) analysis shows a mass interval of 197 (Figure 5-1b, Inset), which matches the mass of Au, and the range of Au atoms in the Au NCs is estimated to be 20-50 by setting the number of Au atoms and ligands as integers for each m/z value. Au NCs with higher initial QYs can be synthesized by decreasing the chloroauric acid to LA-sulfobetaine ratio, presumably due to tuning of the core sizes and the existence of extended ligand layers. As the weight ratio of chloroauric acid hydrate to LA-sulfobetaine decreases from 1:1 to 1:5, and then to 1:40, the QY increases from 0.6% to 6.2% and 14.9%, respectively. However, the emission peak also blue-shifts (~200 nm) out of the SWIR range (Figure 5-1c), likely due to different core sizes and surface Au-thiolate staple motifs created in the presence of the additional ligands during synthesis.[5] This blue-shift of the emission counterbalances the QY improvement for potential SWIR imaging applications. As we see from the images of the three Au NCs samples (same Au molar concentration) taken using an InGaAs camera with two 1,000 nm long pass (LP) filters, the detected signal intensity of the higher QY, blue shifted Au NCs (1:40) is significantly weaker than that of lower QY but red shifted Au NCs (1:1 and 1:5) (Figure 5-2).
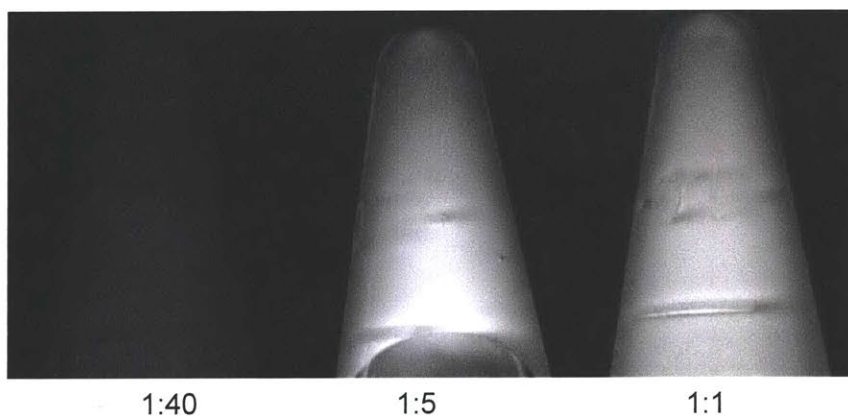
Figure 5-2. Images of Au NCs (1:40, 1:5, and 1:1, same concentration on Au basis) in Eppendorf tubes taken with an InGaAs camera and 808 nm excitation.

Concurrent with the increased QY and the blue-shift in emission, the hydrodynamic diameter (HD) also slightly increases with more ligands present during synthesis (Figure 5-1d) (4.5 nm, 5.0 nm and 5.2 nm, respectively according to the GFC calibration curve Figure 5-3). The inorganic
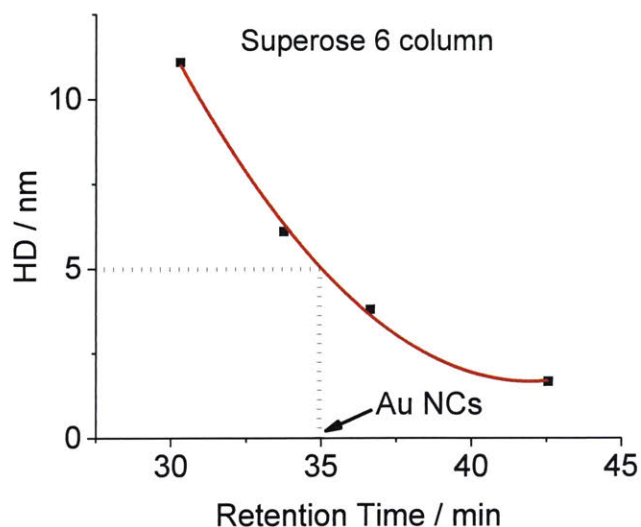
Figure 5-3. A Superose 6 size-exclusion column was calibrated with protein standards containing γ-globulin, ovalbumin, myoglobin, and vitamin B12 from Bio-Rad (black squares). The red curve is a calibration curve based on the protein standards. Our Au NCs (1:5) had a retention time of about 35 min (arrow), which corresponds to a HD of 5 nm.
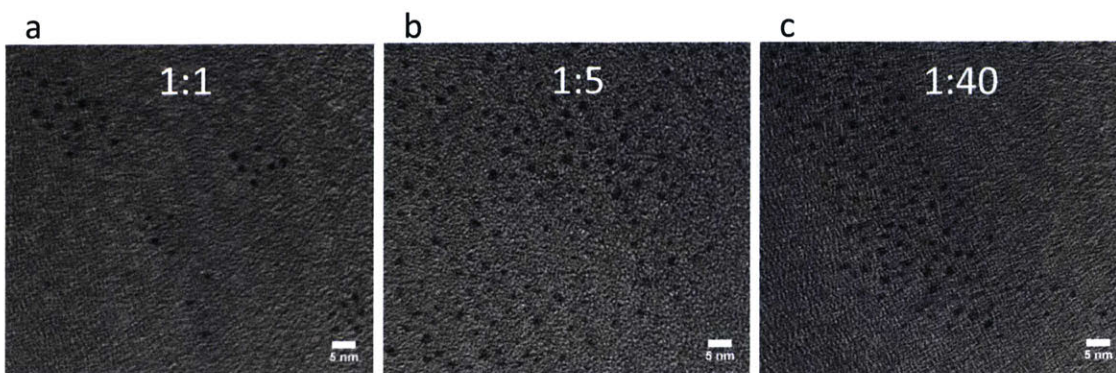
Figure 5-4. TEM images of (a) Au NCs (1:1), (b) Au NCs (1:5), and (c) Au NCs (1:40). Scale bar represents 5 nm.

core diameters of these samples are 1.6 nm (1:1), 1.5 nm (1:5), and 1.3 nm (1:40), respectively (Figure 5-4), indicating the presence of an extended ligand shell that gives rise to the increased HD. We speculate that an extra layer of LA-sulfobetaine ligands may be bound to the surface of Au NCs (1:5) and Au NCs (1:40) through electrostatic interactions between ligands or formation of disulfide bonds between LA-sulfobetaine ligands and exposed thiols on the surface of Au NCs. Consistent with this hypothesis, MALDI spectra of Au NCs (1:5) and Au NCs (1:40) (Figure 5-5) show an increased fragmentation, indicating more capping ligands. We hypothesize that a two-step stacking of LA-sulfobetaine ligands on Au NCs (1:1) would help increase the amount of surface capping ligand, and that will further lead to increase of QY and perhaps the signal intensity in the SWIR region.
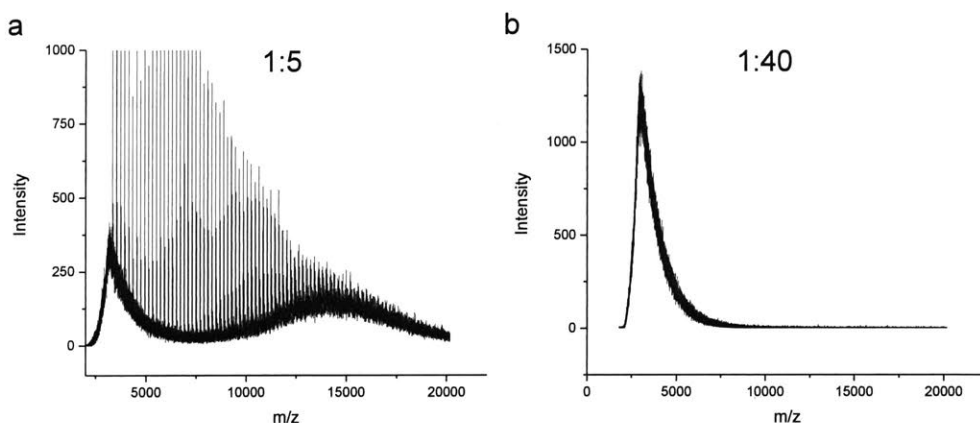
Figure 5-5. MALDI spectra of Au NCs (1:5) and Au NCs (1:40).

5.2 Post Ligand Treatment to Increase the QY of Au NCs

To elucidate whether an extended ligand shell contributes to the increased QY and the blue-shifted emission of Au NCs (1:5 or 1:40), we incubated the low QY Au NCs (1:1) with extra LA-sulfobetaine ligands. Indeed, following treatment with additional LA-sulfobetaine ligands, the QY of Au NCs (1:1) significantly increases from 0.6% to 3.8%, accompanied by a ~100 nm blue-shift
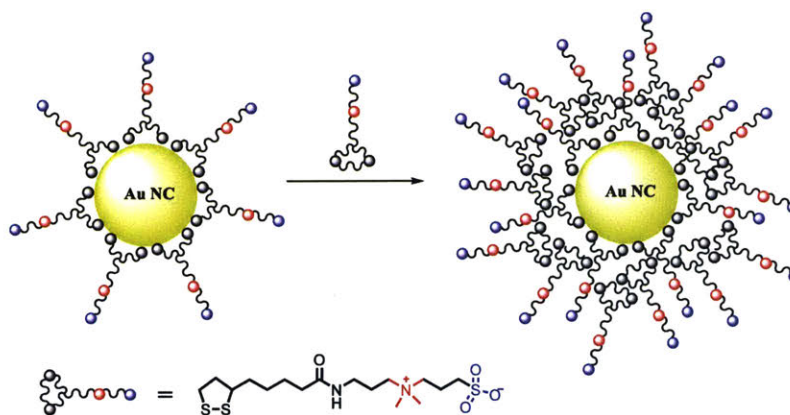
Scheme 5-1. Schematic illustration of zwitterionic ligands capped Au NCs, treated with extra zwitterionic ligands, resulting in an expanded ligand shell.

(to 900 nm) (Figure 5-6b). Since it is unlikely that the disulfide bond of LA-sulfobetaine can change the core size of the initial Au NCs (1:1),[6-7] which is also verified by inductively coupled plasma optical emission spectrometry (ICP-OES) result that 96% of the Au was conserved after additional ligand treatment, we hypothesized the formation of an extended ligand shell (verified by an increase of 0.5 nm in HD shown by GFC, Figure 5-6c), likely through electrostatic forces between ligands, and that this led to increased QYs and slight blue-shifts in emissions. Thermogravimetric analysis (TGA) demonstrates the extended ligand shell of Au NCs after treatment with additional LA-sulfobetaine ligands (Figure 5-7). All samples were purified using a desalting column to remove extra free ligands and salts prior to TGA. As shown in Figure 5-7, Au NCs (1:1) lose ~40% of their original weight when heated to 500 °C, while Au NCs treated with extra ligands lose ~75% of their original weight. We further quantified the amount of ligands bound to Au NCs via liquid chromatography-mass spectrometry (LC-MS) and inductively coupled plasma optical emission spectrometry (ICP-OES) (working function is provided in experimental details). Au NCs were dissolved with potassium cyanide prior to LC-MS and ICP-OES measurements to quantify the concentration of LA-sulfobetaine and Au, respectively. The results
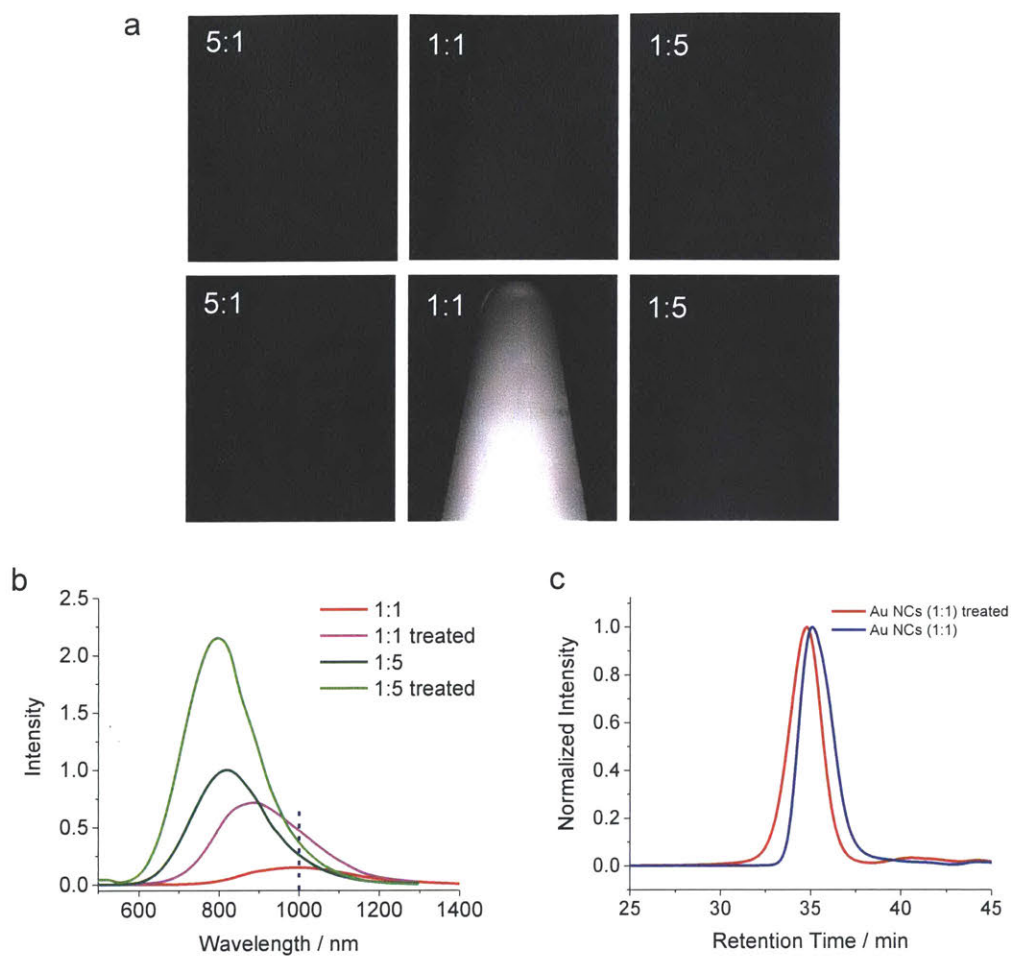
Figure 5-6. (a) Images of Au NCs (5:1, 1:1, and 1:5) (0.25 mg/mL on Au basis) in Eppendorf tubes before (upper row) and after (bottom row) treated with extra LA-sulfobetaine ligands, taken using InGaAs SWIR camera under 808 nm excitation. (b) PL spectra of Au NCs (1:1 and 1:5) before and after treated with LA-sulfobetaine ligands at 532 nm excitation (normalized based on the QYs). (c) GFC traces of Au NCs (1:1) before and after treated with extra LA-sulfobetaine ligands.

show that there is 0.866 mg ligand / mg of Au in nontreated Au NCs, whereas for ligand treated Au NCs this value was found to be 3.949 (Table 5-1). Since the Au NCs (1:5) initially have a signal intensity in the SWIR range that is similar to Au NCs (1:1) (Figure 5-2), we treated both samples with extra ligands for comparison. Images of treated and untreated Au NCs (5:1, 1:1 and 1:5) taken using an InGaAs camera with two 1,000 nm LP filters show that Au NCs (1:1) treated

with extra LA-sulfobetaine ligands are the brightest (Figure 5-6a). There is also a slight increase

of the SWIR signal intensity of Au NCs (1:5) after treatment, which is due to an increase in the

QY. However, the blue-shift of the emission results in less signal beyond 1,000 nm (Figure 5-6b).
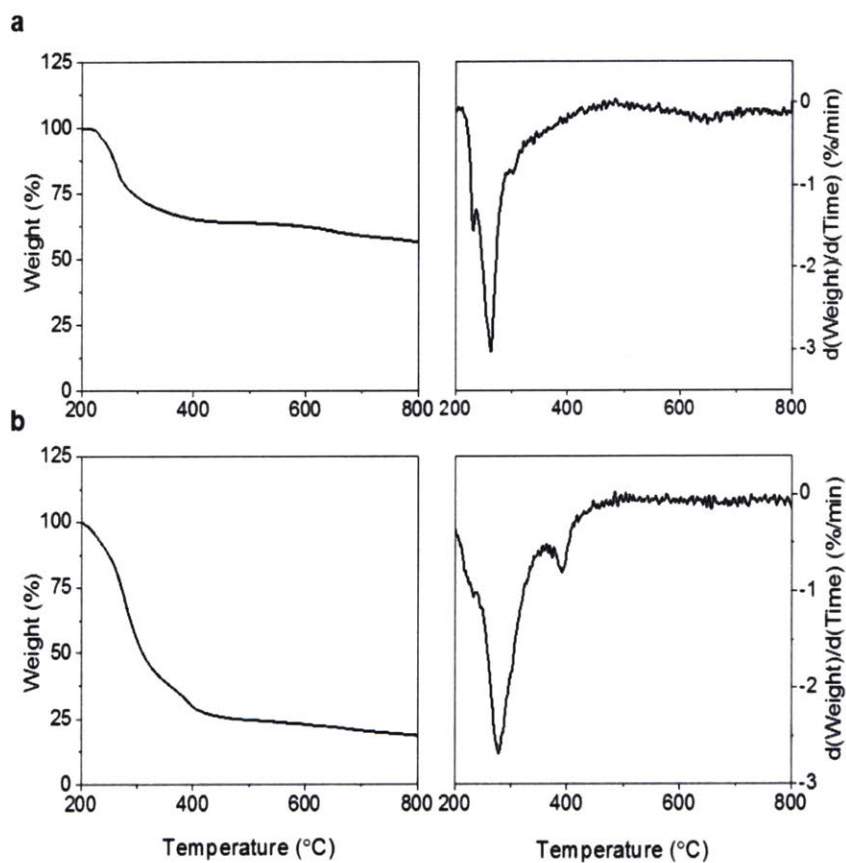
Figure 5-7. TGA curves of (a) Au NCs (1:1), and (b) Au NCs (1:1) treated with extra LA-sulfobetaine ligands.

Table 5-1. Quantitative analysis of ligand to gold ratio of Au NCs. Au NCs were dissolved using potassium cyanide, followed by LC-MS analysis. The concentration of LA-sulfobetaine was calculated using the standard curve in Figure 5-10, and [Au] was measured using ICP-OES.

Au NCs	Volume (mL)	Integrated Area	[LA-sulfobetaine] (mg/mL)	[Au] (mg/mL)	LA-sulfobetaine/Au (mg/mg)
Nontreated	0.51	477.7	0.40762	0.47225	0.86631
Treated	0.66	1328.57	1.39597	0.35350	3.94899

Although previous work has revealed some insights into the origin of the luminescence from Au NCs, the underlying mechanism has not yet been well understood.[8-10] Size (or number of gold atoms), the structure of the nanocluster cores, the packing of gold-thiolate motifs, and the types of ligands all play an important role.[8, 11-14] In our case, the extended ligand shell contributes to the blue-shifted luminescence and higher QY, which is probably due to rigidification of the gold shell structure that consists several Au-S motifs.[15-16] To maximize the SWIR signal from Au NCs, we need to balance a higher QY but a shorter emission maximum with a lower QY but a longer emission maximum. Au NCs (1:1) treated with extra ligands (Figure 5-6a) provide the highest brightness in the SWIR, and we use these to demonstrate *in vivo* SWIR imaging. This preparation has a relatively good QY (3.8%) and an emission maximum at 900 nm.

5.3 Stability Tests of SWIR-emitting Au NCs

SWIR *in vivo* imaging can be advantageous as it can allow for deeper penetration and higher contrast and resolution compared to traditional NIR imaging. Longer-wavelength photons in the SWIR region experience less scattering in biological tissues. Combined with lower auto-fluorescence, this enables increased sensitivity and contrast.[17] With their small HD, high stability,
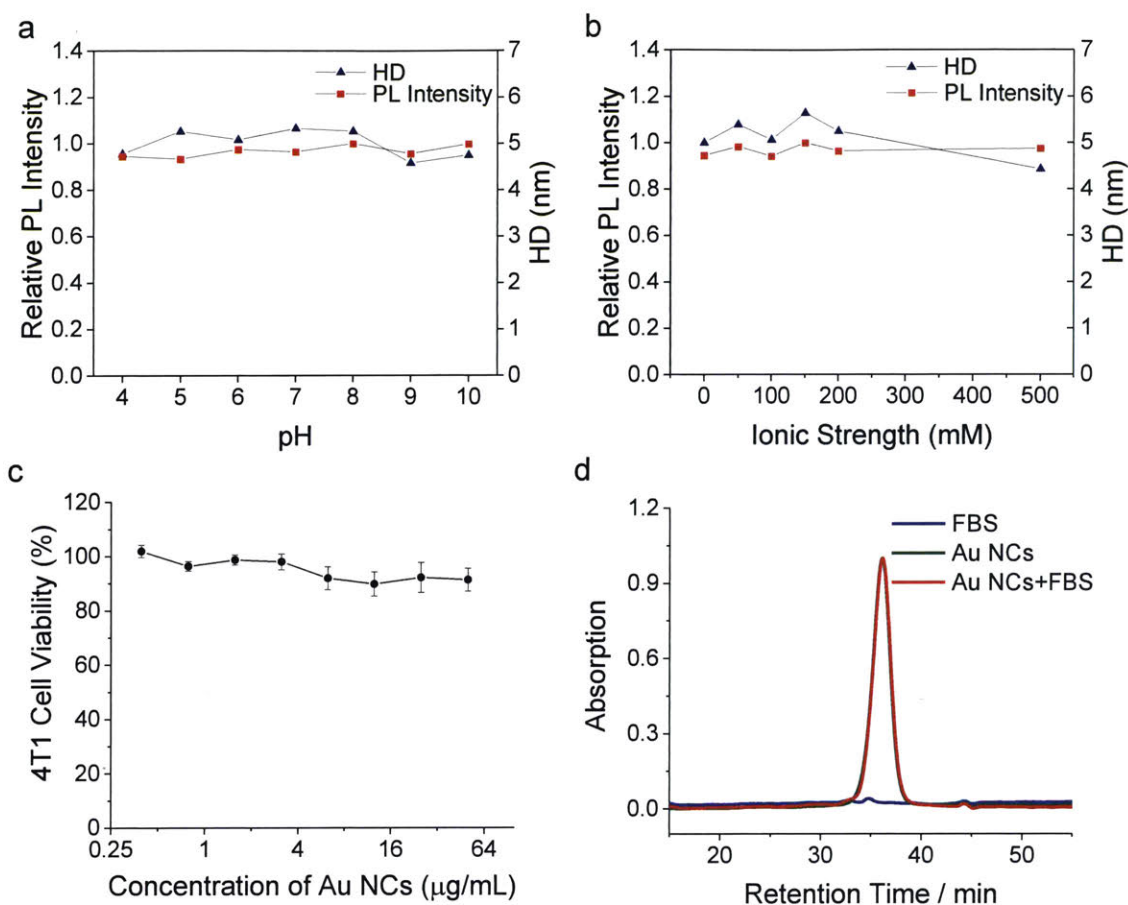
Figure 5-8. Relative photoluminescence intensity and hydrodynamic diameter of Au NCs at (a) different pH values (4-10) and (b) different ionic strength. (c) 4T1 cell viability after treatment with Au NCs at different concentrations for 3 days. (d) GFC traces of FBS, Au NCs (1:1) treated with LA-sulfobetaine ligands, and Au NCs (1:1) treated with LA-sulfobetaine ligands in FBS, respectively. Absorption was detected at 750 nm.

SWIR emission, and comparatively high QYs, these Au NCs are promising probes for *in vivo* imaging. Before applying these NCs to *in vivo* imaging, we performed a pH and ionic strength stability test. Au NCs were dispersed in aqueous solutions of different pH values and sodium chloride solutions of different ionic strengths (0-500 mM), respectively. Both the PL intensity and HD of the Au NCs demonstrated high stability within physiological pH range and over a broad range of ionic strength (Figure 5-8 a-b). Moreover, Au NCs show minimal cell toxicity, as

evidenced by an *in vitro* MTT assay (Figure 5-8c). Serum stability tests were also carried out to investigate the stability of the Au NCs against non-specific binding with serum proteins. Au NCs (900 nm, 3.8% QY) were incubated with fetal bovine serum (FBS) or PBS at 37 °C for 4 hours, and images under an InGaAs camera shows negligible difference in PL intensity (Figure 5-9). In addition, the retention time of Au NCs before and after incubation with FBS shows no significant changes (Figure 5-8c), indicating that the LA-sulfobetaine ligand not only prevents Au NCs from degradation but also minimizes adsorption of serum proteins in biologically relevant environments, consistent with previously published results.[18-20]
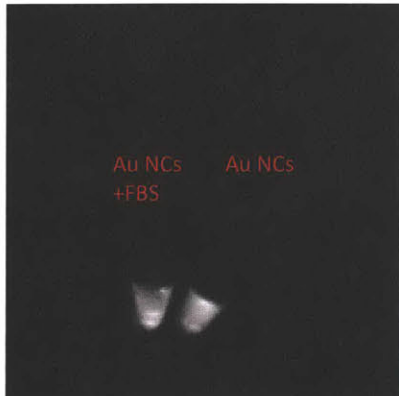
Figure 5-9. Images of Au NCs in Eppendorf tubes after incubating with FBS for 4 h at 37 °C (left) and Au NCs without incubation (right).

These experiments demonstrate that our SWIR-emitting Au NCs exhibit high SWIR brightness, a small HD below renal filtration threshold, excellent stability against pH and ionic strength, and minimal non-specific binding. These Au NCs are ready to be employed as contrast agents for biological imaging applications.

5.4 Experimental Details

Materials

Lipoic acid, trimethylamine, methanesulfonyl chloride, organic solvents (acetone nitrile, methanol, chloroform, etc.), PBS buffer, Fetal bovine serum (FBS), and other reagents were purchased from Sigma Aldrich (St. Louis, MO, USA) unless otherwise noted. N,N-dimethyl-1,3-propanediamine, 1,3-propanesultone, and hydrogen tetrachloroaurate (III) hydrate, 99.9% (metals basis) were purchased from Alfa Aesar (Haverhill, MA, USA). All chemicals were used as received.

Instrumentation

Transmission electron microscopy (TEM) images of LA-sulfobetaine Au NCs were taken on a JEOL 2010 advanced high performance TEM. Absorption spectra were taken using a Cary 5000 UV-Vis-NIR spectrophotometer. Photoluminescence measurements were conducted at room temperature using an Edinburgh FS5 fluorometer with NIR extension. Matrix-assisted laser desorption/ionization (MALDI) spectra were taken on a Bruker Daltonics UltrafleXtreme MALDI TOF/TOF using α-cyano-4-hydroxycinnamic acid as the matrix in positive mode. Thermogravimetric analysis (TGA) was performed using a Discovery TGA thermogravimetric analyzer. All samples were equilibrated at 100 °C for one hour before increasing the temperature to remove water. Experiments were conducted under nitrogen flow. The gel filtration chromatography (GFC) setup was an AKTAprime Plus system equipped with a Superose 6 10/300 GL column. The mobile phase was 1x PBS, and measurements were carried out at a flow rate of 0.5 mL/min. 250 μL of each sample were injected, and absorbance at 280 nm was recorded. Liquid chromatography-mass spectrometry (LC-MS) analyses were conducted on the Agilent 1290 Infinity LC System equipped with an Agilent 6140 Quadruple mass spectrometer, using

acetonitrile and water containing 0.1% formic acid as the mobile phases at a rate of 0.6 mL/min. Gold concentrations for the Au NCs dissolved by potassium cyanide were measured using an Agilent 5100 ICP-OES. Quantum yields were measured using an integration sphere (Labsphere RTC-060-SF) under 785 nm diode laser excitation. An 850 nm longpass filter was used to block the excitation, and signal from the sample was collected using a calibrated germanium detector (Newport: 818-IR) through a lock-in amplifying system. The measured quantum yields were then corrected to account for leakage of the excitation light and the transmittance of the filter. SWIR images were taken using an InGaAs-based SWIR camera (900-1,600 nm) (Nirvana, Princeton Instruments) under 808 nm excitation and two 1000 nm longpass filters.

Synthesis of lipoic acid based sulfobetaine (LA-sulfobetaine)

LA-amide was synthesized according to a previously reported protocol[21] except that the solvent was changed to acetone nitrile and the buffer used for extraction was changed to 1 M sodium bicarbonate aqueous solution. Next, 1.5 g of LA-amide was dissolved in 50 mL of methanol and stirred for 10 min, followed by the successive addition of ammonium hydroxide (0.362 mL, 28% aqueous solution) and 1,3-propanesultone (0.510 mL). The reaction mixture was stirred at room temperature for 4 days before it was completely rotary-evaporated, resulting an oily crude product. Ethanol (50 mL) and hexanes (50 mL) were then added and the mixture was allowed to stand overnight. LA-sulfobetaine as the precipitate was collected and dissolved in 3 mL of water for storage.

Synthesis of SWIR-emitting Au NCs

SWIR Au NCs were synthesized by modifying a literature method.[4] For Au NCs (1:1), briefly, 1 mg of LA-sulfobetaine was dissolved in 5 mL of DI water. Upon stirring, sodium hydroxide

aqueous solution (100 μL, 0.2 M) and hydrogen tetrachloroaurate (III) hydrate (1 mg) in DI water (50 μL) were added. The mixture was stirred at room temperature for 5 min, followed by the dropwise addition of sodium borohydride aqueous solution (100 μL, 50 mM). The mixture was stirred overnight, and Au NCs were purified *via* three repeated dialysis steps using a 10kDa cutoff dialysis filter. The Au NCs were dissolved in DI water (400 μL) and stored at 4 °C. The reaction yield was about 97%.

Treatment of Au NCs with extra LA-sulfobetaine ligands

10 mg LA-sulfobetaine in 100 μL DI water was added to the stock 400 μL of the Au NC (1:1) solution under stirring. The reaction was allowed to stand overnight. Au NCs were purified using a 10K cutoff dialysis filter for 3 times and a NAP-10 column before characterizations. The final product was dissolved in 0.5 mL aqueous solvent (DI water, 1x PBS or isotonic saline) and stored at 4 °C. The reaction yield was about 96%.

Quantification of LA-sulfobetaine

A series of LA-sulfobetaine aqueous solution with different concentrations (0.1-10 mg/mL) was injected into the LC-MS setup. A representative LC spectrum and the corresponding MS spectrum are shown in Figure 5-10. The areas of the LA-sulfobetaine peak in the LC spectra were calculated. Thus, a work function of the integrated area versus the concentration of LA-sulfobetaine was plotted. Au NCs were dissolved using potassium cyanide and analyzed using LC-MS. Based on the area of the LA-sulfobetaine peak, the concentration can be readily obtained.
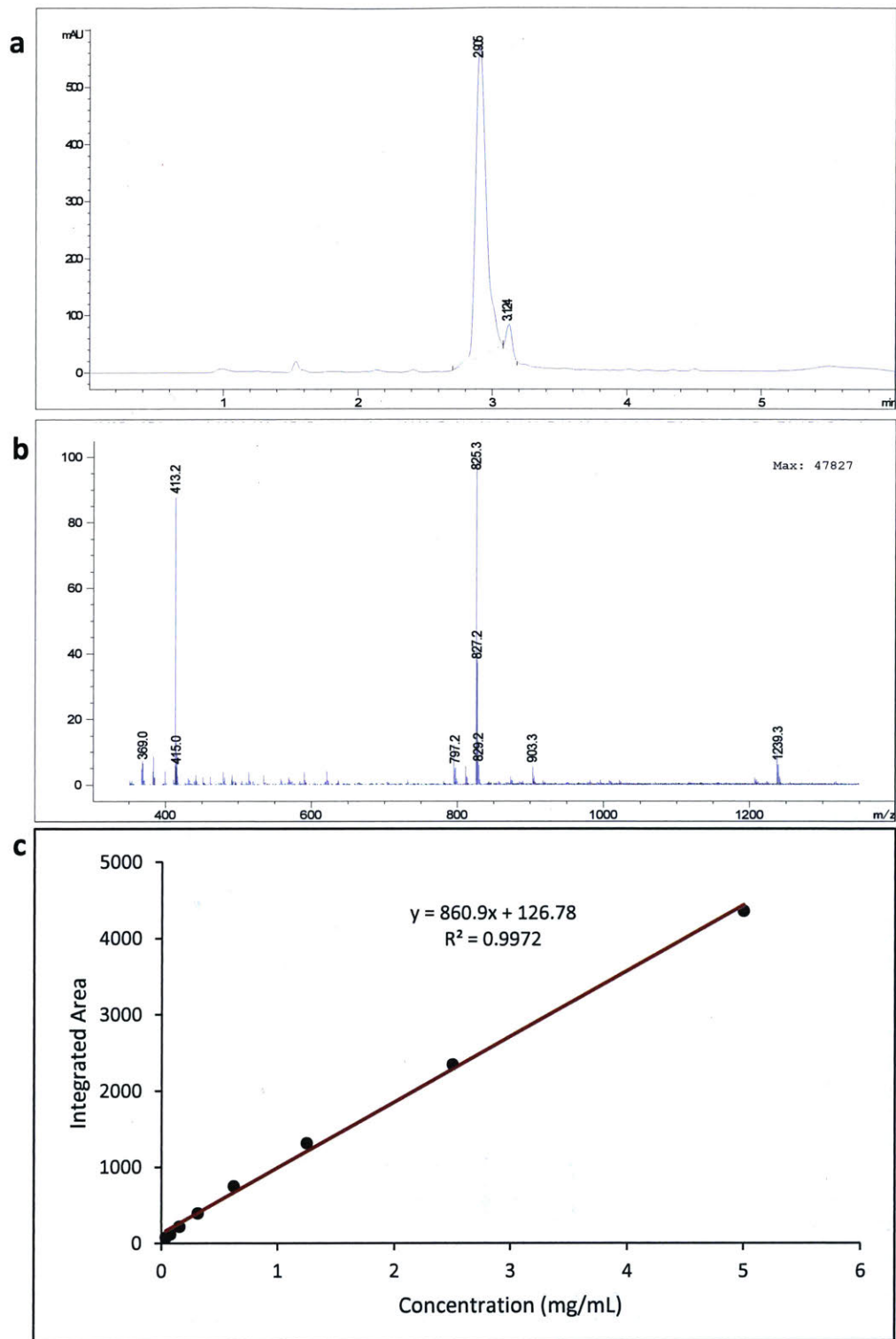
Figure 5-10. (a) HPLC trace of LA-sulfobetaine with 254 nm absorption and (b) Mass spectrum of the largest peak in (a) using LC-MS. (c) Fitting curve of HPLC integrated area versus concentration of LA-sulfobetaine.

Serum stability test

150 μL of Au NCs (1:1) treated with LA-sulfobetaine in isotonic saline were mixed with an equal volume of FBS in an Eppendorf tube. As controls, 150 μL of Au NCs (1:1) treated with LA-sulfobetaine ligands solution were mixed with 150 μL of isotonic saline, and 150 μL of FBS were diluted with 150 μL of isotonic saline in separate tubes. The three tubes were placed in a shaker, warmed to 37 °C, and shaken for 4 h. Each solution was then filtered through a 0.2 μm syringe filter prior to GFC measurements. An Agilent 1260 Series Bio-inert HPLC system equipped with an absorbance diode array detector and a Superose 6 column was used for analysis. The mobile phase was composed of Tris/Tris base (pH 7.5), isotonic NaCl, and 0.02% NaN_3. Analysis was carried out at a flow rate of 0.5 mL/min for all samples: 100 μL of each sample was injected into the instrument, and absorbance at 280 and 750 nm was recorded.

Cell toxicity test

4T1 breast cancer cells were seeded into a 96-well plate with a cell density of 4k/well and incubated at 37 °C for 12 h for cell attachment. Au NCs with different concentrations (0-50 μg/mL) were added, and cells were incubated for 3 days. The cell medium was removed, and cells were washed with PBS twice. MTT reagent (ATCC, 10 μL) was added to each well and the cells were incubate at 37 °C for 3 h. Purple precipitates were observed. DMSO was then added to dissolve the purple precipitates for 20 min under shaking. Absorbance at 570 nm was recorded on a plate reader.

5.5 Chapter-specific Acknowledgement

References

1.   Zhou, C.; Hao, G. Y.; Thomas, P.; Liu, J. B.; Yu, M. X.; Sun, S. S.; Oz, O. K.; Sun, X. K.; Zheng, J. Near-Infrared Emitting Radioactive Gold Nanoparticles with Molecular Pharmacokinetics *Angew. Chem. Int. Ed.* **2012,** *51*, 10118-10122.

2.   Shang, L.; Azadfar, N.; Stockmar, F.; Send, W.; Trouillet, V.; Bruns, M.; Gerthsen, D.; Nienhaus, G. U. One-Pot Synthesis of near-Infrared Fluorescent Gold Clusters for Cellular Fluorescence Lifetime Imaging *Small* **2011,** *7*, 2614-2620.

3.   Xie, J. P.; Zheng, Y. G.; Ying, J. Y. Protein-Directed Synthesis of Highly Fluorescent Gold Nanoclusters *J. Am. Chem. Soc.* **2009,** *131*, 888-889.

4.   Le Guevel, X.; Tagit, O.; Rodriguez, C. E.; Trouillet, V.; Leal, M. P.; Hildebrandt, N. Ligand Effect on the Size, Valence State and Red/near Infrared Photoluminescence of Bidentate Thiol Gold Nanoclusters *Nanoscale* **2014,** *6*, 8091-8099.

5.   Jin, R. C. Atomically Precise Metal Nanoclusters: Stable Sizes and Optical Properties *Nanoscale* **2015,** *7*, 1549-1565.

6.   Lopez-Tobar, E.; Hernandez, B.; Ghomi, M.; Sanchez-Cortes, S. Stability of the Disulfide Bond in Cystine Adsorbed on Silver and Gold Nanoparticles as Evidenced by Sers Data *Journal of Physical Chemistry C* **2013**, *117*, 1531-1537.

7.   Nuzzo, R. G.; Allara, D. L. Adsorption of Bifunctional Organic Disulfides on Gold Surfaces *J. Am. Chem. Soc.* **1983**, *105*, 4481-4483.

8.   Wu, Z. K.; Jin, R. C. On the Ligand's Role in the Fluorescence of Gold Nanoclusters *Nano Lett.* **2010**, *10*, 2568-2573.

9.   Luo, Z. T.; Yuan, X.; Yu, Y.; Zhang, Q. B.; Leong, D. T.; Lee, J. Y.; Xie, J. P. From Aggregation-Induced Emission of Au(I)-Thiolate Complexes to Ultrabright Au(0)@Au(I)-Thiolate Core-Shell Nanoclusters *J. Am. Chem. Soc.* **2012**, *134*, 16662-16670.

10.   Wang, G. L.; Huang, T.; Murray, R. W.; Menard, L.; Nuzzo, R. G. Near-Ir Luminescence of Monolayer-Protected Metal Clusters *J. Am. Chem. Soc.* **2005**, *127*, 812-813.

11.   Wang, G. L.; Guo, R.; Kalyuzhny, G.; Choi, J. P.; Murray, R. W. Nir Luminescence Intensities Increase Linearly with Proportion of Polar Thiolate Ligands in Protecting Monolayers of Au-38 and Au-140 Quantum Dots *J. Phys. Chem. B* **2006**, *110*, 20282-20289.

12.   Zeng, C. J.; Liu, C.; Chen, Y. X.; Rosi, N. L.; Jin, R. C. Gold-Thiolate Ring as a Protecting Motif in the Au-20(Sr)(16) Nanocluster and Implications *J. Am. Chem. Soc.* **2014**, *136*, 11922-11925.

13.   Zhang, Z. Y.; Xu, L. J.; Li, H. X.; Kong, J. L. Wavelength-Tunable Luminescent Gold Nanoparticles Generated by Cooperation Ligand Exchange and Their Potential Application in Cellular Imaging *RSC Adv.* **2013**, *3*, 59-63.

14.   Huang, T.; Murray, R. W. Visible Luminescence of Water-Soluble Monolayer- Protected Gold Clusters *J. Phys. Chem. B* **2001**, *105*, 12498-12502.

15.   Pyo, K.; Thanthirige, V. D.; Kwak, K.; Pandurangan, P.; Ramakrishna, G.; Lee, D. Ultrabright Luminescence from Gold Nanoclusters: Rigidifying the Au(I)-Thiolate Shell *J. Am. Chem. Soc.* **2015,** *137*, 8244-8250.

16.   Deng, H. H.; Shi, X. Q.; Wang, F. F.; Peng, H. P.; Liu, A. L.; Xia, X. H.; Chen, W. Fabrication of Water-Soluble, Green-Emitting Gold Nanoclusters with a 65% Photoluminescence Quantum Yield Via Host-Guest Recognition *Chem. Mater.* **2017,** *29*, 1362-1369.

17.   Hong, G. S.; Zou, Y. P.; Antaris, A. L.; Diao, S.; Wu, D.; Cheng, K.; Zhang, X. D.; Chen, C. X.; Liu, B.; He, Y. H.*, et al.* Ultrafast Fluorescence Imaging in Vivo with Conjugated Polymer Fluorophores in the Second near-Infrared Window *Nat. Commun.* **2014,** *5*, 4206.

18.   Moyano, D. F.; Saha, K.; Prakash, G.; Yan, B.; Kong, H.; Yazdani, M.; Rotello, V. M. Fabrication of Corona-Free Nanoparticles with Tunable Hydrophobicity *Acs Nano* **2014,** *8*, 6748-6755.

19.   Gupta, A.; Moyano, D. F.; Parnsubsakul, A.; Papadopoulos, A.; Wang, L. S.; Landis, R. F.; Das, R.; Rotello, V. M. Ultrastable and Biofunctionalizable Gold Nanoparticles *Acs Applied Materials & Interfaces* **2016,** *8*, 14096-14101.

20.   Oh, E.; Susumu, K.; Goswami, R.; Mattoussi, H. One-Phase Synthesis of Water-Soluble Gold Nanoparticles with Control over Size and Surface Functionalities *Langmuir* **2010,** *26*, 7604-7613.

21.   Zhan, N. Q.; Palui, G.; Grise, H.; Tang, H. L.; Alabugin, I.; Mattoussi, H. Combining Ligand Design with Photoligation to Provide Compact, Colloidally Stable, and Easy to Conjugate Quantum Dots *Acs Applied Materials & Interfaces* **2013,** *5*, 2861-2869.

Chapter 6

SWIR *In Vivo* Imaging with Gold Nanoclusters

6.1 Rapid Renal Clearance of Au NCs

Efficient renal clearance of functional nanomaterials for contrast is of fundamental importance for *in vivo* biomedical applications to ensure that agents can be effectively cleared from the body, have little accumulation in organs, and show minimum interference with other diagnostic tests.[1-3] To have a general understanding of the biodistribution and renal clearance efficiency of our Au NCs, Au NCs (0.125 mg Au) treated with extra LA-sulfobetaine were injected into NCRNU-M mice via the tail vein, and images were taken under 808 nm laser excitation using a SWIR camera from the front side of the mouse. Signal in the heart, lung and gut of the mice could immediately
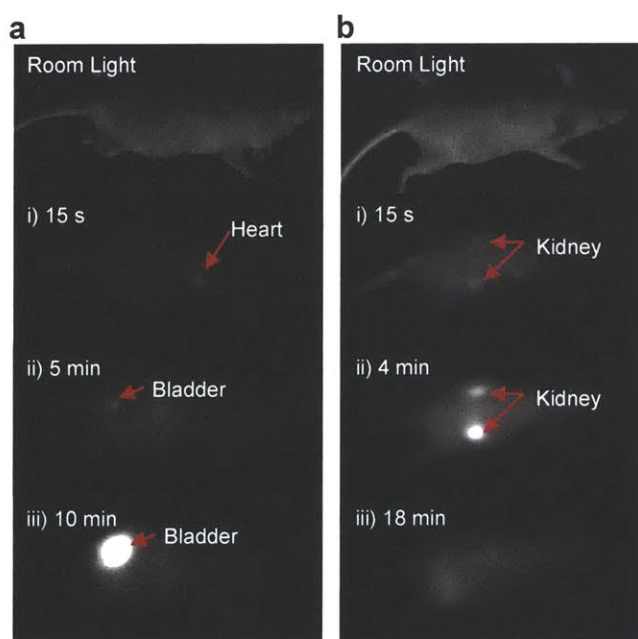
Figure 6-1. A time series of SWIR fluorescence images taken from (a) the front side and (b) the back side of a mouse after tail vein injection of Au NCs.

be observed, and renal clearance was observed after 5 min (Figure 6-1a). To further demonstrate that the Au NCs were excreted by the kidneys, a second injection of Au NCs (0.125 mg gold) was given to the same mouse and images were recorded from the back side. The kidneys are visible within 1 min and the signal disappears after 18 min (Figure 6-1b). Urine was collected from the bladder for further analysis. The photoluminescence spectra of the injected Au NCs sample and the urine overlapped well (Figure 6-2a), indicating that Au NCs were present in the urine. GFC traces show that the retention time of the Au NCs in the urine is the same as that of Au NCs prior to injection (Figure 6-2b), indicating negligible size change of the Au NCs before injection and after being excreted from the mouse. We also took images of the fractions collected by GFC using our InGaAs camera, which further demonstrates the presence of the Au NCs in the urine and the consistent HDs before and after injection (Figure 6-3).
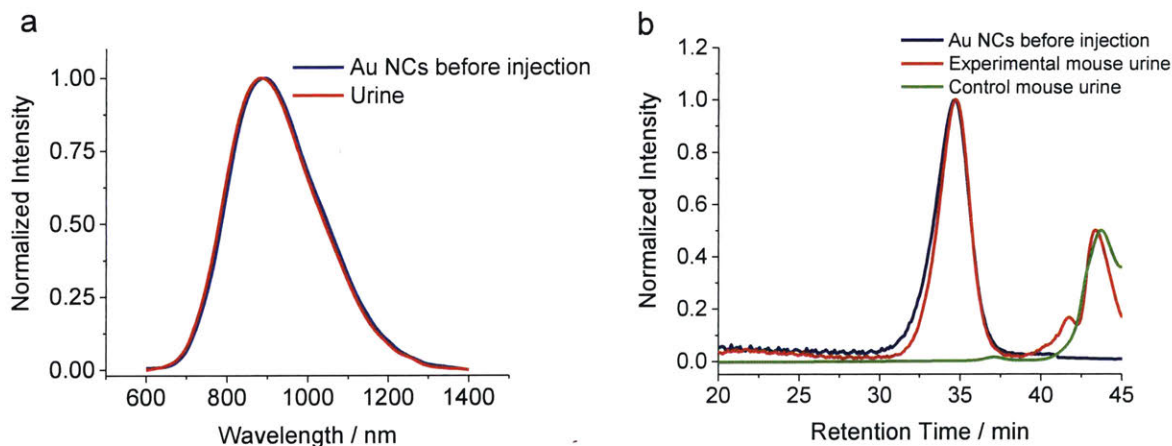
Figure 6-2. (a) Emission spectra and (b) GFC traces of Au NCs before injection into the mouse (blue curve) and the urine collected from both the experimental mouse bladder (red curve) and the control mouse bladder (green curve).

121
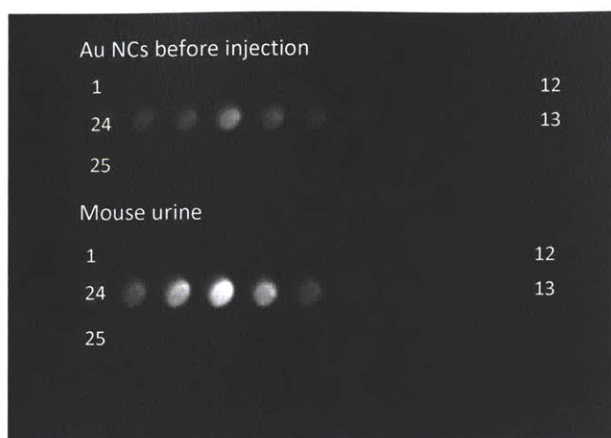
Figure 6-3. Images of GFC fractions of original Au NCs solution (top three rows) and the urine collected from a mouse that was treated with the Au NCs (bottom three rows), respectively. Urine fractions were collected starting from 20 min post-injection with subsequent fractions taken every 0.6 min. Fraction numbers are marked on the wells.

6.2 Biodistribution of Au NCs

The *in vivo* biodistribution of Au NCs was also investigated by intravenously injecting Au NCs into FVB mice and subsequently quantifying Au content in different tissues via inductively coupled plasma mass spectrometry (ICP-MS). As shown in Figure 6-4, Au NCs showed minimal accumulation in skin, muscle, heart, lungs, brain, and blood at 3 h post injection. Some
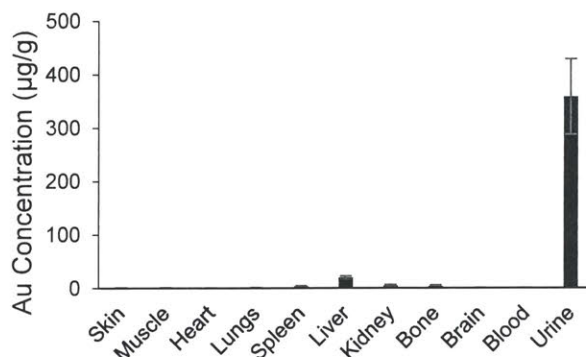
Figure 6-4. Biodistribution of Au in FVB mice (n=6) at 3 h post injection of Au NCs (0.089 mg of Au). Data were measured using ICP-MS and presented as µg of Au per gram of tissue.
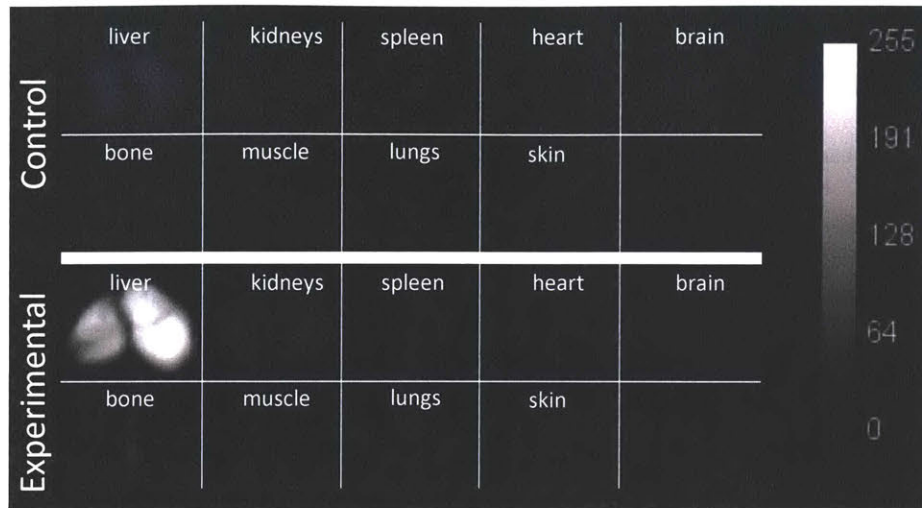
Figure 6-5. *Ex vivo* fluorescence imaging of tissues harvested from mice treated with 1x PBS (n=3) or Au NCs (n=6) at 3 h post injection (top two rows: control mouse; lower two rows: experimental mouse; exposure time: 25 ms).

a   b
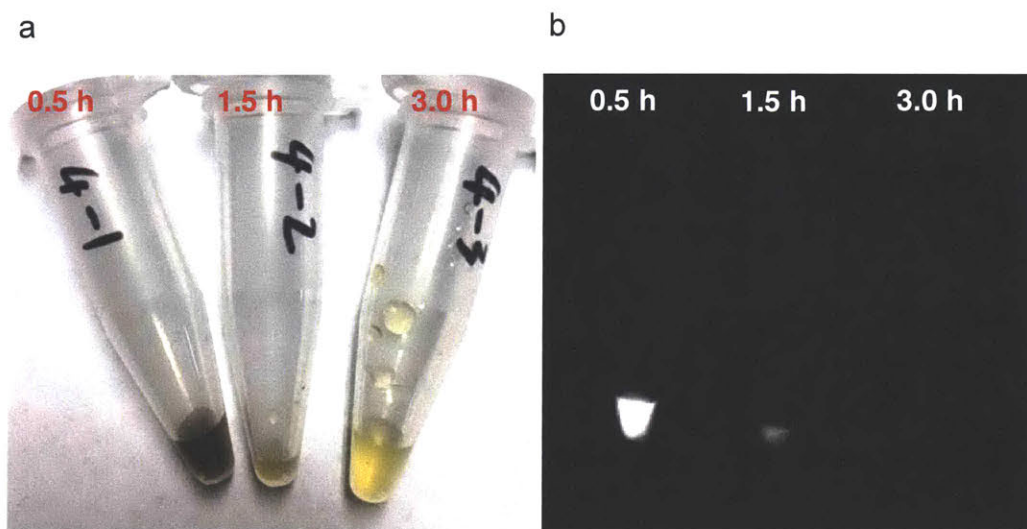
Figure 6-6. Images of mouse urine collected at 0.5 h, 1.5 h and 3.0 h post injection (a) under room light and (b) under SWIR camera (exposure time 2.5 ms, 10x shorter than in Figure 6-5).

accumulation of Au NCs in mononuclear phagocytic system (MPS) such as liver, spleen, and bone marrow was observed. Images of the organs taken using an InGaAs camera showed higher signal

intensities of liver, kidneys, spleen and bone (Figure 6-5), which is consistent with the ICP-MS result. SWIR imaging of mouse urine collected at 0.5 h, 1.5 h, and 3 h, respectively, showed a decreased fluorescence intensity over time (Figure 6-6), and ICP-MS analysis indicates Au content in the urine accounts for about 70% of the injected dose, further demonstrating the rapid clearance of Au NCs. The clearance of these particles is faster than previously reported Au NCs.[1, 4]

6.3 Improved Resolution of SWIR *In Vivo* Imaging
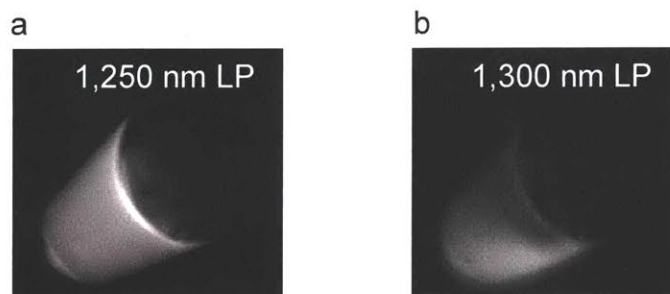
Figure 6-7. Images of Au NCs (1:1) treated with extra LA-sulfobetaine ligands taken using an InGaAs camera with (a) 1250 nm LP filter and (b) 1300 nm LP filter applied.

As seen from the emission spectrum of Au NCs (1:1) treated with extra LA-sulfobetaine ligands, a long spectral tail exists to beyond 1,300 nm (Figure 5-6b). Despite the lower intensity in this region, the quality of *in vivo* SWIR imaging may be better because of the reduced background signal from tissues. Thus, we took images of this sample using an InGaAs camera with 1,250 nm, and 1,300 nm LP filters added, respectively. As shown in Figure 6-7, a high SNR was maintained even after applying a 1,300 nm LP filter. We later injected the sample into a wild type mouse (C57BL/6), and a set of images of the left leg were taken using a silicon camera with a 850 nm LP filter and an InGaAs camera with a 1250 nm LP filter respectively under 808 nm excitation. Figure 6-8 shows that a more detailed image of the blood vessels can be discerned from the images taken

using the InGaAs camera, demonstrating the advantage of SWIR *in vivo* imaging with Au NCs over conventional NIR imaging.
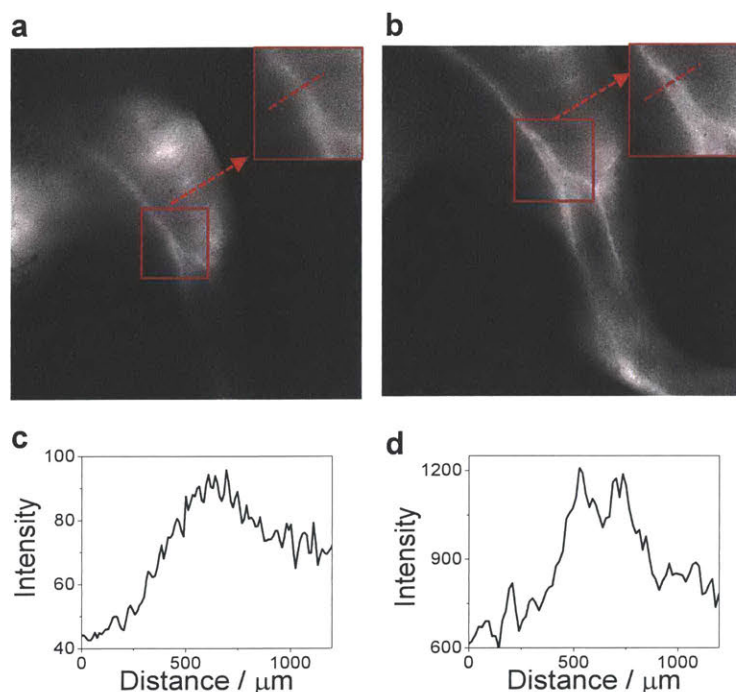
Figure 6-8. Images of the left leg of a wild type C57BL/6 mouse taken using (a) a silicon camera with a 850 nm LP filter, and (b) an InGaAs camera with a 1250 nm LP filter, respectively (Insets are zoomed-in areas indicated in the red squares). (c-d) The intensity across a line of interest drawn in the inset images above.

6.4 Summary

In summary, we have developed water-soluble LA-sulfobetaine capped Au NCs with good QYs that emit in the SWIR. The SWIR emitting Au NCs have small HDs, minimum non-specific binding and rapid renal clearance. *In vivo* imaging of these Au NCs shows a higher contrast and resolution in the SWIR than in the more conventional NIR region, demonstrating the potential of SWIR imaging to improve *in vivo* imaging using Au NCs.

6.5 Experimental Details

Instrumentation

The gel filtration chromatography (GFC) setup was an AKTAprime Plus system equipped with a Superose 6 10/300 GL column. The mobile phase was 1x PBS, and measurements were carried out at a flow rate of 0.5 mL/min. 250 µL of each sample was injected, and absorbance at 280 nm was recorded. Mouse tissues and blood were digested using aqua regia using a Milestone UltraWave microwave sample digestion system, and the gold content in each tissue or blood sample was measured using an Agilent 7900 ICP-MS. *In vivo* imaging data were recorded using an InGaAs-based SWIR camera (900-1,600 nm) (Nirvana, Princeton Instruments) and a silicon based camera (PIXIS, Princeton Instruments) under 808 nm excitation and different longpass filters (Thorlabs and Edmund Optics) as indicated.

Animals

Eight-week-old NCRNU-M mice were purchased from Taconic (Hudson, NY). Fifteen-week-old FVB mice were purchased from Charles River Laboratories. A C57BL/6 mouse (male, 8 weeks) was purchased from The Jackson Laboratory. The animal protocol was reviewed and approved by the Institutional Animal Care and Use Committee at the Massachusetts Institute of Technology.

In Vivo SWIR Imaging

NCRNU-M mice were anesthetized by intraperitoneal injection of ketamine (200 µL) and xylazine (100 µL) in isotonic saline (700 µL) (150 µL/30g mouse). A tail vein catheter was inserted after mice were unresponsive to toe pinch. Mice were placed on the imaging stage to collect background images for the assessment of animal autofluorescence. Mice were then intravenously injected with

Au NCs (1:1) treated with LA-sulfobetaine ligands (200 μL/mouse, 0.125 mg of Au) to observe the injection and initial distribution of Au NCs in the blood. First dose of Au NCs (0.125 mg of Au) was injected, and video was taken from the front side. About 20 min later, a second dose of Au NCs (0.125 mg of Au) was injected via the tail vein, and video was taken from the back side of the mice.

A C57BL/6 mouse was anesthetized using the same method as mentioned above, and the hair on the left leg was shaved. Au NCs (0.5 mg of Au) was injected via tail vein, and images of the left leg were taken using a silicon camera with an 850 nm longpass filter applied. Another dose of Au NCs (0.5 mg Au) was injected via the tail vein, and images of the left leg were taken using an InGaAs camera equipped with 1,000 nm, 1,150 nm, and 1,250 nm longpass filters, respectively.

Biodistribution

200 μL of Au NCs (0.089 mg **of** Au determined by ICP-MS) was injected via tail vein into six FVB mice **each**. Three control FVB mice were injected with 200 uL1x PBS each. Mouse urine was collected at 0.5 h, 1.5 h and 3.0 h post injection, respectively. Organs and blood were harvested from both the experiment and control group of mice at 3 h post injection and stored in pre-weighed petri dishes and Eppendorf tubes. The petri dishes and Eppendorf tubes were weighed again to get the weight of each organ or blood sample. The samples were then digested using aqua regia by the microwave digester. The resulting clear solutions were diluted for ICP-MS analysis.

6.6 Chapter-specific Acknowledgement

References

1.   Zhou, C.; Long, M.; Qin, Y. P.; Sun, X. K.; Zheng, J. Luminescent Gold Nanoparticles with Efficient Renal Clearance *Angew. Chem. Int. Ed.* **2011,** *50*, 3168-3172.

2.   Wang, B.; He, X.; Zhang, Z. Y.; Zhao, Y. L.; Feng, W. Y. Metabolism of Nanomaterials in Vivo: Blood Circulation and Organ Clearance *Acc. Chem. Res.* **2013,** *46*, 761-769.

3.   Aillon, K. L.; Xie, Y. M.; El-Gendy, N.; Berkland, C. J.; Forrest, M. L. Effects of Nanomaterial Physicochemical Properties on in Vivo Toxicity *Advanced Drug Delivery Reviews* **2009,** *61*, 457-466.

4.   Semmler-Behnke, M.; Kreyling, W. G.; Lipka, J.; Fertsch, S.; Wenk, A.; Takenaka, S.; Schmid, G.; Brandau, W. Biodistribution of 1.4-and 18-Nm Gold Particles in Rats *Small* **2008,** *4*, 2108-2111.

Acknowledgements

During the past 5 years at MIT, I have gained so much both as a person and as a scientist. I can't be more grateful for the opportunity to do research and achieve academic accomplishments at the most prestigious institute. I want to thank all the people who made this process a lot easier and enjoyable for me. I won't be able to come here without their help and support.

First of all, I want to thank my supervisor, Prof. Moungi Bawendi, for offering me the chance to work in his lab. I still remember how excited I was after receiving an interview from him when I thought MIT had rejected my application. From him, I learned to do science in a high quality and look at things in a big picture. I really appreciate the freedom to try out new ideas as he has always been supportive and inspiring. He is very careful and serious on science but very kind and easy privately. I also want to thank him for gathering people from highly diverse backgrounds and initiating a comfortable atmosphere to work in.

I really like spending time in the lab and in our office with the Bawendiens. Our group has about 25 students from more than 10 countries, speak more than 13 languages. It has been a great experience to learn about different cultures during lunch time in the kitchen. Topics like politics, education, sports, and food can inspire a lot of discussions. We also have the chance to taste Swiss chocolates, French crepes and king cake, German Feuerzangenbowle, Chinese dim sum and so on. Group traditions like Charles Muddy Friday, ski trip every winter, summer BBQ at Moungi's house, and welcome/farewell lunch at Mulan bring everyone closer to each other. I want to thank all the Bawendiens for creating such a nice and enjoyable working environment.

In terms of professional development, I especially want to thank my mentor Ou Chen for bringing me into this field. The "World No.1 CdSe/CdS Synthetic Chemist" passed over his expertise in II-VI QD synthesis to me, ennobling me "World No.2" (not verified). I want to thank Ou Chen, Shuang Zhao, He Wei, and Yunfei Zhang for helping me to adapt to the culture here and providing me a lot of suggestions both in life and in research. I want to thank Oliver Bruns for introducing me to the gold nanocluster project and offering me tremendous help in the *in vivo* imaging part and final draft improvement. I want to thank Jose Cordero for collaborating on the norbornene ligand project. It was very exciting to try new ideas out together. I want to thank our assistant Miao Li for providing so many advices on job applications and connecting me to her friend for suggestions on career development. I want to thank Yi Shen for getting me involved in his engineering projects and sharing information in the job hunting process. I want to thank Michel Nasilowski for encouraging me and treating me with sweets when I was upset, as well as answering me a lot of random questions about QDs. I want to thank Odin Achorn, Daniel Franke, Dan Montana, and Jess Carr for offering help on my projects and giving me advices on my writing. I want to thank Chia-Hao Chuang for his helpful tips on job applications. I want to thank Jason, Matthias, Mari, and Eric for creating so many laughs in the office. I want to thank Wei Yu for her advices on career development and all the talks between us to cheer each other up. There are too many people to list here, I cannot accomplish these without your help, and I will keep all your kindness in my mind.

My PhD experience won't be so great without the company of my friends. My first-year Ashdown roommates Yiwen Zhu and Peng Wang are the first friends I made in the US. I still remember the days we learned cooking Chinese dishes and explored the new culture together. I am glad that we still rely on each other in a country where our families are far away from us. I want to especially thank Yiwen, whose optimistic and independent character has always inspired me. I was so honored to be her bridesmaid. I want to thank my badminton friends, Coach Pashupati, Grandpa Tang, Linbo, and so many others for training and playing games with me. I really appreciate their kindness to teach me the movements and skills. Badminton has been my favorite way to relax after a day's work in the lab, and I have made so many friends from various backgrounds and cultures through this sport.

I want to thank my best friend, my collaborator, and my mentor Hua Wang. We have been knowing each other for almost 10 years since undergrad, and I can't remember how much help and guidance I have received from him. He was always there to help whenever I encountered a problem, and he always stood on my side to support me whatever happened. Words failed to express my gratefulness.

Last but not least, I want to thank my families for raising me up and providing me endless support. Born into a non-one-child family, I want to thank my parents for standing all the pressure to bring me to this world when the one-child policy was very strict in China. My parents, themselves as teachers, have provided me the best education since I was young. They have always been supportive about whatever decisions I made, including the one that I wanted to come to the US for graduate study. Growing up, I have been so lucky to have my elder sister leading and taking care of me. She is always there to listen to me and provide her suggestions. I also want to thank my nephew, who has brought so much happiness to our family since his birth.

Thanks again to all those people who made my life possible up to this point. I will cherish all the beautiful memories forever.